MOUNTAIN-PLAINS CONSORTIUM

MPC 24-548 | P. Lu, D. Tolliver, X. Yang, J. Zhao, Y. Huang, and H. Wang

SENSITIVITY AND ACCURACY ASSESSMENT OF VEHICLE WEIGH-IN-MOTION SYSTEM MEASUREMENT ERRORS USING IN-PAVEMENT STRAIN-BASED SENSORS

A University Transportation Center sponsored by the U.S. Department of Transportation serving the Mountain-Plains Region. Consortium members:

Colorado State University
North Dakota State University
South Dakota State University
University of Colorado Denver
University of Denver
University of Utah
Utah State University
University of Wyoming

Technical Report Documentation Page

1. Report No.	2. Government Accession No.	3. Recipient's Catalog No.
MPC-601		

4. Title and Subtitle	5. Report Date
Sensitivity and Accuracy Assessment of Vehicle Weigh-In-Motion System Measurement Errors Using In-Pavement Strain-Based Sensors	August 2024
	6. Performing Organization Code

7. Author(s)	8. Performing Organization Report No.
Pan Lu, Denver Tolliver, Xinyi Yang, Jingnan Zhao, Ying Huang, Hao Wang	MPC 24-558

9. Performing Organization Name and Address	10. Work Unit No. (TRAIS)
North Dakota State University 1340 Administration Ave Fargo, ND 58105	11. Contract or Grant No.

12. Sponsoring Agency Name and Address	13. Type of Report and Period Covered
Mountain-Plains Consortium North Dakota State University PO Box 6050, Fargo, ND 58108	Final Report
	14. Sponsoring Agency Code

15. Supplementary Notes

Supported by a grant from the US DOT, University Transportation Centers Program

16. Abstract

The rapid increase in traffic volume and heavy vehicle loads is causing accelerated deterioration of pavement infrastructure worldwide. This research investigates the impact of overweight and dynamic axle loads on pavement performance, employing advanced weigh-in-motion (WIM) systems and machine learning models to enhance predictive accuracy. By integrating data from WIM systems with support vector regression (SVR) and random survival forest models, this study provides a comprehensive analysis of pavement deterioration trends, accounting for high-dimensional variables such as axle load spectra and environmental conditions. The findings reveal that overweight vehicles significantly reduce pavement life, particularly affecting fatigue cracking, rutting, and longitudinal cracking. The application of random survival forest models demonstrates superior predictive performance compared to traditional methods, enabling the development of survival probability curves that inform maintenance strategies. Furthermore, hybrid systems combining in-pavement sensors with roadside cameras and artificial neural networks offer promising solutions for correcting dynamic variables and improving measurement accuracy. This research provides a robust framework for assessing the impacts of traffic loads on pavement performance, offering practical solutions for enhancing infrastructure resilience and sustainability. The insights gained contribute to the optimization of pavement design, maintenance, and rehabilitation strategies, ensuring the longevity and safety of roadways in the face of increasing transportation demands.

17. Key Word	18. Distribution Statement
Weigh-In-Motion, machine learning, traffic loading, support vector machine, random survival forest, overweight traffic	Public distribution

19. Security Classif. (of this report)	20. Security Classif. (of this page)	21. No. of Pages	22. Price
Unclassified	Unclassified	149	n/a

Form DOT F 1700.7 (8-72) Reproduction of completed page authorized

Sensitivity and Accuracy Assessment of Vehicle Weigh-In-Motion System Measurement Errors Using In-Pavement Strain-Based Sensors

Pan Lu, Ph.D.
Upper Great Plains Transportation Institute
North Dakota State University
Fargo, ND

Denver Tolliver, Ph.D.
Upper Great Plains Transportation Institute
North Dakota State University
Fargo, ND

Xinyi Yang
Department of Transportation, Logistics, and Finance
North Dakota State University
Fargo, ND

Dr. Jingnan Zhao
Center for Advanced Infrastructure and Transportation at Rutgers
Rutgers, The State University of New Jersey

Dr. Ying Huang
Department of Civil and Environmental Engineering
North Dakota State University
Fargo, ND

Dr. Hao Wang
Department of Civil and Environmental Engineering
Rutgers, The State University of New Jersey

August 2024

Acknowledgments

This research was made possible with funding supported by the U.S. Department of Transportation through the Mountain-Plains Consortium (MPC) Transportation Center. The authors express their gratitude to the U.S. DOT and MPC.

Disclaimer

ABSTRACT

The rapid increase in traffic volume and heavy vehicle loads is causing accelerated deterioration of pavement infrastructure worldwide. This research investigates the impact of overweight and dynamic axle loads on pavement performance, employing advanced weigh-in-motion (WIM) systems and machine learning models to enhance predictive accuracy. By integrating data from WIM systems with support vector regression (SVR) and random survival forest models, this study provides a comprehensive analysis of pavement deterioration trends, accounting for high-dimensional variables such as axle load spectra and environmental conditions. The findings reveal that overweight vehicles significantly reduce pavement life, particularly affecting fatigue cracking, rutting, and longitudinal cracking. The application of random survival forest models demonstrates superior predictive performance compared to traditional methods, enabling the development of survival probability curves that inform maintenance strategies. Furthermore, hybrid systems combining in-pavement sensors with roadside cameras and artificial neural networks offer promising solutions for correcting dynamic variables and improving measurement accuracy. This research provides a robust framework for assessing the impacts of traffic loads on pavement performance, offering practical solutions for enhancing infrastructure resilience and sustainability. The insights gained contribute to the optimization of pavement design, maintenance, and rehabilitation strategies, ensuring the longevity and safety of roadways in the face of increasing transportation demands.

EXECUTIVE SUMMARY

The global demand for efficient transportation infrastructure has escalated significantly over the past decades, driven by increased urbanization, economic growth, and globalization. This rise in demand has led to higher traffic volumes and heavier loads on roadways, resulting in accelerated deterioration of pavement structures. The presence of overweight vehicles, while economically beneficial for transport efficiency, poses significant challenges to pavement integrity. These vehicles induce various forms of distress, including fatigue cracking, rutting, and surface roughness, which ultimately reduce the lifespan of pavements and increase maintenance costs. Moreover, dynamic axle loads, exacerbated by pavement surface irregularities, contribute to fluctuating stress and strain levels within the pavement structure, further complicating the assessment of pavement performance.

Traditional pavement design and evaluation methods often fall short in accurately assessing these impacts due to the complex interplay of traffic loading, environmental factors, and pavement materials. These conventional methods may overlook the high-dimensional data and complex variable interactions that significantly affect pavement deterioration. This gap necessitates the exploration of more advanced methodologies that can provide a comprehensive understanding of pavement behavior under real-world conditions.

This research was conducted to address these challenges by leveraging weigh-in-motion (WIM) systems and advanced analytical techniques to assess and manage the impacts of traffic loads on pavement performance. This body of work integrates machine learning models and mechanistic-empirical approaches with WIM data to enhance the accuracy and reliability of pavement performance predictions. WIM systems offer significant advantages over traditional static weigh stations by providing real-time data on vehicle weights, axle configurations, and traffic patterns. These systems enable continuous monitoring of freight traffic, essential for enforcing weight regulations and optimizing pavement maintenance strategies.

Despite their benefits, WIM systems face challenges in maintaining measurement accuracy due to factors such as temperature fluctuations, pavement surface conditions, and vehicle dynamics. For instance, changes in pavement temperature can affect the stress-strain state of pavement layers, impacting sensor signals. Additionally, vehicle wandering and uneven road surfaces introduce potential errors in weight assessments. This research addresses these challenges by integrating advanced technologies with WIM systems to improve predictive accuracy and reliability.

The integration of machine learning techniques, such as support vector regression (SVR) and random survival forest models, plays a crucial role in this research. These models incorporate detailed axle load spectra, traffic loading, and environmental conditions to provide a more comprehensive framework for understanding pavement degradation trends. The findings indicate that the inclusion of detailed axle load data in performance models is essential for accurately assessing the impact of traffic loading on pavement life. By employing these advanced models, the research demonstrates that predictive accuracy significantly improves compared to traditional regression methods.

One of the critical findings of this research is the substantial reduction in pavement life caused by overweight traffic. The research quantifies the reduction ratios for different types of pavement distress and designs, emphasizing the need for precise predictive models in pavement management. The application of random survival forest models has proven effective in quantifying the impact of overweight traffic on pavement life, offering superior predictive accuracy compared to conventional methods. By utilizing datasets from the Long-Term Pavement Performance (LTPP) program, researchers have

developed survival probability curves that illustrate the influence of different traffic loading scenarios on pavement service life. These models enable transportation agencies to make informed decisions regarding pavement maintenance and rehabilitation strategies, ultimately contributing to more sustainable and cost-effective infrastructure management.

Moreover, this research explores the potential of hybrid systems that combine in-pavement sensors with roadside cameras and artificial neural networks to correct for dynamic variables and environmental influences. These approaches leverage machine learning and data analytics to refine pavement temperature predictions and assess dynamic axle loads, providing more reliable insights into pavement performance under real-world conditions.

In conclusion, this research represents a significant advancement in the field of pavement engineering by integrating advanced technologies with WIM systems to address the limitations of traditional methods. The insights gained from these studies provide a robust framework for assessing and managing the impacts of traffic loads on pavement performance. As a result, this research offers practical solutions for developing resilient transportation infrastructure capable of withstanding the demands of modern freight transportation. By addressing the current limitations of WIM systems and harnessing advanced analytics, this body of work contributes to the development of sustainable and efficient roadways, ensuring the longevity and safety of transportation networks for future generations.

TABLE OF CONTENTS

LIST OF TABLES

LIST OF FIGURES

1. INTRODUCTION

In 2021, the United States had approximately 282 million registered vehicles, with around 166 million being private and commercial trucks [1]. The growing demand for efficient transportation networks has led to increased traffic volumes and heavier loads on roadways, resulting in accelerated deterioration of pavement infrastructure. Understanding the impact of these loads on pavement performance is crucial for developing effective maintenance strategies and ensuring the longevity of roadway systems. However, traditional pavement design and evaluation methods often fail to account for the complex interactions between traffic loading, environmental conditions, and pavement materials. This oversight can lead to inaccurate predictions of pavement life and performance, ultimately resulting in higher maintenance costs and reduced serviceability.

The efficient road maintenance is vital for ensuring safe, sustainable, and economically viable transportation infrastructure, minimizing repair costs, enhancing road safety, and facilitating reliable traffic flow. Road maintenance is significantly influenced by factors such as vehicle traffic volume, diverse vehicle types, and varying weights, all contributing to the degradation of road infrastructure. The field of urban traffic data collection offers various methods, including data from swiping transit cards, online ride-hailing services, and bikesharing usage [2], [3], [4] . For highway traffic, the primary traffic data collection methods encompass the automatic traffic recorder and weigh station systems; however, the automatic traffic recorder can only provide vehicle counts, while weigh station systems collect detailed data on vehicles speed, axle load, gross vehicle weight, and classification.

The weigh station systems mainly include the static weigh stations and weigh-in-motion (WIM) stations. Static weigh stations offer high accuracy but have drawbacks as they influence traffic and may pose safety concerns. These stations are often situated next to highways, requiring vehicles to come to a complete stop or driving at a very low speed for weight measurement, resulting in significant time delays [5]. This becomes especially problematic when the volume of vehicles is high, and the capacity of static weigh station is insufficient to survey all passing heavy commercial vehicles.

In contrast, WIM stations offer benefits by providing real-time vehicle weight without disrupting them. In the field of traffic management, WIM systems contribute to optimizing traffic flow, reducing congestion, and supporting informed decision-making for road improvements. WIM technology also aids in safety enforcement and environmental protection. It helps monitor weight limits, ensures compliance with regulations, and guards against the detrimental effects of overloaded vehicles, enhancing road safety while reducing maintenance costs and environmental impact. They provide crucial data for pavement design, helping engineers create roads capable of withstanding the heavy loads of modern vehicles [6]. Additionally, the integration of machine learning techniques and mechanistic-empirical approaches has opened new avenues for analyzing the effects of traffic loads on pavement performance. These methodologies enhance predictive accuracy by incorporating high-dimensional data and complex variable interactions, which are often overlooked in traditional regression-based models.

A critical area of research within this domain is understanding the impact of overweight and dynamic axle loads on pavement service life. Given the increasing prevalence of heavy vehicles in freight transportation, these loads pose significant challenges to pavement integrity. The stresses induced by overweight trucks can lead to various forms of pavement distress, including fatigue cracking, rutting, and surface roughness, thereby shortening pavement life and increasing maintenance needs. Moreover, dynamic loads, exacerbated by pavement unevenness, contribute to fluctuating stress and strain levels within the pavement structure, further complicating the assessment of pavement performance.

Addressing these challenges requires a multidisciplinary approach that combines insights from civil engineering, data science, and materials science. By leveraging advanced analytical tools and comprehensive datasets, researchers can develop robust models that account for the myriad factors influencing pavement performance. This research not only advances the theoretical understanding of pavement mechanics but also provides practical solutions for infrastructure management, ultimately contributing to more sustainable and cost-effective transportation systems.

In this context, WIM systems have emerged as a vital tool for understanding the impact of traffic loads on pavement performance. These systems provide real-time data on vehicle weights, axle loads, and traffic patterns, which are essential for monitoring weight regulations and managing pavement life. WIM systems offer dynamic solutions by capturing vehicle data as they travel at highway speeds, allowing continuous monitoring and accurate enforcement of weight limits. This capability is crucial for identifying overweight vehicles that disproportionately contribute to pavement damage and deterioration.

Despite their benefits, WIM systems face challenges in maintaining measurement accuracy due to various factors such as temperature fluctuations, pavement surface conditions, and vehicle dynamics. For instance, changes in pavement temperature can alter the stress-strain state of pavement layers, impacting sensor signals. Vehicle wandering and uneven road surfaces introduce potential errors in weight assessments, underscoring the need for further research and technological advancements.

To overcome these limitations, recent studies have focused on integrating advanced technologies with WIM systems to enhance accuracy. Hybrid sensor systems that combine in-pavement sensors with roadside cameras and artificial neural networks offer promising solutions to correct for dynamic variables and environmental influences. These approaches leverage machine learning and data analytics to refine pavement temperature predictions and assess dynamic axle loads, providing more reliable insights into pavement performance under real-world conditions.

Notably, machine learning models for pavement temperature prediction have shown significant potential in improving WIM system accuracy. By utilizing comprehensive weather data and empirical modeling techniques, researchers have developed sophisticated models that account for temperature variations at different pavement depths. These advancements enhance the reliability of WIM data, equipping transportation agencies with valuable tools for infrastructure management and decision-making.

As the demand for efficient and sustainable transportation systems grows, the need for accurate and reliable traffic data becomes increasingly critical. By addressing the current limitations of WIM systems and harnessing advanced analytics, this body of research contributes to the development of resilient infrastructure capable of withstanding the demands of modern transportation. The insights gained from these studies inform the future of pavement design, maintenance, and traffic management, ensuring safe and efficient roadways for generations to come.

1.1 Impact of Traffic Loading on Pavement Damage

A literature review describes the quantification of pavement damage subjected to axle load spectrum of traffic loading recorded in WIM data. The review also highlighted the impacts of overweight traffic and longitudinal unevenness on pavement deterioration. Nonetheless, a review of the literature reveals the gap and scope for the predictive model of pavement damage considering various potential factors.

1.1.1 Statisical and Machine Learning Models

Past studies mainly used field data to quantify pavement damage due to vehicular loading using regression models. Li, and Sinha [7] developed load and non-load factor functions using the relative change in international roughness index (IRI) considering cumulative traffic loading, regional and climatic features, subgrade materials, design and construction standards, and pavement ages from Indiana pavement management system. Ong et al. [8] correlated pavement distresses, such as IRI, rut, and pavement condition rating, with average annual daily truck traffic and environmental factors on different highways. Gungor et al. [9] established the relationship between the change of condition rating survey with pavement age, daily traffic, and environmental factors to predict pavement deterioration under various loading conditions. Wu et al. [10] investigated the influence of overweight traffic on pavement service life considering climatic effects, truck origin and destination, permitted routes, and frequency of the routes.

Because of the complexity of the problem, the relationship between pavement performance and influential variables may not be apparent in traditional regression models. Advanced machine learning methods became commonly used to analyze the pavement performance data in pavement management system. Schlotjes et al. [11] used SVM method to predict the probability of structural failure of pavements and found that shear failure was more impacted by the combination of traffic, pavement composition, and material strength. Ziari et al. [12] analyzed the capability of SVM for predicting pavement condition by comparing five kernel types of SVM algorithm. The IRI was considered as the pavement performance index, and nine variables were selected in the proposed model. Gong et al. [13] predicted international roughness index (IRI) of flexible pavements based on the measured distress, climate, traffic, maintenance, and structural data using random forest regression. The results indicated that the random forest regression model significantly outperformed the linear regression model.

Fathi et al. [14] developed a hybrid machine learning method by combining random forest and artificial neural network (ANN) to predict alligator cracking index (ACI) based on the measured quality control parameters and analyzed influence of independent variables on ACI. Marcelino et al. [15] proposed a systematic approach to develop machine learning models for prediction of pavement performance. Various machine learning methods were supported, and the generalization performance was emphasized. Inkoom et al. [16] predicted highway pavement condition based on previous pavement condition ratings and selected time variant and invariant covariates using different machine learning methods. It was indicated that these machine learning methodologies were promising in predicting the crack of pavement with the coefficient of determination of 0.6-0.9. Inkoom et al. [17] investigated the use of recursive partitioning and ANN to predict crack rating of pavements and found that the recursive partitioning and ANN were efficient approaches to predict crack condition and their accuracy were close. Although these previous studies used machine learning methods for pavement performance analysis under multiple influential factors, few research investigated the effect of traffic loading on pavement deterioration using machine learning approach.

1.1.2 Pavement Damage Due to Overweight Traffic

It is well accepted that overweight trucks would accelerate pavement deterioration based on mechanistic-empirical (M-E) pavement analysis [18], [19], [20]. Field measurements of pavement distresses and traffic loads provide an opportunity to use statistical models to analyze the effects of overweight vehicles on pavement deterioration. Traditionally, multiple-variable linear or nonlinear regression models have been widely used to develop pavement distress index and identify the pavement damage induced by heavy truck traffic [21], [22].

Rys et al. [23] investigated asphalt pavement fatigue life caused by mixed traffic based on the axle load distribution and percentage of overweight vehicles. The analysis results indicated that the increase of percentage of overweight vehicles from zero to 20% would cause up to 50% reduction of fatigue life of asphalt pavement. Wang, and Zhao [24] estimated load equivalency factors of axle load on for fatigue cracking and rutting and quantified the reduction of pavement life caused by overweight traffic on thin and thick asphalt pavements. Batioja-Alvarez et al. [25] predicted rutting and fatigue cracking damage due to overweight vehicle considering the impact of vehicle loading, pavement temperature, and vehicle-miles traveled on pavement performance using mechanistic-empirical approach. It was found that the distribution of load equivalency factor could be incorporated in pavement design to consider the influence of overweight vehicles. Titi et al. [26] evaluated the impacts of overweight truck traffic on performance of four flexible pavements in Wisconsin and found that the proportion of pavement damage due to overweight trucks increased most of pavement distresses by 0.5% to 4%.

1.1.3 Pavement Damage Due to Vehicular Dynamic Loading

Pavement distress is an accumulated result of mechanistic responses in pavement structure subjected to dynamic loads of moving vehicles and climatic conditions. Pavement surface evenness deteriorates as pavement distress propagates. The variance of dynamic loads on rougher pavement surface condition leads to even faster pavement deterioration. It is vital to consider the vehicle-pavement interaction to estimate pavement distress in pavement design. Mechanical-empirical (M-E) method is applied to design pavement structures, which was developed under National Cooperative Research Program Projects 1-37A [27]. In Mechanical-Empirical Pavement Design Guide (MEPDG), the principles of engineering mechanics are applied to calculate pavement response under traffic loading. The empirical transfer functions are then used to predict long-term pavement performance through local calibrations. The axle load spectra obtained from WIM is utilized as traffic inputs in MEPDG. The WIM system captures gross vehicle weights, individual axle loads, and axle spacing when trucks are passing over the station. In general, the raw data collected by the WIM system need to be calibrated by comparing the field measurements of static scales to guarantee the required accuracy [28]. Therefore, WIM data indicates the static axle load spectra, which may not reflect the variation of dynamic loads on real pavements due to surface roughness.

Previous studies have evaluated the impact of dynamic loads on flexible pavement deterioration and service life. Navarrina et al. found that the service life of asphalt pavement was shorten by 40% after taking dynamic loads into consideration [29]. Bilodeau, Gagnon and Dore concluded that the pavement life could be reduced by 29% due to fatigue cracking and by 20% due to rutting after considering dynamic loads [30]. Gillespie et al. introduced the distribution of dynamic loads under a wheel with a mean value equal to static load and a standard deviation, which follows normal distribution [31]. Hu et al. suggested evaluated the pavement damage around manholes and suggested that the maximum of dynamic load was 1.29 times that of the static load which increased the pavement damage coefficient up to 2.12 times that of the static load [32]. To investigate the impacts of dynamic loads on pavement surface conditions, the dynamic loading coefficient (DLC) was defined as a ratio by dividing the standard deviation of dynamic loads by the mean value. Regression models were developed to correlate DLC with contributing factors, such as vehicle speed and pavement roughness conditions [33], [34], [35]. Misaghi et al. found that the pavement life decreased from 1.31 million to 0.63 million passes for a terminal rut depth of 15 mm, while pavement life decreased from 1.07 million to 0.64 million passes for a terminal of 40% at the vehicle speed of 90 km/h [36]. However, limited studies have taken the influence of axle loads on DLC into consideration.

Limited studies have considered dynamic loads induced by vehicles on rough pavement in pavement design. International roughness index (IRI) is a standard scale for roughness according to the response of a generic motor vehicle subjected to road surface roughness and determined by the measurement of road profile, simulation of vehicle responses, and accumulation of suspension travel [31]. It is quantified by measure of vertical deviations over a road section by the response-type road measuring system, such as road meters and profilometers [37]. Rys considered dynamic loads in the determination of axle load spectra in M-E pavement design by including the static axle load spectra and distributions of dynamic loads from specific axle load intervals. It was indicated that the cracked area and rut depth in medium pavement structure were increased by 67% and 8% under dynamic loads when the international roughness index (IRI) was 4 m/km [38]. The constant value of DLC was utilized in the transformation. However, axle loads were expected to have an influence on the variance of dynamic loads and DLC [39], [40]. In addition, Rys and Burnos found the effect of random error in axle load spectra arises from dynamic loads on the predicted traffic and overweight percentage need to be considered if random error was not low and the coefficient was greater than 0.05 [41].

The new asphalt overlay shows a similar cracking pattern which matches the cracking in the existing asphalt layer after opening to traffic. The cracking propagation from the existing asphalt concrete (AC) layer into and through the new AC overlay is named as reflective cracking. The effect of dynamic loads on reflective fatigue cracking of AC overlay on asphalt pavement can be quantified by transforming static axle load spectra to dynamic axle load spectra in M-E design. Since DLC values tend to change with axle load intervals designated by MEPDG in axle load spectra, it is essential to establish a correlation between DLC and axle loads to obtain the accurate dynamic axle load spectra. Besides, the change of axle load spectra that arises from dynamic loads on the overweight percentage needs to be considered, and the impact of overweight traffic on propagation of reflective fatigue cracking in AC overlay can be quantified considering dynamic loads induced on rough pavement surface.

1.2 Weigh-in-motion Systems

The research on the impact of traffic loading on pavement damage, based on data from WIM systems, brings many benefits. WIM systems provide numerous real-time data points, offering valuable insights into traffic patterns and their effects on pavement. However, concerns about accuracy have prompted further research to improve the precision of these systems. This section reviews existing literature related to WIM systems, aiming to identify and address shortcomings in current methodologies and technologies.

1.2.1 Pavement Temperature

The precision of a Weigh-in-Motion measurement system can be greatly impacted by pavement temperature, as temperature variations can alter the stress–strain state of the pavement layers, resulting in changes to the strain signals gathered by the strain sensor located beneath the pavement for WIM measurements [42]. Teltayev et al. [43] examined the temperature and moisture distribution, as well as stresses and strains, of a highway's pavement and subgrade in the northern region of Kazakhstan throughout a year-long cold period. Through experimental analysis utilising specialized sensors, the study found that the elasticity modulus of the asphalt concrete layers and upper subgrade increased notably (up to 18,000 MPa and 10,000 MPa, respectively) during the winter season. Additionally, all stress and strain components at pavement and subgrade points undergo significant changes throughout the annual cycle. Thus, accurately gathering the temperature data for different pavement layers is essential for accurate WIM measurements.

The pavement temperature can be collected directly by the embedded temperature sensors; however, they have a few limitations, such as high cost, limited durability, limited installation location options and difficulties in fixing any problems that arise after installation [44], [45]. Therefore, researchers have developed an alternative approach, such as utilising pavement temperature prediction models, which were intended to predict pavement temperatures based on environmental weather conditions [46], [47]. However, they are only based on one or few weather conditions. An effective prediction model should be capable of employing a comprehensive set of data on weather conditions, including temperature, humidity, wind, precipitation, and more, to analyse the influences of weather conditions on pavement performance.

Pavement temperature prediction models are categorized into (1) analytical, (2) numerical, and (3) empirical models. The former two models are based on solving partial differential equations for heat conduction under the prescribed boundary conditions, while the latter is developed through statistical analysis [48]. Analytical models and numerical models generally involve multiple heat transfer models such as incident short-wave radiation, reflected short-wave radiation, long-wave radiation emitted by the pavement, longwave back radiation emitted by the atmosphere, convection between the pavement surface and air, and heat flux conducted into the pavement [49]. Numerical methods can handle complex boundary conditions and nonlinearities in pavement temperature prediction models, providing an advantage over analytical methods [48]. Chen et al. [48] discussed different methods for predicting pavement temperature, including analytical models with simplified assumptions, and numerical methods such as Finite Difference Method, Finite Volume Method, and Finite Element Method, and highlighted the critical climatic and pavement factors affecting the accuracy of temperature prediction. While analytical models and numerical models offer greater flexibility and physical insights, they come with some disadvantages, such as being complex and computationally intensive. Moreover, they can be sensitive to input data quality and model parameters, which can require significant data collection and calibration efforts.

Empirical models are widely used in practice because they are straightforward to apply and can provide quick and accurate results when properly calibrated and validated against data. Chen et al. [48] illustrated empirical models' ability to estimate pavement temperature without analytical deviation or numerical computation. Empirical models also do not require a deep understanding of underlying physical mechanisms, making them easier to interpret and apply in certain contexts. Empirical models for predicting pavement temperatures are developed through statistical analysis and provide simplified associations between pavement temperature and affected factors.

As one of the primary types of asphalt pavement temperature models, empirical models should rely on large databases containing climatic, meteorological, geographical, and pavement data, such as air temperature, wind speed, solar radiation intensity, latitude, pavement layer thickness, and in-situ pavement temperature measurements at various depths [50]. Kršmanc et al. [51] proposed a purely statistical method for forecasting road surface temperature based on stepwise linear regression analysis with appropriate selection of input parameters and separate models for different time intervals, which showed comparable or better accuracy than physical models, and could be continuously improved with new data.

Empirical models and machine learning models are both used to make predictions based on observed data. However, empirical models are typically developed through regression analysis and rely on prior knowledge of the underlying relationship between variables, and are more widely used. Nonetheless, the past decade has witnessed a rapid growth in the use of machine learning (ML), particularly deep learning, due to its powerful fitting abilities and reduced dependence on prior knowledge. This has made ML a

promising data analytical approach for solving complex data patterns or formats in various applications, including image classification and machine translation [52].

Huang et al. investigated a road pavement structure comprising two HMA layers measuring 3.5 and 6.3 in., a granular base course layer measuring 17.7 in., and a subgrade soil layer measuring 110.2 in. and developed machine learning models to predict the average daily temperature at depths ranging from 20 to 106 in. below the pavement surface based only on the air temperature and day of the year. The results show that the accuracy of temperature prediction in the base and subgrade layers using machine learning models was found to be higher than that of an existing model. Matić et al. [53] utilised ANN to predict the minimum and maximum pavement temperatures at a specified depth, based again only on the surface pavement temperature. The models show adequate accuracy for predicting both maximum and minimum temperatures, with the model for minimal temperature at a specific depth being slightly more accurate. Rigabadi et al. [54] investigated the feasibility of utilising remote sensing technology to estimate pavement temperature. To accomplish this, the paper proposed three models, including linear, non-linear, and ANN, which were developed for the asphalt pavement at the surface level and at depths of 7.9 and 9.8 in. The accuracy of the predicted temperatures was then validated against measurements obtained from the BELLS3 model, which used data from a local weather station to calculate the temperature beneath the road surface. The results indicate that the predicted temperatures closely align with the measured temperatures. The BELLS3 models were widely used to estimate pavement temperature based on factors such as pavement surface temperature, average air temperature from the previous day, depth, and time of testing [55]. However, Marshall et al. [56] found BELLS3 model provided accurate predictions for temperatures below 25°C, but tended to underestimate the mid-depth temperature by an average of 5°C at higher temperatures.

In addition to the general concern of pavement temperature present in all WIM systems, there are specific concerns regarding the two primary data acquisition methods used in practical WIM systems: the embedded sensor system and the image capture system. The sensor system involves integrating specialized sensors into the road surface to detect vehicle forces and calculate real-time weights. Conversely, the image-capturing system strategically positions cameras to estimate weight by analyzing the tire's profile as the vehicle moves.

1.2.2 Embedded Sensor System

For a WIM system based on in-pavement sensors, the embedded sensor system consists of two main components: a data acquisition system and sensors integrated into the road surface. The sensors commonly used for this purpose include bending plates, load cell plates, polymer piezoelectric sensors, quartz piezoelectric sensors, and strain gauge strip sensors [57]. However, these electrical sensors, such as bending plates, load cell plates, polymer piezoelectric sensors, and quartz piezoelectric sensors, tend to be highly susceptible to their surrounding environment, which often leads to issues such as electromagnetic interference, relatively short lifespans, and moderate levels of measurement errors [58]. To overcome these challenges, Fiber Bragg Grating (FBG) technology has emerged as an attractive alternative for WIM systems based on in-pavement sensors. FBG technology offers several advantages, including immunity to electromagnetic radiation, non-conductive nature, lightweight design, spark-free operation, intrinsic safety, high sensitivity to strain, and embedding compatibility with structural elements [59]. FBG sensors find widespread application in research to measure parameters like strain, stress, temperature, pressure, and vibrations across diverse fields, encompassing structural health monitoring [60], [61], aerospace [62], etc. However, it is worth noting that bare FBG sensors are quite delicate and can be easily damaged when exposed to harsh and demanding environments. To address this, the proper packaging method of the FBG sensors becomes essential [63]. Recently, Glass Fiber Reinforced Polymer (GFRP) has been demonstrated to be an effective choice for packaging FBG sensors, known as GFRP-FBG sensors [58],

[64], for WIM systems in asphalt pavements to detect real-time wheel weights due to its impressive strength, durability, resistance to corrosion, and ability to withstand fatigue.

However, due to the fact that the GFRP-FBG sensors are point sensors, the accuracy of GFRP-FBG sensors for WIM measurement can be significantly influenced by the occurrence of the wandering effect, stemming from the disparity between sensor placement and actual wheel load positions [58]. This mismatch often results in inaccuracies as the sensors are fixed in location, failing to precisely align with the varying wheel positions of passing vehicles. As a consequence, this phenomenon introduces uncertainties and inconsistencies in weight measurements, undermining the reliability of the collected data. This difficulty arises from factors such as sensor accuracy, weather conditions, and road surface smoothness associated with current techniques [57]. Therefore, alternative approaches must be explored to enhance the accuracy of the WIM system based on FBG sensors, more specifically, the GFRP-FBG sensors.

1.2.3 Image-capturing System

On the other hand, a multitude of cutting-edge research studies have emerged, investigating pioneering approaches like computer vision within the domain of WIM systems without the need to install sensors beneath the road surface. Feng et al. [65] introduced a novel approach by leveraging computer vision methods to analyze images of moving vehicles. In this study, the researchers extracted tire deformation parameters, including tire-roadway contact length, vertical deflection, and tire make/model identification. They retrieved tire width and manufacturer-recommended tire inflation pressure from a tire information database and calculated vehicle weight by totaling the products of each tire's contact area and inflation pressure [65]. Furthermore, Kong et al. [66] employed cameras to capture images of moving vehicles and subsequently utilized computer vision techniques to detect tire-road contact areas and inflation pressure, achieving non-contact WIM solutions. The primary advantage of those studies lies in the image analysis of moving vehicles to estimate vehicle weight, where the images are captured by cameras placed near the road, eliminating the need for sensor installation. However, a limitation arises from the use of manufacturer-provided inflation pressure, which may not accurately reflect the actual tire conditions. Variations in contact pressure can occur due to tire type, tire load, and inflation pressure, ranging from significantly less than the inflation pressure to up to 10–30% more [67], [68], [69], [70]. Additionally, temperature fluctuations can lead to changes in inflation pressure [71]. This discrepancy is particularly pronounced for trucks carrying heavy loads, as the actual contact pressure may significantly differ from the manufacturer's recommended inflation pressure.

1.3 Problem Statement and Research Objectives

The development and maintenance of road infrastructure face significant challenges due to the complex interactions between traffic loads, pavement materials, environmental conditions, and monitoring technologies. Existing models often fall short in accurately predicting pavement performance and deterioration, while traditional weigh-in-motion (WIM) systems struggle with measurement inaccuracies due to factors like vehicle wandering and environmental influences. The integration of advanced technologies such as machine learning, hybrid systems, and innovative sensor technologies is essential to address these issues.

Therefore, based on the literature review, there are problems as shown below for traffic loading impacts, pavement performance prediction, and vehicle weight monitoring systems:

1. **Traffic Loading and Pavement Performance:** Many existing research models rely on estimates rather than actual traffic load measurements, leading to inaccuracies in predicting pavement deterioration. Most models fail to incorporate axle load spectra, which are crucial for understanding specific impacts on pavement life. Additionally, available models often focus on static conditions, overlooking dynamic effects caused by uneven surfaces.
2. **Overweight Traffic Impacts:** Traditional methods struggle to quantify the impact of overweight traffic on pavement life accurately. There is a lack of comprehensive analysis of axle loads and their contributions to pavement distress, such as cracking and rutting. Current regulatory measures are not well-informed by precise data on how overweight vehicles affect pavement service life.
3. **Dynamic Axle Loads and Uneven Surfaces:** Longitudinal unevenness in pavements results in dynamic axle loads that traditional models fail to account for adequately. This leads to inaccurate predictions of pavement fatigue and deterioration, as existing mechanistic-empirical models do not incorporate these dynamic loading conditions.
4. **Pavement Temperature Prediction:** Many temperature prediction models rely on surface temperature data, neglecting deeper pavement layers and comprehensive environmental factors. This results in vulnerabilities in pavement design and increased maintenance costs.
5. **Weigh-in-Motion System Accuracy:** Vehicle wandering introduces significant measurement errors in traditional WIM systems, compromising the accuracy of vehicle weight data. Existing systems lack integration with advanced technologies like computer vision and artificial neural networks, limiting their effectiveness.
6. **Hybrid Systems for Improved Monitoring:** Image-capturing systems for vehicle monitoring depend on manufacturer-provided data, leading to potential inaccuracies. There is a need for hybrid systems that combine in-pavement sensors and image-capturing technologies to address the wander effect and improve measurement accuracy.

Based on the identified challenges, this study aims to develop innovative solutions to enhance the accuracy and reliability of pavement performance predictions and vehicle weight monitoring. The specific objectives are:

1. **Develop Support Vector Regression Models:** Create advanced SVR models to accurately predict pavement performance under various traffic loading conditions by incorporating axle load spectra and dynamic loading effects.
2. **Leverage Machine Learning for Overweight Traffic Analysis:** Utilize machine learning techniques to analyze the impact of overweight traffic on asphalt pavement life, providing precise data for regulatory measures and pavement management.
3. **Incorporate Dynamic Axle Load Spectra in Mechanistic Models:** Integrate dynamic axle load spectra due to longitudinal unevenness into mechanistic-empirical models to improve predictions of pavement performance and lifespan.
4. **Create Advanced Temperature Prediction Models:** Develop temperature prediction models using multiple regression and artificial neural networks to provide accurate predictions across various pavement depths.
5. **Implement Hybrid WIM Systems for Accurate Weight Monitoring:** Design hybrid WIM systems that combine in-pavement sensors with computer vision to address the wander effect and improve vehicle weight measurement accuracy.
6. **Enhance Hybrid Systems with Advanced Technologies:** Further develop hybrid WIM systems by integrating computer vision with in-pavement sensors to mitigate the wander effect and adapt to varying vehicle conditions, enhancing weight monitoring accuracy and infrastructure management.

The remainder of this report is organized as follows. Chapter 2 details the data collection process from state Departments of Transportation (DOT), the Long-Term Pavement Performance (LTPP) program, and MnROAD, covering truck traffic data, pavement structure, climate conditions, and field experiments with sensors. Chapter 3 explores Support Vector Regression (SVR) for modeling traffic loading impacts, comparing traditional regression models and discussing the results, particularly concerning overweight trucks. Chapter 4 presents the use of Random Survival Forests to model traffic impacts, explaining the methodology and analyzing overweight traffic's effects on pavement life. Chapter 5 focuses on mechanistic-empirical analysis considering dynamic axle loads, evaluating their impact on pavement performance. Chapter 6 predicts asphalt pavement temperatures using regression and neural networks, evaluating weather factors and their influence on pavement temperatures. Chapter 7 assesses the vehicle wandering effect using GFRP-FBG sensors and camera systems, presenting experimental frameworks and results. Chapter 8 introduces a hybrid WIM system integrating computer vision with in-pavement sensors, presenting its framework, experimental results, and benefits in mitigating the wander effect. Chapter 9 concludes the study, summarizing findings, discussing implications for pavement management, and suggesting future research directions.

2. DATA COLLECTION AND PROCESSING

The LTPP program was established to collect pavement performance data to analyze various affecting factors, develop performance prediction models, and evaluate the effectiveness of pavement preservation and rehabilitation. Various pavement performance data have been analyzed, including specific pavement distresses, pavement condition index, surface roughness, friction considering the interaction between pavement material and structure, traffic loading, and environmental conditions.

2.1 Data Collection from State DOT

2.1.1 Truck Traffic Data from WIM

Weigh-in-motion devices can continuously capture and record GVW, axle load, and axle spacing with supplementary data including date, time, speed, lane of travel, and vehicle type. Axle load spectra and GVW from WIM database are critical inputs for mechanistic-based pavement design and pavement performance analysis. NJDOT has 95 WIM sites in the highway network. The axle load spectra recorded at 87 WIM sites for both directions were extracted from Vehicle Travel Information System (VTRIS) operated by Federal Highway Administration (FHWA) [72] .

The numbers of daily ESALs for flexible and rigid/composite pavement structures were calculated from WIM data based on load equivalency factors derived from AASHO road test [73]. Considering that WIM data was not recorded for every segment successively from 2000 to 2014, the daily ESALs were averaged for every five years. Figure 2.1 shows the frequency distribution of average annual daily ESALs for Interstate highways, US highways, and state highways, respectively. Interstate highways are part of the network of controlled-access highways for long-distance travel and freight transport. US highways are mainly consisted of major roads having the designation and numbering coordinated among the states over US. State highways are designed according to various standards or capacity and operated by state governments.

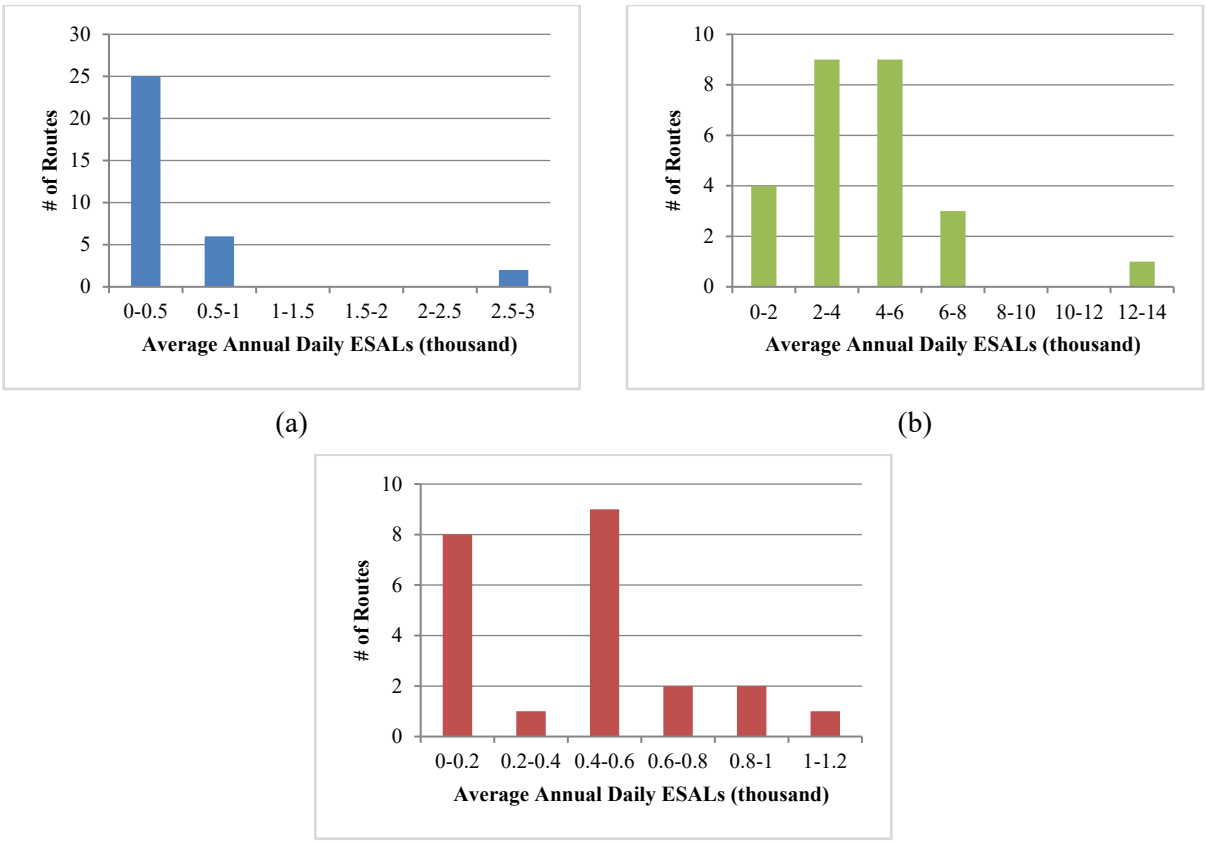

Figure 2.1 Frequency distribution of average annual daily ESALs on (a) state highways, (b) Interstate highways and (c) US highways in NJ

The number of single, tandem, tridem axles and axle load spectra were provided in the VTRIS system. Figure 2.2 shows single, tandem, and tridem axle load spectra of all trucks on Interstate highway Route 80 in the year of 2000. It indicated that single axles had the most axle loads around 5 kips, and the axle loads of tandem axles concentrated at 5 kips and 11 kips. Most tridem axles have loads between 18 and 20 kips. In previous works, Gaussian distribution was applied to fit the observed single and tridem axle load spectra, and the tridem axle load was usually not considered [74], [75]. In this study, the axle load spectra were fitted using Gaussian distribution, and the amplitude, mean, and standard deviation of Gaussian distribution were used to characterize the pattern of traffic loads. The Gaussian distribution fits peaks of axle load spectra and is given by Eq.1 [76] .

$$y = \sum_{i=1}^{n} a_i e^{\left[-\left(\frac{x-b_i}{c_i}\right)^2\right]} \quad (1)$$

Where, a_i is the amplitude; b_i is the centroid or location; c_i is the parameter related to the peak width; and n is the number of peaks to fit (n =1 for single and tridem axles; n = 2 for tandem axle).

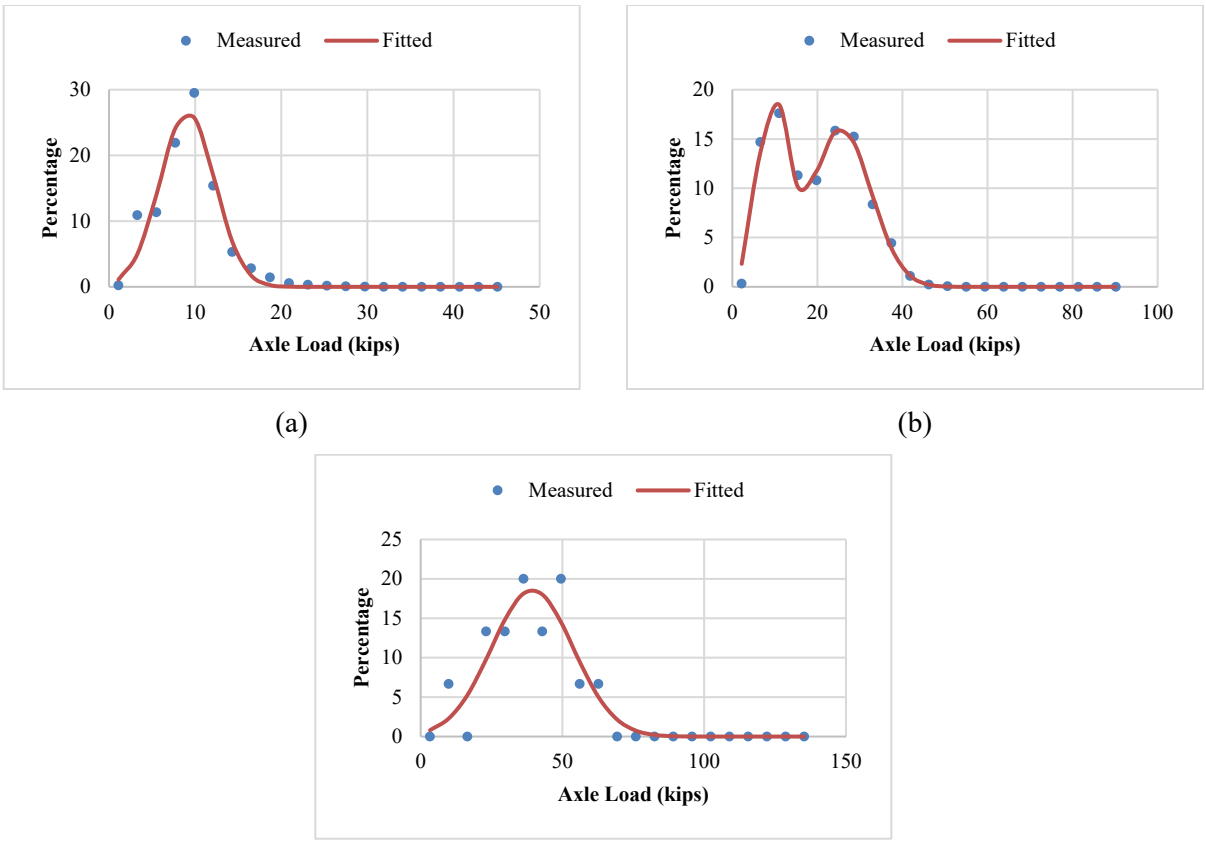

Figure 2.2 Gaussian distribution of axle load spectra of (a) single, (b) tandem, and (c) tridem axle on I-80 in 2000

2.1.2 Pavement Structure and Field Performance

The pavement structure and field performance data for the two-mile pavement segments nearby the WIM sites were collected from pavement management system of NJDOT. In general, 50% of highways in NJ are composite pavements, 40% are flexible pavements, and the remaining 10% are rigid pavements. Figure 2.3 shows the frequency distribution of thicknesses of flexible and composite/rigid pavements. For the majority of flexible pavements, the thickness of state highways, US highways, and Interstate highways are in the ranges of 2-4 inches, 4-6 inches, and 8-12 inches, respectively. For most of the composite and rigid pavements, the thickness of surface layer of state highways, US highways, and Interstate highways are in the ranges of 6-8 inches, 10-12 inches, and 10-14 inches, respectively.

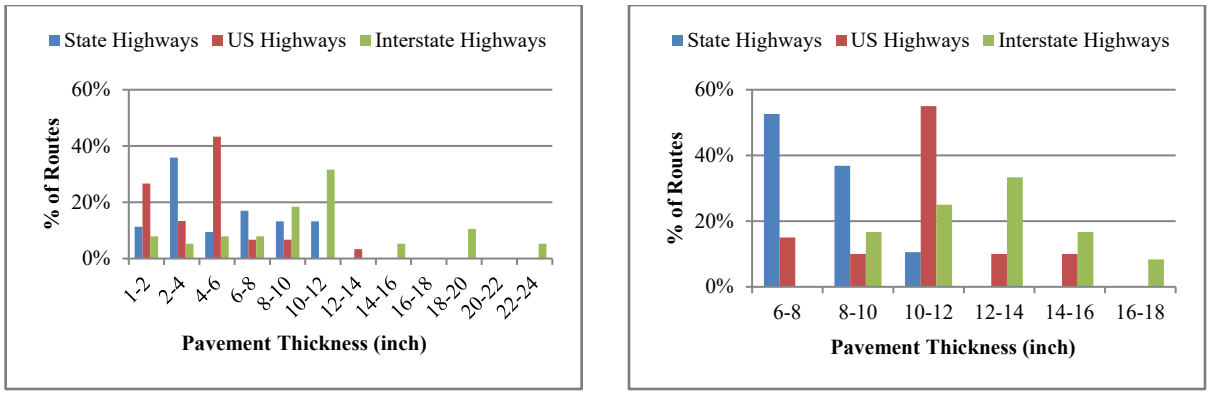

(a) (b)

Figure 2.3 Frequency distribution of (a) surface layer thickness of flexible pavement and (b) surface layer thickness of composite/rigid Pavement

Surface distress index (SDI) is a New Jersey standard used for decades in roadway assessment and considered the most indicative of functional adequacy to evaluate the system status. Pavement performance data in terms of SDI over years were used to estimate pavement service life after major rehabilitation treatments. The SDI has a scale of 0-5 and incorporates both non-load related distresses index (NDI) outside wheel paths and a load related distress index (LDI) in wheel path by manual survey [77]. Figure 2.4 shows an example of pavement deterioration showing SDI over years. It can be observed from that the SDI declines slowly during the first several years. Afterward, SDI starts to drop rapidly and finally decreases gradually to a small value. The SDI data indicated a nonlinear relationship with pavement age. NJDOT defines the pavement condition as poor when SDI < 2.4 or IRI > 2.7m/km and as good when SDI > 3.5 and IRI < 1.5m/km. In real practice, the terminal IRI values are much smaller than 2.7m/km when pavement life is reached based on the SDI threshold [78]. Therefore, the pavement service life in the study is determined as the period before the SDI drops to 2.4.

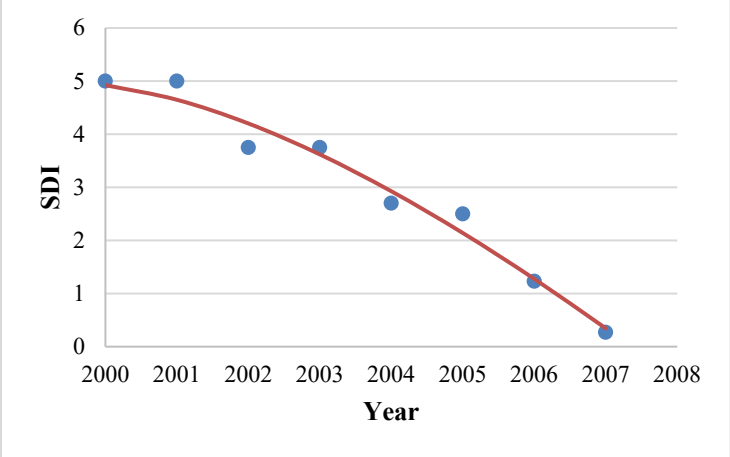

Figure 2.4 Example of deterioration trend of pavement performance (I-287A)

2.1.3 Climate Condition

The office of New Jersey State Climatologist provides average monthly air temperature data. The 21 counties in New Jersey were grouped into three districts: Northern New Jersey (11 counties), Southern New Jersey (10 counties), and Costal New Jersey. The freezing index (FI) is defined by the negative of the sum of all average daily temperatures below 32 °F within the given period, as shown Eq. 2 [8]. The FI was found to be 9.3 degree-days in Southern New Jersey, and 175.7 degree-days in Northern New Jersey. As the consequence of using average monthly air temperature instead of daily air temperature, the estimated FI is correspondingly smaller.

$$FI = \sum \left[\frac{1}{2}\left(T_{Max} - T_{Min}\right) - 32 \right] \times n_i \tag{2}$$

Where, FI is accumulative FI, degrees Fahrenheit (°F) degree-days; T_{max} is the maximum monthly temperature in month i, °F; T_{min} is the minimum monthly temperature in month i, °F; and n_i is days in month i when average monthly temperature is below freezing (32°F).

2.2 Data Collection from LTPP

2.2.1 Data Elements from LTPP Database

The LTPP program was established to collect pavement performance data as one of the major research areas of the Strategic Highway Research Program (SHRP). It provides technical knowledge about available pavements and seeks models that can better explain pavement performance. The LTPP program includes the general pavement study (GPS) and the specific pavement study (SPS). LTPP InfoPave is a web interface for the LTPP database that is used to deliver data sets of features generated by users.

Totally 128 pavement sections in a SPS-5 study located in 12 states were used in this study. The SPS-5 study was conducted to develop improved methodologies and strategies for the rehabilitation of flexible pavements. Each LTPP test section was approximately 3.5 meters wide per lane and 152.4 meters long [79]. The selected pavement sections were located at four climate regions: dry freeze (Colorado, Montana), dry no freeze (Arizona, California, and New Mexico), wet freeze (Maine), and wet no freeze (Florida, Maryland, Mississippi, New Jersey, Oklahoma, Texas) [80]. The climate region of the pavement section was considered as an environmental factor in the analysis.

The load-related pavement distress data, including alligator cracking, longitudinal cracking at wheel-path, and rut depth of the analyzed pavement sections were identified and extracted from LTPP database. The pavement age of AC overlay at the time of distress survey was determined by comparing the survey time and construction time of the rehabilitation. Fatigue cracking and longitudinal cracking were measured at different severity levels (high, medium, and low). Therefore, the overall cracking needed to be estimated using weight factors. The weight factors for low-, medium-, and high-severity cracking were determined to be 0.2, 0.3, and 0.5, respectively, which were approximated based on the deduct value curves used in calculating pavement condition index [81]. The initial international roughness index (IRI) score after construction was considered as the variable indicating construction quality in the analysis [82].

Multiple data buckets for desired variables were downloaded from LTPP InfoPave and then organized to create a relational database. Table 2.1 summarizes the LTPP database variables and the extracted data elements in this study, including pavement age, traffic (number of axles and axle load distribution),

pavement layer thickness, climate region, overlay treatment (milling and overlay thickness), construction quality, and pavement distresses (alligator cracking, longitudinal cracking at wheel-path, and rutting).

Table 2.1 LTPP InfoPave database tables and extracted data elements

Variables	Symbol	Range	Unit	Relevant Tables in InfoPave
Pavement age		0.02~24.9	year	EXPERIMENT_SECTION
Number of single axles	Single	65~4541	N/A	YY_AX
Number of tandem axles	Tandem	1~4701	N/A	YY_AX
Number of tridem axles	Tridem	0~100	N/A	YY_AX
Range of single axle loads	Single	0-39	kips	YY_AX
Range of tandem axle loads	Tandem	0-78	kips	YY_AX
Range of tridem axle loads	Tridem	0-117	kips	YY_AX
Thickness of AC layer	AC	2.8~16	inch	TST_L05B
Thickness of bound base layer	TB	0~15	inch	TST_L05B
Thickness of unbound base layer	GB	0~20.7	inch	TST_L05B
Thickness of bound subbase layer	SS	0~66	inch	TST_L05B
Thickness of unbound base layer	GS	0~234	inch	TST_L05B
Climate region	Climate	1~4	Categorical	EXPERIMENT_SECTION
Improvement type	IMP_TYPE	N/A	Categorical	CONSTRUCTION_EVENTS_EXP
Overlay thickness	IMP_h	0.7~7.8	inch	CONSTRUCTION_EVENTS_EXP
Mill thickness	Mill	0.45~4.0	inch	AC_MILLING_EXP
IRI after AC overlay	IRI	0.44~1.8	mm/m	MON_HSS_PROFILE_SECTION
Alligator cracking		0~808 (L) 0~424 (M) 0~817 (H)	m^2	MON_DIS_AC_REV
Longitudinal cracking		0~271 (L) 0~153 (M) 0~48 (H)	m	MON_DIS_AC_REV
Rut depth		1~25	mm	MON_T_PROF_INDEX_SECTION

2.2.2 Analysis of Axle Load Spectra

The traffic data are available in the LTPP database in terms of axle configuration and weight collected through weigh-in-motion (WIM) stations [83]. Multi-year traffic data for the selected pavement sections were used in the analysis. The same traffic data was used in successive years for the pavement sections where traffic data was not available for certain years.

As compared to the number of equivalent single axle load (ESAL), axle load spectra provide better representation of traffic loading by showing the distribution of axle loads for each type of axle configuration. Given the apparent bell-shaped plot, the axle load spectra were fitted using Gaussian distribution, as shown in Eq. 1 [84]. The amplitude, mean, and standard deviation of the Gaussian distribution were utilized to characterize the pattern of traffic load, which provides a simplified but efficient way to take detailed axle load distributions into consideration [85], [86].

Table 2.2 presents the summary of variables related to the total number of axles and fitted Gaussian distributions of axle load spectra for all the pavement sections used in this study. Note that tridem axle load spectra were not included in the analysis because of an inconsistent trend of axle load distributions. Because the number of tridem axles was small, this exclusion is believed not to affect analysis results.

Table 2.2 Summary of Gaussian distribution model parameters for axle load spectra

Variable	Symbol	Range of Values
Amplitude of single axle load spectrum	a	7.94~37.98
Mean of single axle load spectra	b	4.08~11.48
Standard deviation of single axle load spectrum	c	0.68~5.38
Amplitude of tandem axle load spectrum (peak 1)	a1	2.44~15.9
Mean of tandem axle load spectra (peak 1)	b1	8.09~25.23
Standard deviation of tandem axle load spectrum (peak 1)	c1	1.94~9.64
Amplitude of tandem axle load spectrum (peak 2)	a2	3.22~20.15
Mean of tandem axle load spectra (peak 2)	b2	16.76~36.91
Standard deviation of tandem axle load spectrum (peak 2)	c2	1.74~12.55

2.3 Data Collection from MnROAD

To validate the proposed hybrid WIM system, a field study was conducted on Interstate 94 westbound located on the MnROAD mainline between exits 201 and exit 194 in Albertville, MN, USA, with sensors meticulously positioned just beneath the asphalt pavement road surface. This section provides an overview of the field experimental, encompassing pertinent details about the field's location, pavement characteristics, and the determination of dynamic modulus for the specific road segment. Additionally, it outlines the deployment of sensors, their positioning, and methodological setup of the experiment.

2.3.1 Field Experiment Setup

The field tests took place on a designated road within the MnROAD research facility, an establishment dedicated to pavement research and equipped with a range of pavement materials. Administered by the Minnesota Department of Transportation, MnROAD encompasses several roadways which each contain several test sections, with the majority of test sections located on the MnROAD Mainline – 3.5 miles of I-94 WB interstate), Old I-94 Westbound - 3.5 miles of the original westbound I-94 build during the 1970s, and a 2.5-mile low traffic volume test track. This extensive site boasts over 80 distinct test sections strategically situated along both the mainline and original westbound I-94 segments. The field test for this study was carried out on a specified test section, as highlighted in Figure 2.5.

Figure 2.5 Test section location on MnROAD Mainline

The flexible pavement cross section of the test section is shown in Figure 2.6(a), and is composed of hot-mix asphalt (HMA), MnDOT Class 5 granular base, MnDOT Class 3 sub-base, selected granular layer, and clay loam [87]. The GFRP-FBG sensors were strategically positioned above the MnDOT Class 5 granular base, as illustrated in Figure 2.6 (b). To ensure the stability and integrity of their placement during subsequent construction stages, a thin layer of HMA was applied to gently secure the sensors in their designated locations. This safeguarding step was undertaken before the laying of the 0.127-meter-thick HMA layer, as shown in Figure 2.6 (c). This comprehensive approach guaranteed that the sensors remained in their intended positions throughout the pavement construction process.

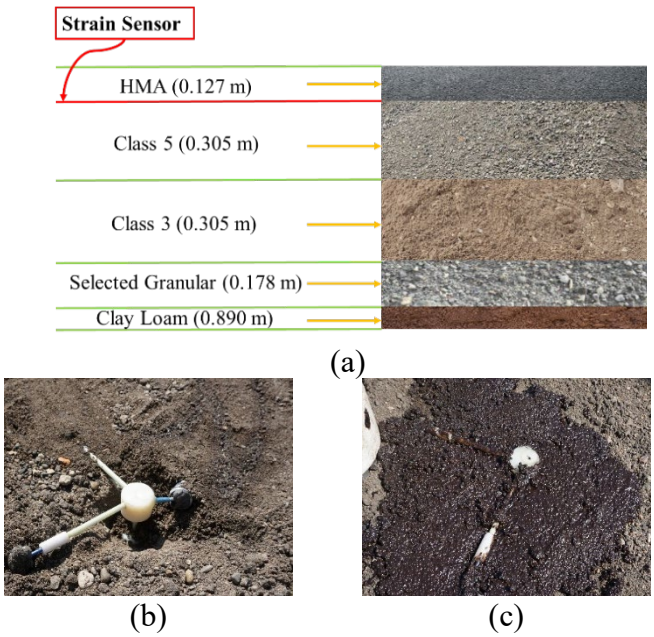

Figure 2.6 (a) Flexible pavement cross section of the test section; (b) GFRP-FBG sensor placement above MNDOT class 5 granular base; (c) safeguarding GFRP-FBG sensor placement with HMA layer

Results from previous asphalt mixture performance testing experiments conducted by MnROAD and National Center for Asphalt Technology, obtained from MnROAD, were utilized in this study. The testing involved two specimens with 150 mm diameter and 38 mm height (the same material as the warm mix asphalt layer of the test section), which were used in dynamic modulus testing. The dynamic modulus testing consisted of eight frequencies and three temperatures, which generated 24 temperature and frequency combinations. The average results from testing the two test specimens are shown in Table 3.1 2.3 [88].

Table 2.3 Average dynamic modulus of elasticity value for test section [88]

Temp (℃)	25 Hz	10 Hz	5 Hz	1 Hz	0.5 Hz	0.1 Hz	0.05 Hz	0.01 Hz
-12	15.520	11.830	10.410	9.490	9.000	8.190	7.900	6.990
12	7.580	7.830	7.340	4.550	3.990	2.120	1.570	0.570
36	1.660	1.350	1.070	0.420	0.300	0.160	0.130	0.040

*unit is GPa

2.3.2 Field Installed GFRP-FBG Sensors and Experimental Setup

The layout of the proposed hybrid WIM system, depicted in Figure 2.7, involves the utilization of a camera, two GFRP-FBG sensors, and one temperature compensation sensor. Either three-dimensional (3D) or one-dimensional (1D) GFRP-FBG sensors as shown in Figure 8 (b, c) [89] can be used. In the case of the 3D GFRP-FBG sensor, it integrates three distinct components for data collection along vertical, longitudinal, and transverse directions. The longitudinal component aligns parallel to the wheel path. The transverse component is perpendicular to it, and a vertical dimension extends to a point at the asphalt surface. Based on previous study [89], the longitudinal, transverse, and vertical segments possessed dimensions can be 4.064, 4.064, and 3.048 cm, respectively, with an FBG positioned at the

center of each component. Among a 3D GFRP-FBG sensor, the vertical component of the 3D sensor detects proximity but faces alignment challenges with passing vehicles, while the transverse aspect depends less on the matrix and requires a reasonable wheel load radius [58]. Conversely, the longitudinal part shows high sensitivity, less matrix independence, and an ample detection range, making it ideal for WIM measurements along the wheel path. Hence, the longitudinal component usually is chosen for evaluating high-speed WIM feasibility post field assessment. For an 1D GFRP-FBG, it can be positioned strategically in the longitudinal direction for wheel load detection.

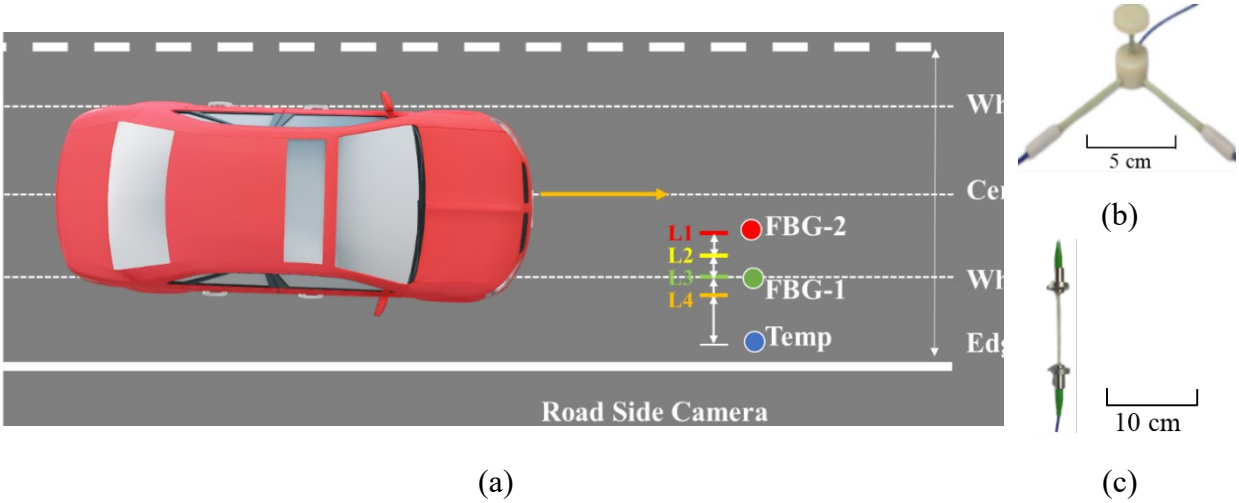

Figure 2.7 Photo of the (a) Practical layout of the hybrid WIM system; (b) 3D; and (c) 1D GFRP-FBG sensors [89]

Previous research on the GFRP-FBG sensor [90], the elastic modulus (E_0) and outer radius (r_0) of the optical fiber, shear modulus (G_{GFRP}) and outer radius (r_{GFRP}) of the packaging layer (GFRP), and outer radius of the host material layer (r_h) are shown in Table 2.4. The gauge length of the longitudinal (l_f), transverse, and vertical components of the optical fiber were 70 mm, 70 mm, and 14 mm, respectively. The shear modulus of the host material layer (which is HMA in this study) was calculated based on the dynamic modulus of elasticity and Poisson's ratio of the host material. This calculated shear modulus and the parameters depicted in the Table were then employed to calculate the measurement error attributable to the host material. This correction was subsequently applied to adjust the strain calculations obtained from the sensor.

Table 2.4 OFBG sensor strain transfer parameters

	E_0 (GPa)	r_0 (mm)	G_{GFRP} (GPa)	r_{GFRP} (mm)	r_h (mm)	l_f (mm)
Longitudinal	70	0.0625	5.0	2.5	25	70

The experimental design was targeted to evaluate vehicle performance at various positions with driving speeds of 16.093 km/h (10 mph), 32.187 km/h (20 mph), 40.280 km/h (30 mph), and 64.374 km/h (40 mph). A semi-truck passed over the two FBG sensors located at positions L1 and L3. The same driver drove the truck over each position a total of seven times, aiming to align the wheels directly above the sensor positions.

However, ensuring precise control over the truck's movement within the specific areas and at the designated speed presented a challenge, particularly when the two locations were in close proximity. Consequently, both the sensor data and captured images were employed to accurately calculate the vehicle's exact speed and location as it passed through the specified points.

The field test utilized a semi-truck from the MnROAD facility, which had a total gross weight of 354,523 N. The vehicle configuration is illustrated in Figure 2.8. This study specifically concentrated on weight measurement of the first axle equipped with a single tire.

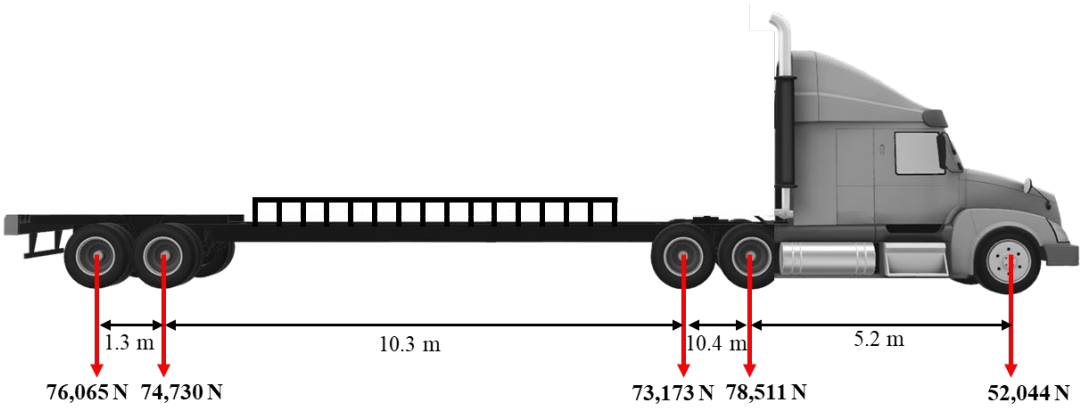

Figure 2.8 Layout of semi-truck used in MnROAD field test

3. SUPPORT VECTOR REGRESSION OF TRAFFIC LOADING IMPACT ON PAVEMENT PERFORMANCE

This chapter used SVR model to quantify the impact of traffic loading on pavement performance based on field data. Pavement structure and condition data were collected from pavement management system. Truck traffic data were extracted from WIM database and the characteristics of axle load spectra were analyzed. The SVR method was applied and compared to the traditional multi-variable nonlinear regression method in terms of prediction accuracy and error. The proposed pavement performance models were further used to analyze pavement deterioration caused by overweight trucks with different truck traffic and axle load distributions.

3.1 Traditional Regression Models

Traditional nonlinear regression models were first used to investigate traffic loading impact on pavement performance. The average daily ESALs and axle load spectra were considered as traffic variables in the nonlinear regression model to analyze and predict pavement performance. A total of 5,481 data points were used to derive the regression models. The number of data points for flexible pavement structure on state highways, Interstate highways, and US highways were 1,310, 1,368, and 653, respectively. The number of data points for composite and rigid pavement structure on state highways, Interstate highways, and US highways were 402, 960, and 788, respectively. The data points were categorized into two groups: 80% for model training and 20% for model validation. Bootstrap procedure, a resampling technique for the validation of model performance, was conducted to assess the influence of each observation on each parameter estimate. The shape of bootstrap distribution was examined, and the mean and confidence intervals based on the sampling distribution were determined. Confidence intervals were used to evaluate the practical significance of the estimate for the population parameter. The pavement performance models developed by relating SDI to pavement age, average daily ESALs, and freezing index, as shown in Eq. 3.

$$SDI_t = exp(a - b \times Log(T) \times Age - c \times Log(FI) \times Age) \quad (3)$$

Where, SDI_t is surface distress index in the tth year; Age is pavement age; T is average annual daily ESALs; FI is freezing index; and a, b, and c are model coefficients.

Table 3.1 summarizes the coefficients and R square values of the regression models of flexible and composite/rigid pavements for state highways, Interstate highways, and US highways, respectively. The R square value varies from 0.51 to 0.70 depending on the pavement structure and route type.

Table 3.1 Coefficients and R^2 values of regression model based on average daily ESALs

Pavement Type	Highway Type	a	b	c	R-square (training)	R-square (validation)
Flexible Pavement	State Highway	1.717	0.009	0.017	0.50	0.53
	Interstate Highway	1.703	0.002	0.025	0.71	0.68
	US Highway	1.742	0.021	0.006	0.58	0.50
Composite/Rigid Pavement	State Highway	1.753	0.020	0.024	0.56	0.62
	Interstate Highway	1.754	0.009	0.013	0.53	0.53
	US Highway	1.838	0.034	0.001	0.62	0.66

In order to improve the accuracy of prediction, another pavement performance model was developed by correlating SDI to pavement age, freezing index, the number of axles, and the fitted Gaussian distribution of axle load spectrum for each axle type, expressed by Eq.4.

$$SDI_t = exp\big(a - \big((bA_1 + cM_1 + dSD_1) \cdot log(N_1) + (eA_2 + fM_2 + gSD_2 + e_2A_3 + f_2M_3 + g_2SD_3) \cdot log(N_2) + (hA_4 + iM_4 + jSD_4) \cdot log(N_3)\big) \cdot Age - p \cdot log(FI) \cdot Age\big) \quad (4)$$

Where, *N1, N2, N3* are the number of single, tandem, and tridem axles; A_1, M_1, SD_1 are amplitude, location, and peak width of single axle load spectrum as shown in Figure 2.2 (a); $A_2, M_2, SD_2, A_3, M_3, SD_3$ are amplitude, location, and peak width of tandem axle load spectrum for the first peak and second peak as shown in Figure 2.2 (b); A_4, M_4, SD_4 are amplitude, location, and peak width of tridem axle load spectrum as shown in Figure 2.2 (c); and *a, b, c, d, e, f, g, e2, f2, g2, h, i, j,* and *k* are model coefficients.

Table 3.2 presents the coefficients of pavement performance models for state highways, Interstate highways, and US highways, respectively. The mean absolute error (MAE), root mean square error (RMSE), and coefficient of determination (R-square) were considered as the error metrics to evaluate the accuracy of fitting model, as shown in Table 3.3. The R-square values varied from 0.51 to 0.71 depending on pavement structure and highway type. The comparison between the R-square values of two nonlinear regression models (Eq. 3 and 4) indicated that the accuracy of pavement performance prediction was improved by considering the number of axles and the fitted Gaussian distribution of axle load spectra in the model. However, the R-square values are still not very high.

Figure 3.1 illustrates the actual observed and predicted SDI using the nonlinear regression models expressed by Eq.4, respectively, for different pavement structures and highway types. An apparent bias was observed in the predicted SDI with low accuracy. Therefore, more accurate predictive models are needed to investigate the impact of traffic loading on the deterioration trend of pavement performance.

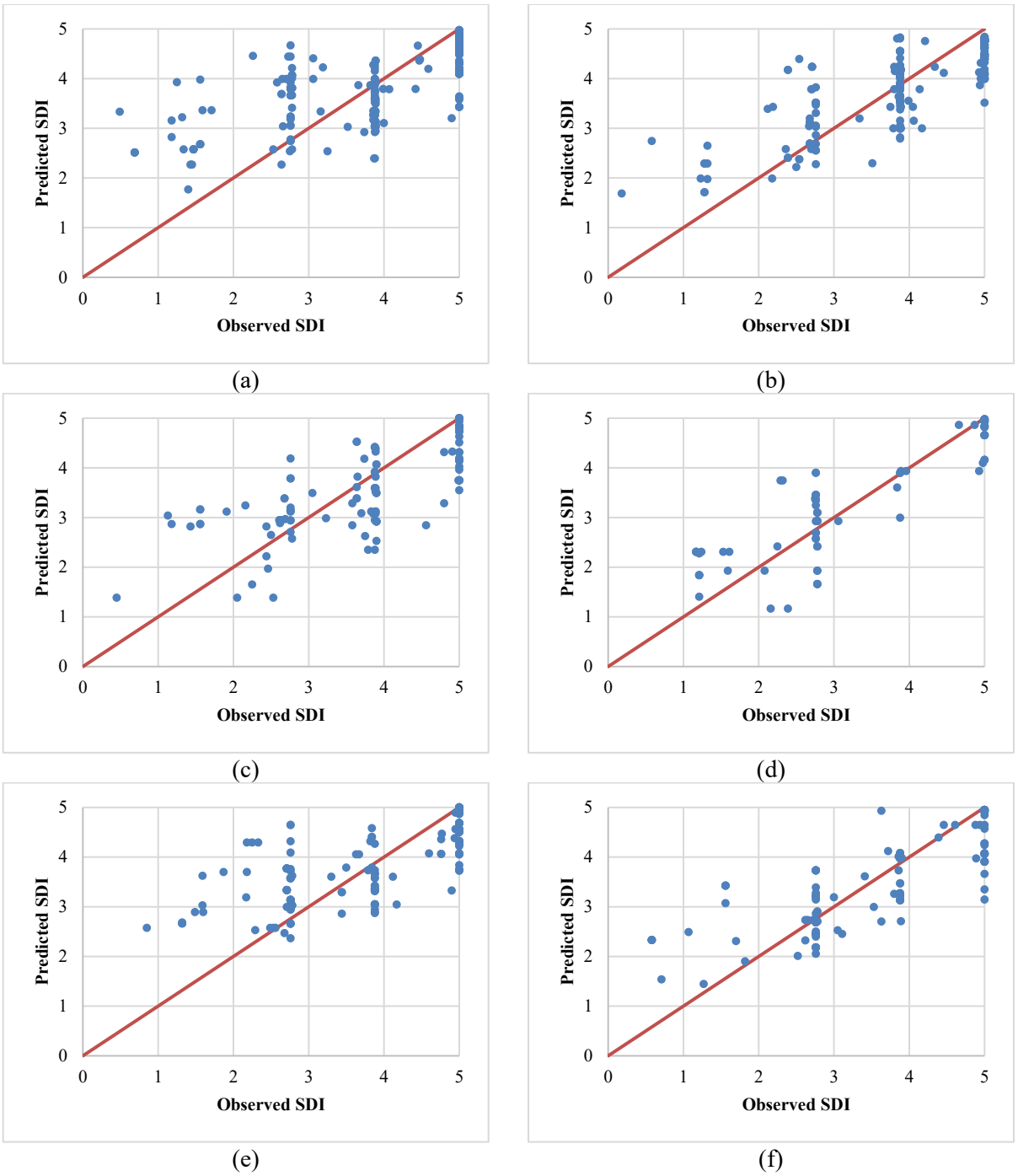

Figure 3.1 Actual observed and fitted SDI based on multiple nonlinear regression models for flexible pavement structure on (a) state highways; (b) Interstate highways; (c) US highways; and composite/rigid pavement structure on (d) state highways; (e) Interstate highways; (f) US highways.

Table 3.2 Coefficients of regression models based on axle load spectra

Pavement Type	Highway Type	a	b	c	d	e	f	g
Flexible Pavement	State	1.712	-	-	-	5.1E-04	1.1E-03	2.6E-03
	Interstate	1.670	-	-	-	-	-	-
	US	1.735	-	1.3E-02	-1.4E-03	-	-	-
Composite/Rigid Pavement	State	1.784	1.2E-03	-	7.9E-04	-	-4.5E-03	-
	Interstate	1.754	-	-	-	-	-8.2E-03	8.2E-03
	US	1.846	-	9.9E-03	-	0.001	-	-
Pavement Type	Highway Type	e2	f2	g2	h	i	j	p
Flexible Pavement	State	-2.0E-04	-	-	-	-	-	3.9E-02
	Interstate	-	-	-	-	9.6E-04	-1.0E-02	7.6E-02
	US	-	-	-	-	-	-	6.5E-03
Composite/Rigid Pavement	State	4.1E-03	-	8.0E-03	-	-	-	-
	Interstate	8.8E-04	3.5E-03	-	-	-	-	2.3E-02
	US	-	2.7E-04	-	1.7E-03	-	-	8.3E-03

Table 3.3 Error metric of regression model based on axle load spectra

Structure	Route	R-square (training)	RMSE (validation)	MAE (validation)	R-square (validation)
Flexible	State	0.51	0.82	0.62	0.51
	Interstate	0.71	0.58	0.43	0.68
	US	0.63	0.76	0.60	0.63
Composite/Rigid	State	0.68	0.63	0.47	0.68
	Interstate	0.58	0.74	0.56	0.58
	US	0.66	0.68	0.49	0.66

3.2 Support Vector Regression Method

3.2.1 Principle of Support Vector Regression

The selection of machine learning algorithms needs to consider the size of dataset, the number of potential influential variables, linearity, training time, model accuracy, and interpretability of output. Support vector method (SVM) is a supervised learning model which is commonly applied for classification and regression analysis. SVM is an efficient approach to derive pavement performance model with low generalization error and easy interpretation of results, especially when the dataset is small and the correlation is nonlinear [11], [12]. Since the size of dataset in this study was not large, SVM approach was used to develop the pavement performance models.

SVM produces nonlinear boundaries by constructing a linear boundary in a large, transformed version of the feature space. The basic principle behind the linear SVM is to find an optimal separating hyperplane creating the biggest margin between the training data. The closest training points to the hyperplane are called support vectors. SVM can also be used as regression method rather than classification method, this application is also called as SVR [91]. SVR uses the same principles as SVM but provides the flexibility to find the appropriate hyperplane in higher dimensions to regress the data and customize controlled errors in an acceptable range. Its main objective is to decide a decision boundary at a specific distance from the original hyperplane such that data points closest to the hyperplane or the support vectors are within that boundary line by approximating a function to seek the narrowest ϵ-tube centered around the data [92], as shown in Figure 3.2.

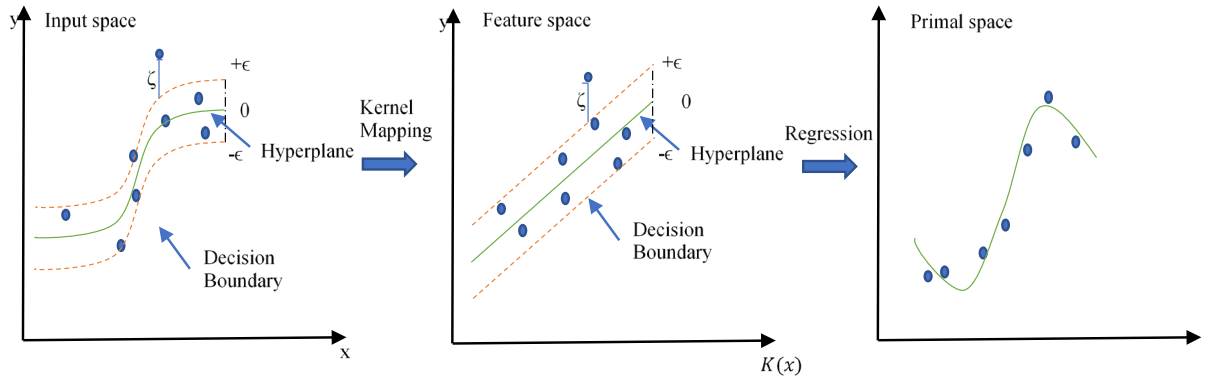

(a) (b) (c)

Figure 3.2 Principle of SVR

For the training data consisted of N pairs (x_1, y_1), (x_2, y_2), …, (x_N, y_N), with $x_i \in R^p$ and $y_i \in \{-1,1\}$. Define a hyperplane by Eq. 5.

$$\{x : f(x) = x^T\beta + \beta_0 = 0\} \tag{5}$$

where, β is a unit vector $\|\beta\|=1$.

A classification rule induced by *f(x)* is defined by Eq. 6:

$$G(x) = \mathrm{si}\,gn\left[x^T\beta + \beta_0\right] \tag{6}$$

where, *f(x)* gives the signed distance from a point x to the hyperplane $f(x) = x^T\beta + \beta_0 = 0$. The classes are separated, so a function $f(x) = x^T\beta + \beta_0$ with $y_i f(x_i) > 0\ \forall i$. Thus, it is available to find the hyperplane that maximizes the margin between training data for different classes. The optimization problem is defined by Eq. 7.

$$\max_{\beta,\beta_0,\|\beta\|=1} M \tag{7}$$

Subject to

$$y_i(x_i^T\beta + \beta_0) \geq M, i = 1,...,N \tag{8}$$

The band is M units away from the hyperplane on either side, and then 2M units wide, which is called the margin. Therefore, optimization problem can be more conveniently phrased as shown in Eq. 9 and 10.

$$\min_{\beta,\beta_0} \|\beta\| \tag{9}$$

Subject to

$$y_i(x_i^T\beta + \beta_0) \geq 1, i = 1,\ldots,N \tag{10}$$

Noted that $M = \frac{1}{\|\beta\|}$. Eq. 9-10 are the common approach of expressing the support vector criterion for separable data. When SVM is used for regression to estimate □, the minimization of Eq.11 is considered with Eq. 12. SVM regression is considered as a nonparametric technique since it is dependent on kernel functions, which will be introduced in the following section.

$$H(\beta,\beta_0) = \sum_{i=1}^{N} V\big(y_i - f(x_i)\big) + \frac{\lambda}{2}\|\beta\|^2 \tag{11}$$

Where, ϵ - insensitive error function is:

$$V_\epsilon(r) = \begin{cases} 0 & if\ |r| < \epsilon \\ |r| - \epsilon & otherwise \end{cases} \tag{12}$$

Assume that the classes are overlapped in feature space. Overlap is solved by maximizing M allowing some points to be on the inaccurate side of the margin. Define the slack variables $\xi = (\xi_1, \xi_2, \ldots, \xi_N)$, and drop the norm constraints on β to write the Eq. 10 in the equivalent form:

$$\min_{\beta,\beta_0} \|\beta\| \ \text{ Subject to } \begin{cases} y_i(x_i^T\beta + \beta_0) \geq 1 - \xi_i \forall i \\ \xi_i \geq 0, \sum \xi_i \leq constant \end{cases} \tag{13}$$

The convex optimization in Eq.13 is solved using Lagrange multipliers, and the Lagrange (primal) function is:

$$L_p = \frac{1}{2}\|\beta\|^2 + C\sum_{i=1}^{N}\xi_i - \sum_{i=1}^{N}\alpha_i\left[y_i\left(x_i^T\beta + \beta_0\right) - (1-\xi_i)\right] - \sum_{i=1}^{N}\mu_i\xi_i \tag{14}$$

Which minimize L_p with respect to $\beta, |\beta_0$ and ξ_i. *C* is the "cost" parameter which replaces the constant in Eq.13. Setting the respective derivatives to zero, we can get

$$\beta = \sum_{i=1}^{N}\alpha_i y_i x_i \tag{15}$$

$$\beta_0 = \sum_{i=1}^{N}\alpha_i y_i \tag{16}$$

$$\alpha_i = C - \mu_i, \forall i \tag{17}$$

The Lagrangian dual objective function can be derived by substituting Eq.15-17 into Eq. 14 and expressed by Eq.18 which gives a lower bound on the objective function for any feasible point. The optimization problem in Eq. 14 can be solved in a special approach by only involving the input feature via inner products using the transformed feature vectors $h(x_i)$. Then the Lagrangian dual objective function can be expressed by Eq.19.

$$L_D = \sum_{i=1}^{N}\alpha_i - \frac{1}{2}\sum_{i=1}^{N}\sum_{i\prime=1}^{N}\alpha_i\alpha_{i\prime}\, y_i y_{i\prime} x_i^T x_{i\prime} \tag{18}$$

$$L_D = \sum_{i=1}^{N}\alpha_i - \frac{1}{2}\sum_{i=1}^{N}\sum_{i\prime=1}^{N}\alpha_i\alpha_{i\prime}\, y_i y_{i\prime}\langle h(x_i), h(x_{i\prime})\rangle \tag{19}$$

From Eq.15, the solution function *f(x)* can be written by:

$$f(x) = h(x)^T\beta + \beta_0 = \sum_{i=1}^{N}\alpha_i y_i\langle h(x_i), h(x_{i\prime})\rangle + \beta_0 \tag{20}$$

The knowledge of the kernel function can be used to solve the problem in Eq.19-20 using inner products without specifying the transformation *h(x)*, as illustrated in Figure 3.2 (a)-(b).

$$K(x, x') = \langle h(x), h(x')\rangle \tag{21}$$

Which calculates inner products in the transformed space. K is supposed to be a symmetric positive definite function.

3.2.2 Results and Discussion

Similar to the nonlinear regression model, the SVR model was developed by relating SDI to pavement age, FI, and truck traffic. The average daily ESALs and fitted Gaussian distribution of axle load spectra were considered as traffic variables, respectively. The data points were categorized into two groups: 80% for model training and 20% for model validation to evaluate the performance of retrained model. In Python, scikit-learn is a widely used library for implementing machine learning algorithms. The sklearn.svm module was utilized to implement SVR algorithm (Python Software Foundation). Parameter values in the SVR models were optimized using grid search with k-fold cross-validation. The k-fold cross-validation is a resampling procedure in applied machine learning to estimate the skill of a model on unseen data. In general, it provides a less biased or less optimistic estimate of the model skill than other validation methods [93]. Kernels were used in SVR to solve nonlinear regression problems through decreasing the complexity of calculations by providing an chance to linearly deal with nonlinear functions in high-dimensional spaces [94]. Different kernels, including linear, radial basis function, sigmoid, and universal Pearson VII function, were considered in the model optimization [95]. Radial basis function kernel was found work best in the dataset through trial analysis. The radial basis function is expressed by Eq.22.

$$K(x, x') = exp(-\gamma \|x - x'\|^2) \tag{22}$$

where, γ is constant.

Table 3.4 summaries the cross-validation results of SVR when different traffic variables were considered in the model. The score was used to calculate the coefficients of determination (R-square values) for the evaluation of the SVR model performance. The mean_squared_error and mean_absolute_error from sklearn.metrics module were imported to compute the Root Mean Square Error (RMSE) and mean absolute error (MAE) values, respectively (Python Software Foundation). By applying SVR method, the coefficients of determination (R-square values) were found significantly increased as compared to the traditional nonlinear regression models. The MAE decreased to 0.17-0.38 and the coefficient of determination (R-square) increased to 0.71-0.93. The predictive models for flexible pavements on Interstate highway and composite/rigid pavements on US highway presented better accuracy than the other highway types. Compared to the nonlinear regression models, the SVR models could capture more complicated relationships in the original feature space between datapoints without computing the coordinates of the data in a higher dimensional space by applying kernel tricks. On the other hand, the fitting accuracy was further improved by involving the number of axles and fitted Gaussian distribution of axle load spectra in the SVR model, except for the flexible pavement on US highway. Thus, it was recommended to use the number of axles and the fitted Gaussian distribution of axle load spectra to develop SVR model and predict pavement performance. However, the SVR model based on average daily ESALs provided a simplified way with acceptable accuracy to investigate the influence of traffic loading on pavement deterioration.

Table 3.4 Cross-validation results of SVR with different variables

Model Variables	Pavement Type	Highway Type	R-square (training)	RMSE (validation)	MAE (validation)	R-square (validation)
Age, FI, ESALs	Flexible	State	0.86	0.46	0.25	0.85
		Interstate	0.86	0.41	0.22	0.84
		US	0.83	0.54	0.34	0.79
	Composite/Rigid	State	0.87	0.58	0.32	0.80
		Interstate	0.84	0.58	0.30	0.72
		US	0.85	0.45	0.24	0.88

Figure 3.3 presents the comparison of actual observed and predicted SDI values for the validation data set by using the SVR models based on the fitted Gaussian distribution of axle load spectra and the number of axles. As compared to Figure 3.1, the SVR method shows significant improvement on the accuracy of performance prediction.

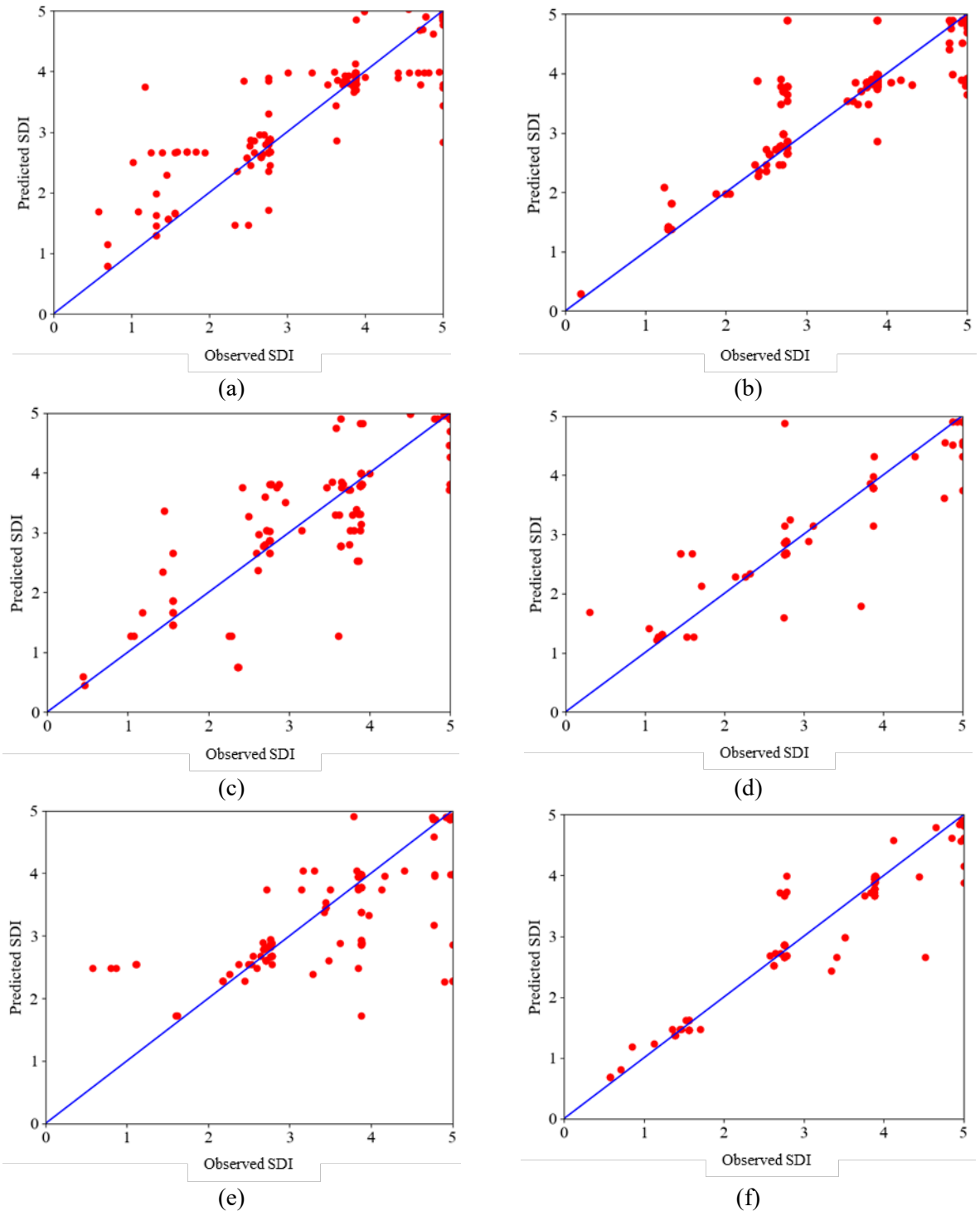

Figure 3.3 Actual observed and fitted SDI based on SVR models for flexible pavement structure on (a) state highways; (b) Interstate highways; (c) US highways; and composite/rigid pavement structure on (d) state highways; (e) Interstate highways; (f) US highways.

The developed SVR models could be applied to predict the pavement performance over year after reconstruction and derive the fragility curve of pavement section. The maintenance and rehabilitation could be scheduled based on the estimated deterioration trend of pavement section to avoid the pavement failure. Moreover, sensitivity analysis could be conducted to investigate the impact of traffic and environmental factors on pavement deterioration. The developed SVR models were further used to analyze the impact of overweight trucks on pavement deterioration in the following section.

3.3 Impact of Overweight Truck on Pavement Deterioration

The developed SVR models were utilized to investigate the impact of overweight truck traffic on pavement damage. Currently, NJDOT legislates 80,000 lbs. as the legal GVW. The legal weight on single axle at Interstate highways and non-Interstate highways are 20,000 lbs. and 22,400 lbs., respectively. The legal weight on tandem axle is 34,000 lbs. [96]. In order to evaluate the overweight traffic effect on pavement performance, the WIM data was processed and grouped into two traffic groups. The first group included all the trucks within the legal weight limit (non-overweight traffic); while the second group included both the trucks within the legal weight limit and the overweight trucks (total traffic). The considered legal weight limits on single, tandem, and tridem axles were 22,400 lb., 34,000 lb., and 42,000 lb., respectively. Table 3.5 shows the highway type, route number, pavement structure, freezing index (FI), and the number of single, tandem, and tridem axles for the total and non-overweight traffic at the selected six sites. One site was selected for each highway type.

Table 3.5 Total and non-overweight (N-O) traffic at the selected routes

Pavement Type	Highway Type	Route #	Traffic	FI (degree-day)	Asphalt concrete (in.)	Cement concrete (in.)	No. of single axle	No. of tandem axle	No. of tridem axle
Flexible	State	NJ-138	Total	-9.3	2	0	412	118	7
		NJ-138	N-O	-9.3	2	0	410	109	1
	Interstate	I-195	Total	-9.3	12	0	3509	3602	201
		I-195	N-O	-9.3	12	0	3505	3562	76
	US	US-30	Total	-9.3	5	0	336	114	10
		US-30	N-O	-9.3	5	0	334	104	1
Composite/ Rigid	State	NJ-33	Total	-9.3	2.5	5.5	664	299	19
		NJ-33	N-O	-9.3	2.5	5.5	659	277	3
	Interstate	I-80	Total	-175.7	3	8	4197	4448	55
		I-80	N-O	-175.7	3	8	4051	3990	30
	US	US-202	Total	-175.7	3.5	7	356	225	25
		US-202	N-O	-175.7	3.5	7	355	211	3

Figure 3.4 shows the axle load spectra at the selected routes, respectively, for single, tandem, and tridem axles. It indicated that most of tridem axles were overweight axles, but it was less than 5% of the total traffic. The majority of overweight axle loads were on tridem and tandem axles, which were expected to have significant influences on pavement deterioration.

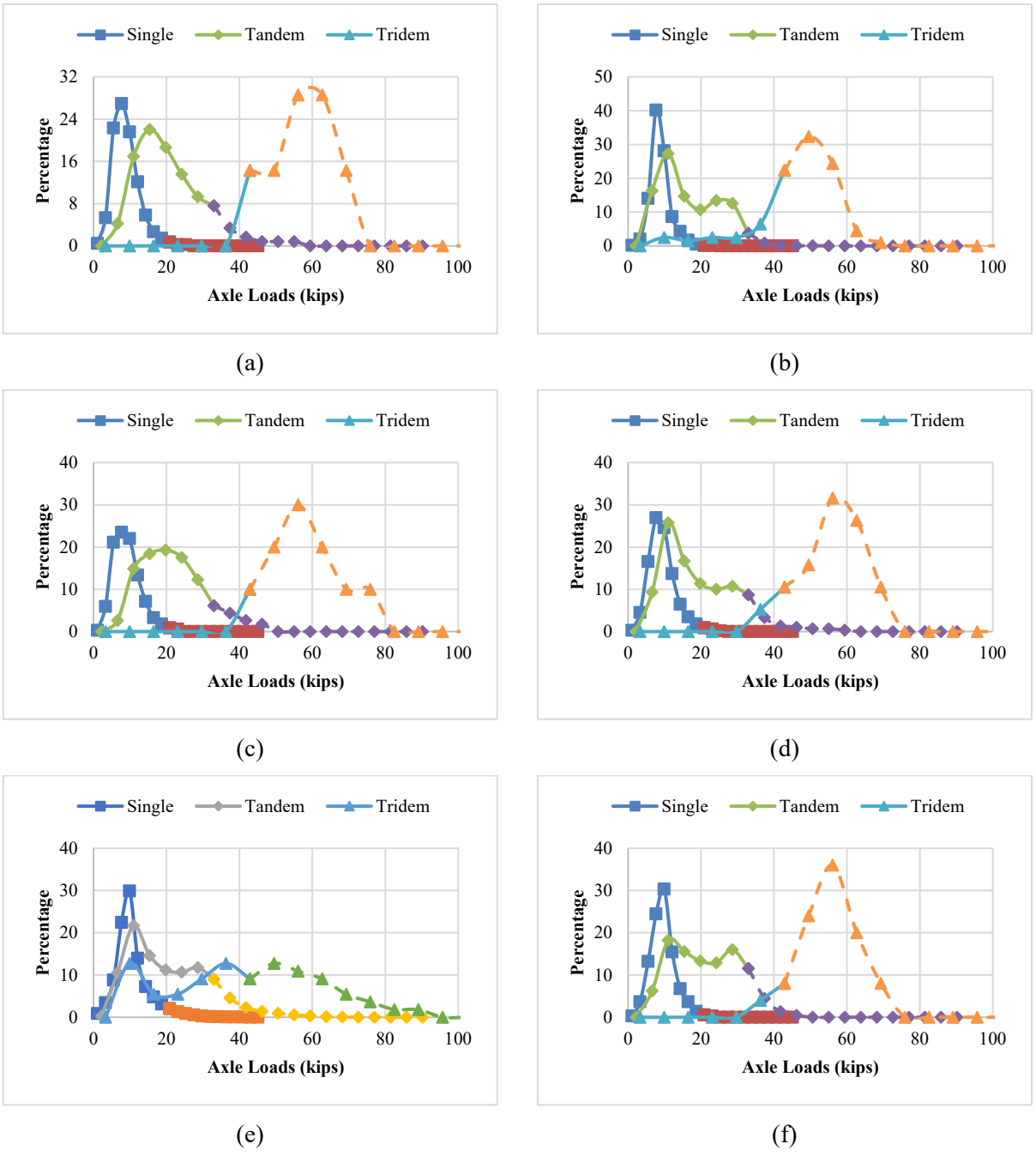

Figure 3.4 Axle load spectra at the selected sites: (a) NJ-138; (b) I-195; (c) US-30; (d) NJ-33; (e) I-80; (f) US-202 (solid line—: non-overweight; dotte dline---: overweight).

Figure 3.5 illustrates the deterioration trend of flexible and composite pavement under the total and non-overweight truck traffic using the derived SVR models based on the number of axles and the fitted Gaussian distribution of axle load spectra. The deterioration of pavement condition increased with the change of axle load spectra and the increasing number of axles, especially on tridem axle, due to the overweight truck traffic. Since the maintenance or rehabilitation was applied at the pavement sections before the SDI dropped to 2.4, it was difficult to track the pavement sections with the SDI below 2.5. In order to derive the entire curve of SDI deterioration, a sigmoidal model, which has been proven to provide acceptable accuracy to fit the performance curve, was applied to fit the predicted SDI values, as expressed by Eq. 23 [97], [98]. With the determined model parameters, the pavement life before the SDI decreasing to 2.4 was calculated for total and non-overweight traffic scenarios at each route.

$$SDI = SDI_0 - exp\,(a - b * c^{ln\,(\frac{1}{Age})}) \tag{23}$$

where, *SDI* is surface distress index; SDI_0 is surface distress index at year zero; *Age* is the year since the construction of rehabilitation; and *a, b,* and *c* are model coefficients.

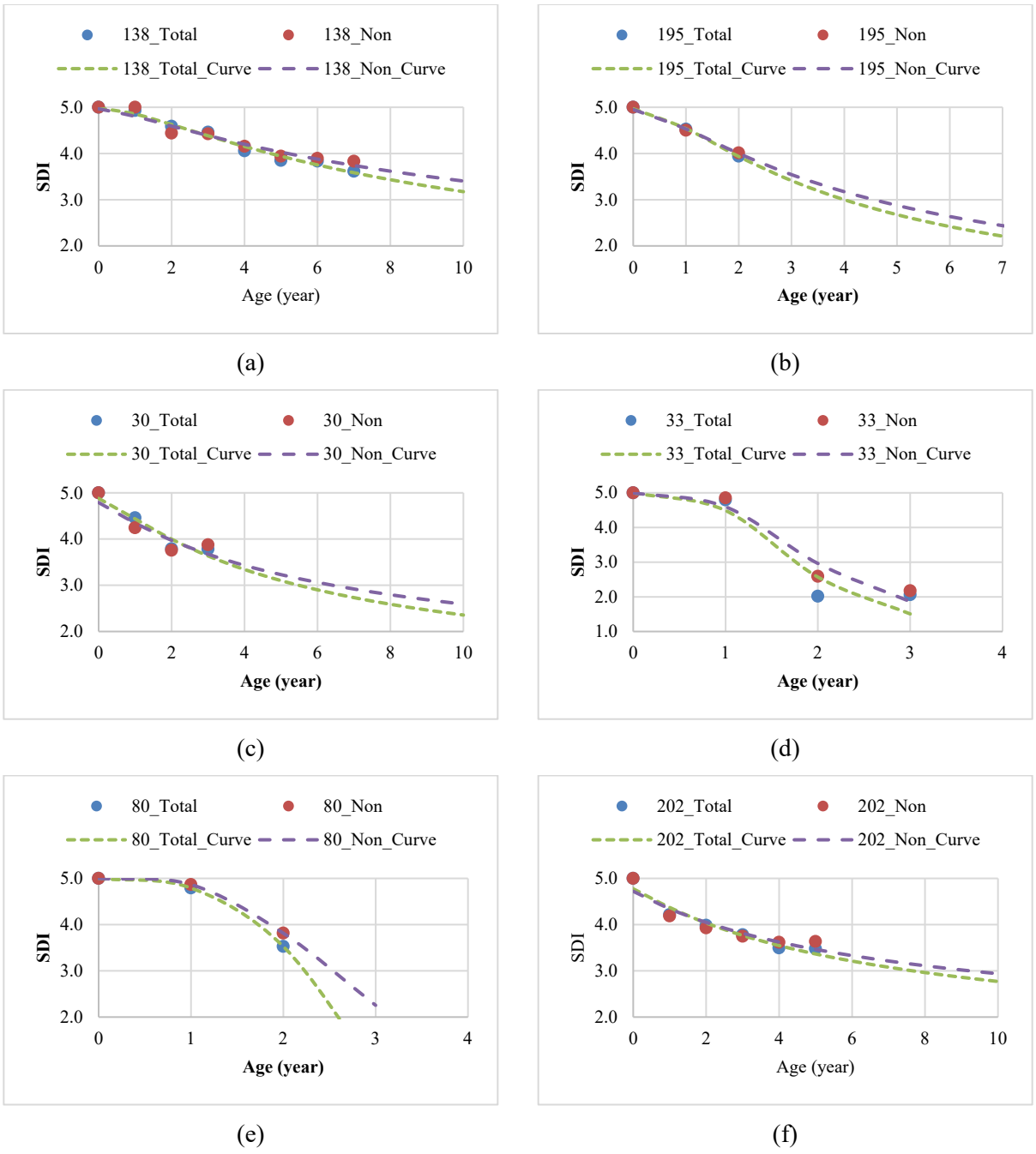

Figure 3.5 Pavement performance under total and nonverweight truck traffic for flexible pavements (a) state highway; (b) Interstate highway; (c) US highway; and composite pavements (d) state higway; (e) Interstate highway; (f) US highway.

To quantify the impact of overweight traffic on pavement damage, the reduction ratio of pavement life was calcualted using Eq. 24. Table 3.6 summarizes the overweight percenetage on single, tandem, and tridem axles and reduction ratio of pavement life for the selected routes. Since the SVR models were developed for each highway type, the pavemetn life reduction due to traffic loading variations were acurately captured for different pavement structures and highway types.

$$Reduction\ ratio\ of\ pavement\ life = \frac{L_T - L_N}{L_N} \tag{24}$$

where, L_T is pavement life caused by total traffic; and L_N is pavement life caused by the non-overweight traffic.

Table 3.6 Percentage of overweight axles and pavement life ratio for selected routes

Pavement Type	Route	Single	Tandem	Tridem	Pavement Life Reduction (%)
Flexible	NJ-138	0%	8%	86%	29%
	I-195	0%	1%	62%	14%
	US-30	1%	9%	90%	21%
Rigid	NJ-33	1%	7%	84%	9%
	I-80	3%	10%	45%	11%
	US-202	0%	6%	88%	23%

To quantity the pavement deterioration induced by overweight traffic on different road types, the reduction ratio of SDI was calculated using Eq. 25. Figure 3.6 illustrates the range of reduction ratio of SDI at the end of observation for different road types. It indicated that composite/rigid pavement sections were more affected by overweight traffic, especially for Interstate highways and US highways.

$$Reduction\ ratio\ of\ SDI = -\frac{SDI_T - SDI_N}{SDI_N} \tag{25}$$

where, SDI_T is SDI caused by total traffic; and SDI_N is SDI caused by the non-overweight traffic.

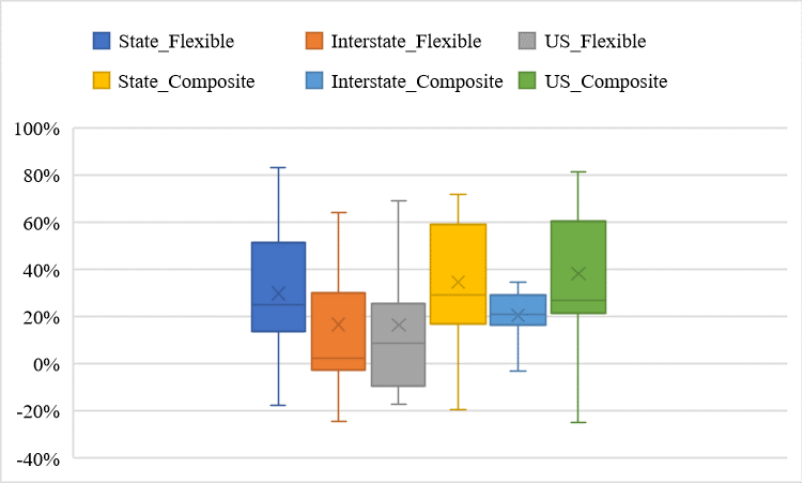

Figure 3.6 Boxplot of reduction ratio of SDI for different road types

3.4 Summary of Using Support Vector Regression to Model Traffic Load Impacts on Pavement

This chapter used traditional nonlinear regression and machine learning methods to derive pavement performance models under the impact of traffic loading. Compared to the nonlinear regression model, the accuracy of pavement performance prediction was significantly increased by utilizing the SVR method. The model accuracy was further improved by considering the number of axles and fitted Gaussian distribution of axle load spectra in the performance model. The derived SVR models were used to investigate the impact of overweight truck traffic on the deterioration trend of pavement. The deterioration of pavement condition increased with the change of axle load spectra and the increasing number of axles due to overweight truck traffic. The proposed pavement performance model can be further used in determining pavement damage caused by overweight trucks for pavement rehabilitation strategy and permit fee analysis. SVR model has proved to be an efficient approach to analyze small dataset of pavement performance. However, other supervised learning approaches, such as random forests and neural network, will be more suitable than SVR method to develop pavement performance models using a larger dataset due to the intensive computation of SVR.

4. RANDOM SURVIVAL FOREST MODELING TRAFFIC IMPACT ON PAVEMENT PERFORMANCE

The objective of this chapter is to quantify the impact of overweight traffic on asphalt pavement life using machine learning based survival analysis. Traffic data and field distress measurements were collected from the LTPP database. The random survival forest method was used to establish predictive models of load-related pavement distresses considering traffic loading, pavement structure, and climate. The variable importance approach was used to select the appropriate variables in the prediction model and to reduce prediction errors. The derived models were applied to estimate survival probability of asphalt pavement life at different traffic loading scenarios and to evaluate the impact of overweight traffic on pavement life.

4.1 Random Survival Forest Model

4.1.1 Algorithm of Random Survival Forest

Recently, random survival forest, a fully non-parametric approach, has been applied for better variable selection and survival analysis [99]. Non-parametric survival analysis, like Kaplan-Meier estimate, is flexible but cannot incorporate with covariates, which means it is difficult to infer the impacts of variables in the survival functions. Unlike traditional semi-parametric and parametric survival analysis (like Cox Proportional hazards regression analysis), an assumption of the distribution of life or a linear-exponential form was not needed in random survival forest model. Random survival forest is capable of dealing with a large number of variables and identifying non-linear effects of all variables automatically with the random forest for regression and classification, because decision trees are used as base learners or a block for an ensemble process in random survival forest [100].

Figure 4.1 illustrates the framework of random survival forest algorithm. The specific details of the random survival forest algorithm are as follows:

1. Draw bootstrap samples from the training dataset. Each bootstrap sample excludes approximately one third of the data, called out-of-bag (OOB) data.
2. Grow a survival tree for every bootstrap sample. Randomly select p candidate variables at every node of the survival tree. The candidate variable which maximizes survival difference between daughter nodes is used to split the node.
3. Grow the survival tree to full size under the constraint that a terminal node is supposed to have no less than $d_0>0$ unique deaths.
4. Calculate a cumulative hazard function (CHF) for every survival tree and average to derive the ensemble CHF.
5. Calculate prediction error for the ensemble CHF using out-of-bag data.

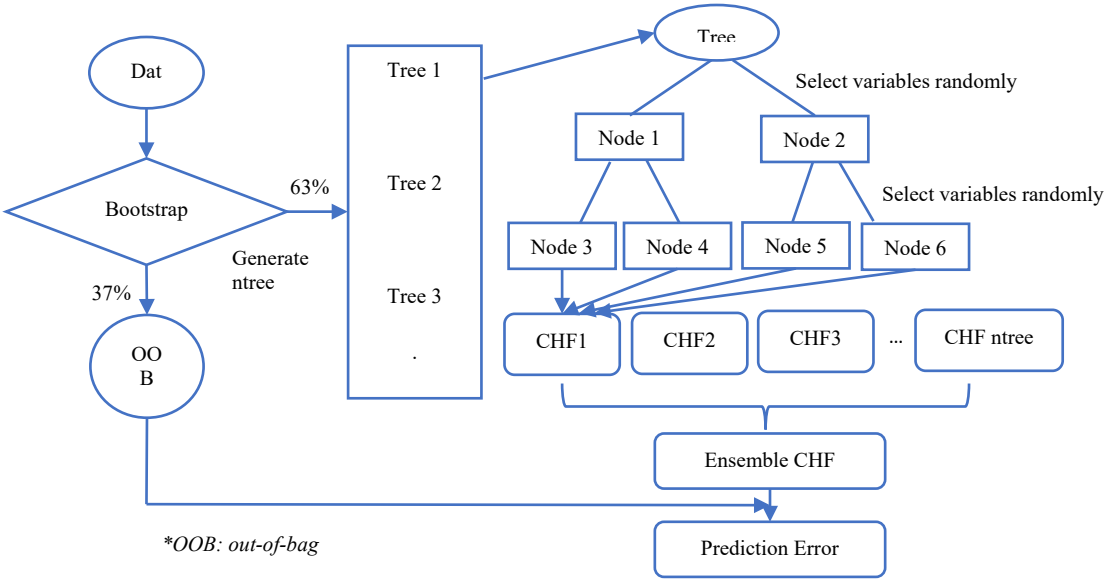

Figure 4.1 Framework of random survival forest algorithm

4.1.2 Ensemble of Cumulative Hazard Function

The key aspect of the random survival forest algorithm is to grow a survival tree and construct the ensemble CHF. Survival trees consist of binary trees grown by recursively splitting nodes. A survival tree is grown from the root node, and the root node is split into two daughter nodes according to a predetermined survival criterion. Then, every daughter node is split, and this process is repeated in a recursive order for every subsequent node. The node splitting is optimized by searching all possible split values and variables and selecting the optimal split that maximizes survival differences. Finally, a saturation point is reached when no new daughters can be generated because of the constraint that every node needs to contain a minimum of $d_0>0$ unique deaths. The most extreme nodes in a saturated survival tree are named terminal nodes denoted by *T*.

Let $(T_{1,h}, \delta_{1,h})\ldots, (T_{n(h),h}, \delta_{n(h),h})$ be the survival times and censoring information for cases in a terminal node $h \in T$. A case *i* is set to be right-censored at time $T_{i,h}$ if, $\delta_{i,h} = 0$; otherwise, if $\delta_{i,h} = 1$, the case is considered to have died or experienced an event at $T_{i,h}$. Let $t_{1,h} < t_{2,h} < \cdots < t_{N(h),h}$ be the *N(h)* distinct event times. Define $d_{l,h}$ and $Y_{i,h}$ to be the number of events and cases at risk at time $t_{l,h}$. The CHF estimate for terminal node *h* is the Nelson-Aalen estimator that is a non-parameter estimator for incomplete and censored data, and all individuals in *h* have the same CHF, as shown in Eq. 26.

$$\hat{H}_h(t) = \sum_{t_{l,h} \le t} \frac{d_{l,h}}{Y_{l,h}} \tag{26}$$

Each individual *i* has a *d*-dimensional covariate x_i. Let $H(t|x_i)$ be the CHF for *i*. To decide the CHF, drop x_i down the survival tree. Because of the binary characteristic of a tree, x_i will fall into a unique terminal node $h \in T$. The CHF for *i* is the Nelson-Aalen estimator for the terminal node of x_i. Eq. 27 is applied to define the CHF for all cases and estimate CHF for the tree.

$$H(t|x_i) = \widehat{H}_h(t), \text{ if } x_i \in h \tag{27}$$

The CHF is obtained from a single tree, and the CHF are averaged over *B* survival trees to derive an ensemble CHF. As is known, every survival tree in the forest is grown by an independent bootstrap sample. Define $I_{i,b} = 1$ if *i* is an OOB case for *b*; otherwise, set $I_{i,b} = 0$. Let $H_b^*(t|x)$ be the CHF for a tree grown using the b_{th} bootstrap sample. The ensemble CHF of OOB data for *i* is an average over bootstrap samples, as shown in Eq. 28.

$$H_e^{**}(t|x_i) = \frac{\sum_{b=1}^{B} I_{i,b} H_b^*(t|x_i)}{\sum_{b=1}^{B} I_{i,b}} \tag{28}$$

OOB data is dropped down a tree grown from bootstrap data and the terminal node and CHF of case *i* are tracked. The OOB ensemble CHF is estimated by Eq. 28. In contrast, the bootstrap ensemble CHF for *i* is computed using all survival trees, as shown in Eq. 29.

$$H_e^*(t|x_i) = \frac{1}{B} \sum_{b=1}^{B} H_b^*(t|x_i) \tag{29}$$

4.1.3 Prediction Error and Cross-Validation

Several measures are available for assessing the probabilistic risk predictions in survival analysis. Brier and logarithmic scoring rules are commonly selected metrics [101], [102]. In this study, the prediction error defined as the time-dependent expected Brier score is discussed and used to assess the developed model [103], as shown in Eq. 30.

$$BS\big(t, \hat{S}\big) = E\big(Y_i(t) - \hat{S}(t|X_i)\big)^2 \tag{30}$$

The expectation is in terms of the data of a case *i* which is not within the training dataset. $Y_i(t) = I\,(T_i \geq t)$ is the observed status of case *i* and $\hat{S}(t|X_i)$ is the predicted survival probability at time *t* for case *i* with predictor variables x_i. In survival analysis, the Kaplan-Meier estimate of survival is calculated with all training samples.

Several approaches are applied to deal with overfitting issues when only one data set is used to establish the prediction models. The bootstrap cross-validation method splits the data D_N into bootstrap samples D_b and corresponding test samples $D_N \backslash D_b$ ($b = 1 \ldots, B$). Bootstrap samples can either be generated with or without replacement from the original data. Then, models $\hat{S}_b$ are trained using the bootstrap training data D_b, corresponding test samples are predicted, and residuals are calculated. Eventually, the bootstrap cross-validation estimate of prediction error is computed by averaging over the test dataset, as shown in Equation 31.

$$BootCvErr\big(t, \hat{S}\big) = \frac{1}{B} \sum_{b=1}^{B} \frac{1}{M_b} \sum_{i \in \frac{D_N}{D_b}} \widehat{W}_i(t) \big\{\tilde{Y}_i(t) - \hat{S}_b(t|X_i)\big\}^2 \tag{31}$$

where, $\widehat{W}_i$ is the inverse probability of censoring weights. M_b is the size of bootstrap samples for resampling without replacement.

4.2 Model Results and Analysis

The random survival forest approach was applied to investigate asphalt pavement life using the failure threshold of each pavement distress. After combining the pavement distress data and all explanatory variables summarized in Table 2.1 and Table 3.1, the total number of data observations for alligator cracking, longitudinal cracking at wheel-path, and rut depth were 1214, 1214, and 1139, respectively. Based on the current practice of mechanistic-empirical pavement design, the thresholds of alligator cracking, longitudinal cracking at wheel-path, and rut depth were defined be 20% of lane area, 189 m/km (1000 ft/mile), and 12.7 mm (0.5 inch), respectively [27].

Variable importance measures the change (increase or decrease) of prediction error for the forest ensemble when a variable is randomly "noised-up" [99]. The variable with larger variable importance indicates the prediction error that is significantly impacted when the variable is "noised-up". Positive variable importance shows variables have predictive power, and zero or negative variable importance means variables make no contribution to prediction accuracy. The variable importance was estimated by the differences between the prediction error calculated using Equation 6 and the recalculated prediction error using the noise-up data by random node assignment. Random node assignment is capable of effectively calculating variable importance. In random node assignment, cases are randomly assigned to a daughter node when the parent node is split at the target variable.

Pavement structure and material, traffic history, climatic condition, and construction quality were considered to be influential variables for pavement performance and the variable importance was calculated for each variable. Figure 4.2 illustrates the variable importance for different pavement distresses. The greater value of positive variable importance indicates that the variable makes more contribution to the prediction model. The explanation of each symbol could be found in Table 2.1 and Table 2.2.

The results indicated that fatigue cracking was sensitive to climate, the number of tandem axle loads, the number of single axle loads, the thickness of AC overlay, and the thickness of milling. Longitudinal cracking was found to be more affected by the amplitude of tandem axle load spectrum (first peak), the number of tandem axles, the standard deviation of tandem axle load spectra (first peak), the number of single axle loads, and the amplitude of tandem axle load spectrum (second peak). The top-five important features for rut depth were the standard deviation of tandem axle load spectrum (second peak), the thickness of AC layer, the amplitude of tandem axle load spectra (second peak), and the number of single axle loads, and the thickness of treated base layer. These findings indicated that the explanatory variables of axle load spectra would impact pavement distress development. Therefore, the derived predictive models showed promise for analyzing the influence of traffic loading on deterioration trend of each pavement distress.

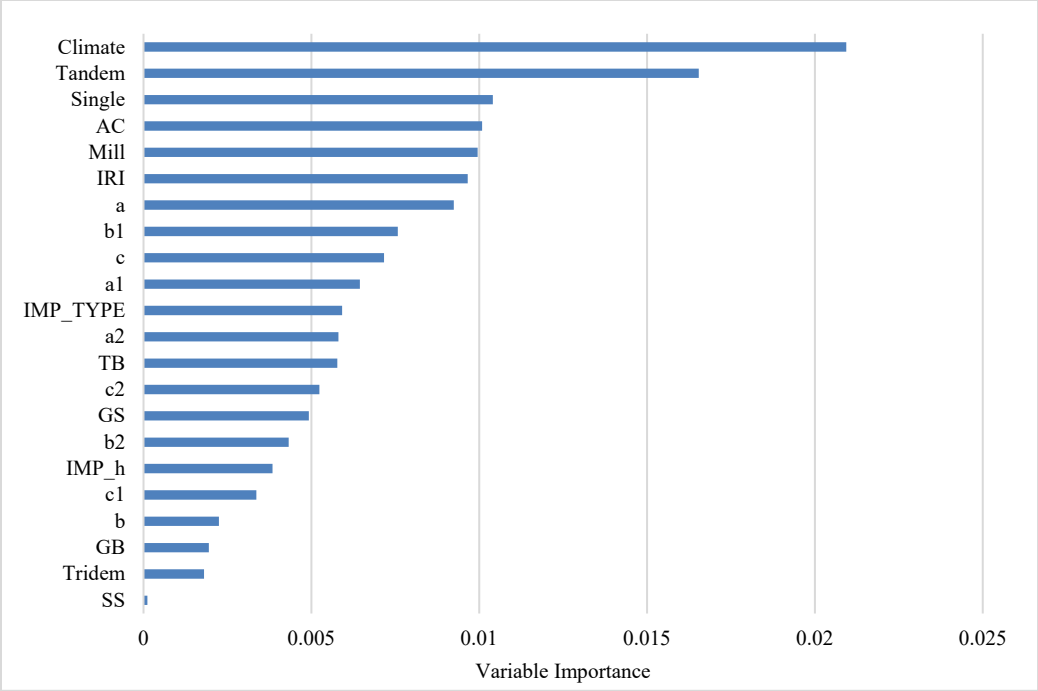
Climate
Tandem
Single
AC
Mill
IRI
a
b1
c
a1
IMP_TYPE
a2
TB
c2
GS
b2
IMP_h
c1
b
GB
Tridem
SS
0
0.005
0.01
0.015
0.02
0.025
Variable Importance

(a)

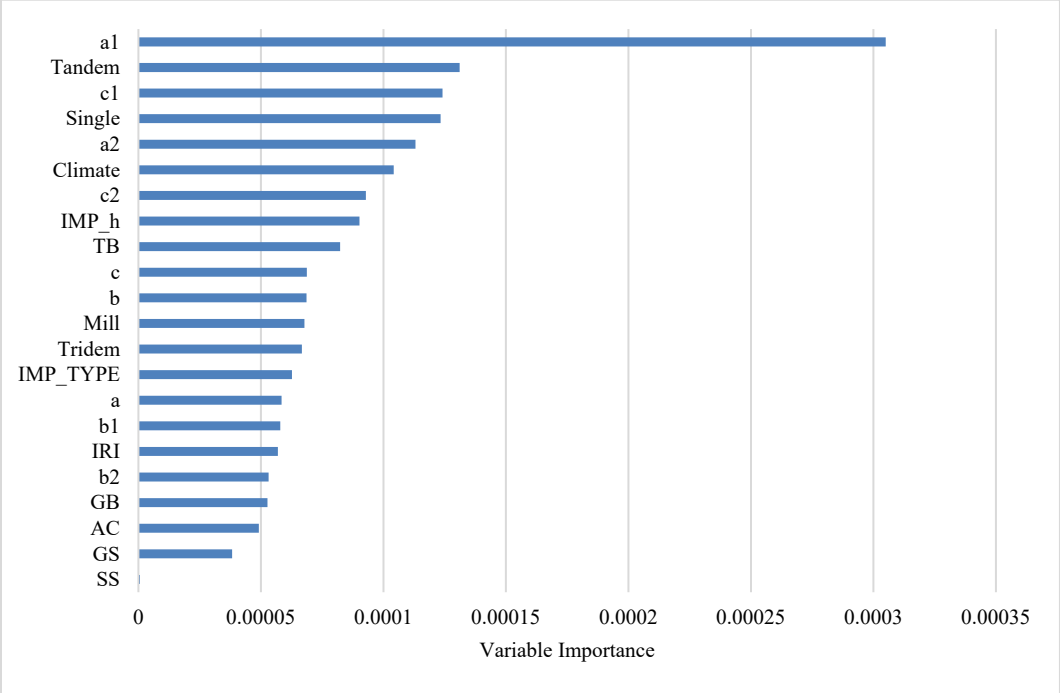
a1
Tandem
c1
Single
a2
Climate
c2
IMP_h
TB
c
b
Mill
Tridem
IMP_TYPE
a
b1
IRI
b2
GB
AC
GS
SS
0
0.00005
0.0001
0.00015
0.0002
0.00025
0.0003
0.00035
Variable Importance

(b)

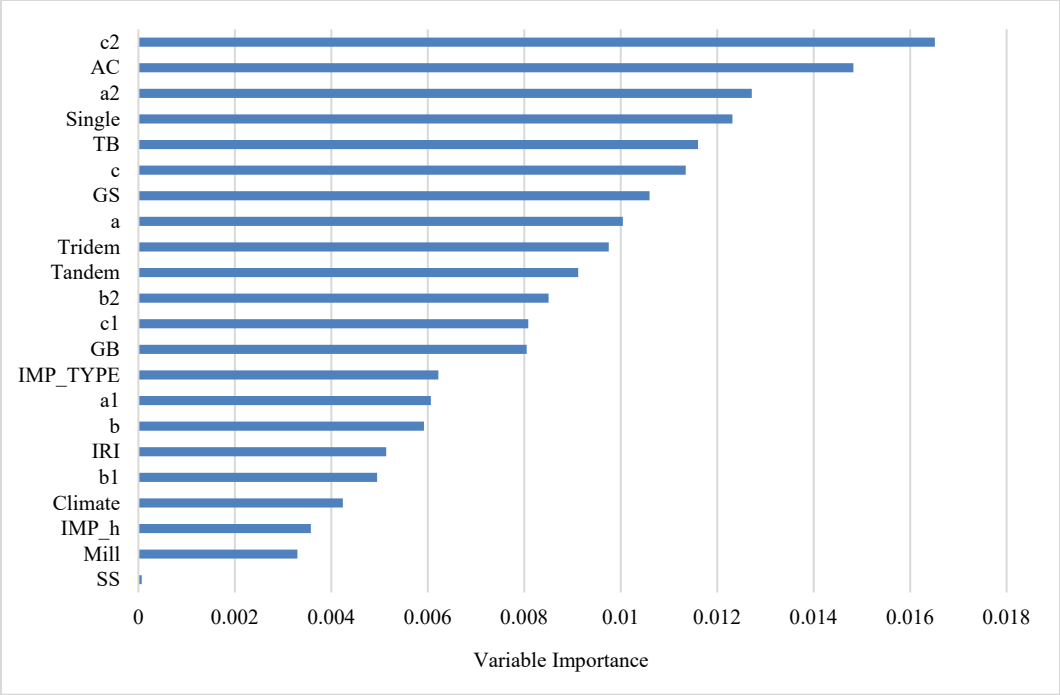

(c)

Figure 4.2 Variable Importance for (a) alligator cracking; (b) longitudinal cracking at wheel-path; and (c) rut depth

The cross-validation bootstrap method was used to compare the time-dependent Brier score (prediction error) of fitted survival forests. A total of 100 bootstrap samples were considered. Figure 4.3 shows the prediction error curve of random survival forest (RSF) models and the conventional non-parametric survival analysis using Kaplan-Meier (K-M) models for alligator cracking, longitudinal cracking at wheel-path, and rut depth, respectively. For alligator cracking and rutting, the prediction error of two models were found to be small and similar as the pavement life was shorter than eight years, but the random forest survival model showed much less error with the longer pavement life. As for longitudinal cracking, the prediction error of two models were similar but relatively smaller than those for other pavement distresses. In general, random survival forest models outperformed than the conventional survival analysis with K-M model in prediction accuracy.

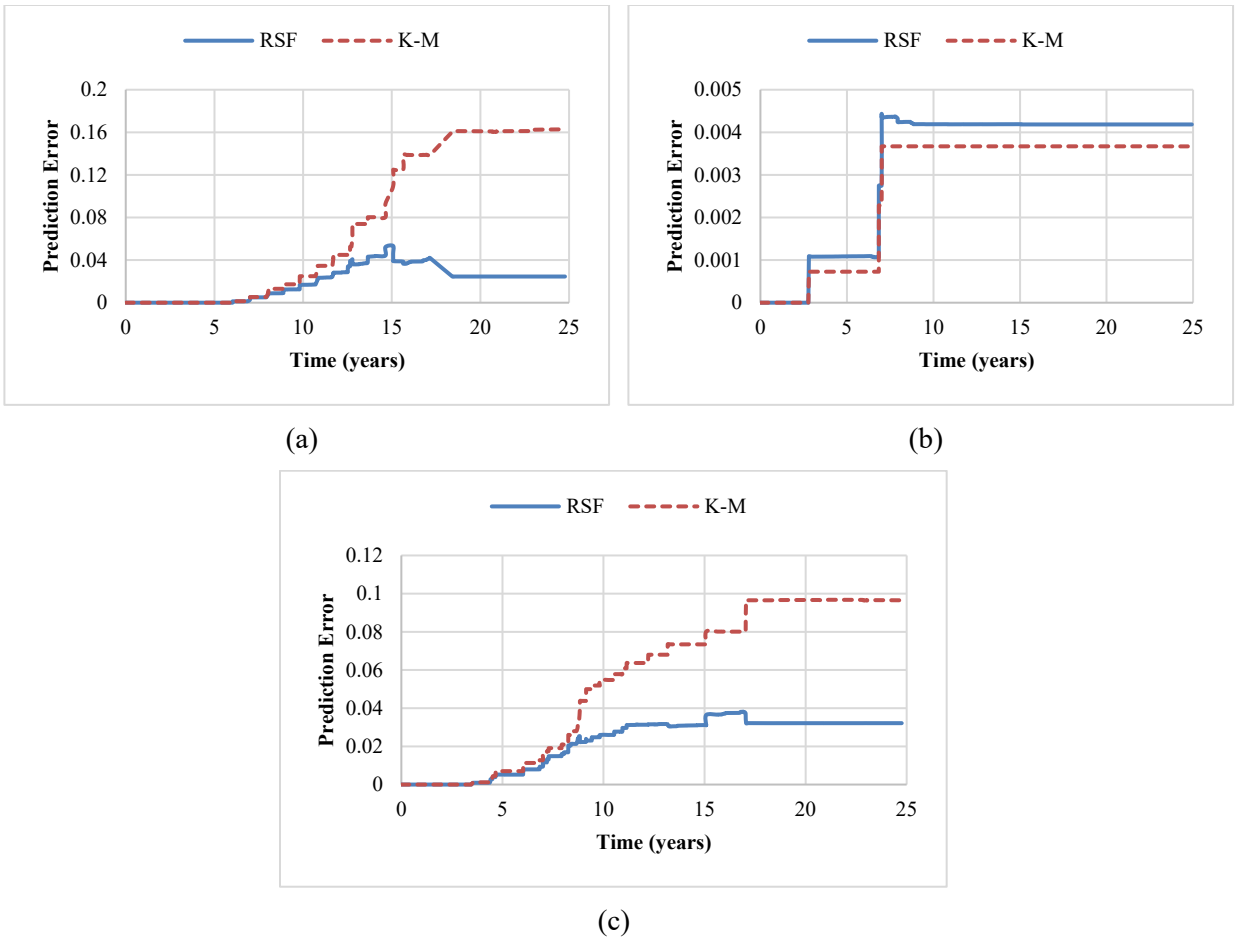

Figure 4.3 Prediction error of survival models: (a) alligator cracking; (b) longitudinal cracking at wheel-path; and (c) rut depth (RSF: random survival forest model; K-M: Kaplan-Meier model)

4.3 Impact of Overweight Traffic on Pavement Life

4.3.1 Effect of Overweight Traffic on Survival Probability

The derived random survival forest models can be used to analyze the influence of overweight traffic loading on the survival probability of AC pavement. To evaluate the overweight effect on pavement distress, the axle load spectra data was processed and divided into two traffic categories. The first category (non-overweight traffic) only included the trucks within the legal weight limit by excluding the overweight axles. The second category (total traffic) included the trucks within the legal weight limit and the overweight trucks. The differences of the number of axles and axle load spectra between the non-overweight and total traffic were considered in the survival analysis. The legal weight limits on single, tandem, and tridem axles were set as 22,400 lbs., 34,000 lbs., and 42,000 lbs. to distinguish the overweight axles from the total traffic [96].

One pavement section (SHRP_ID: 040502) was selected for the survivable probability analysis. The pavement structure consisted of a 6.5-inch AC layer and a 14.7-inch untreated base layer laid on soil subgrade, which was located in dry and no-freeze climate region. A maintenance treatment of milling the existing pavement (1.05 inch) and overlaying with AC (2.7 inch) was applied. The average daily number

of single, tandem, and tridem axles in the total traffic were 2769, 2775, and 8, respectively. The average daily number of single, tandem, and tridem axles in the non-overweight traffic were 2754, 2356, and 7, respectively. The overweight axles were found to be approximately 1%, 15%, and 13% of total single, tandem, and tridem axles, respectively. Figure 4.4 shows the axle load spectra of non-overweight and total traffic at the selected pavement section. The amplitude, mean, and standard deviation of the Gaussian distribution defined in Equation 1 were utilized to characterize the single and tandem axle load distribution pattern of non-overweight traffic and total traffic, respectively. The comparison of Figure 4.4 (a) and (b) shows that the tandem axle load spectra were significantly influenced by the overweight traffic.

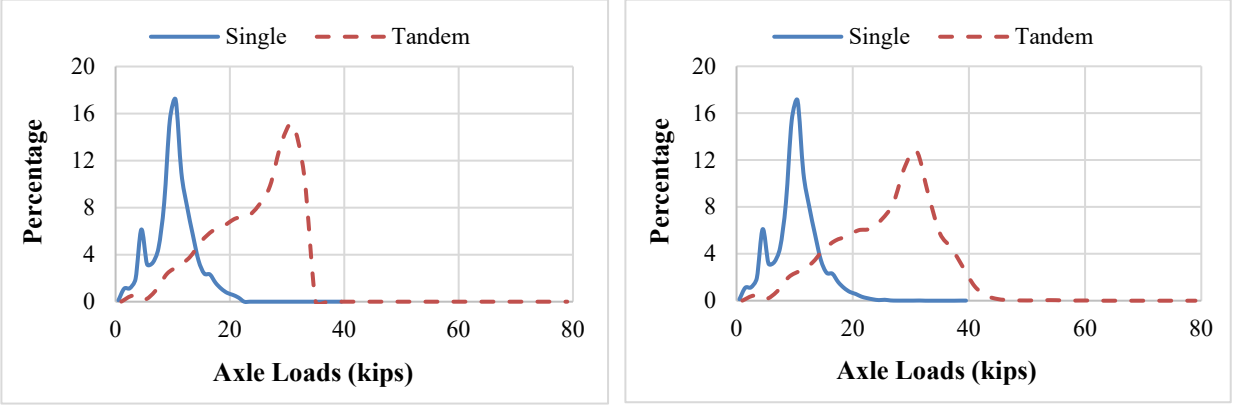

(a) (b)

Figure 4.4 Axle load spectra: (a) non-overweight traffic; (b) total traffic at the selected pavement section

The deterioration trends of pavement distress under total traffic and non-overweight traffic scenarios were predicted for the selected pavement section. Figure 4.5 presents the survival curves of pavement life at the selected pavement section respectively, for alligator cracking, longitudinal cracking at wheel-path, and rut depth. Survival curves illustrate the probability of pavement life after construction until the pavement distress reached the failure threshold. The decreasing trend of the survival curve is expected because pavement sections are likely to fail as service life increases. As expected, overweight truck traffic accelerated pavement deterioration and increased failure risk of pavement. It was found that the pavement life at 50% survival probability was reduced by 1-2 years due to overweight traffic. The reduction of pavement life varied depending on the failure mechanism.

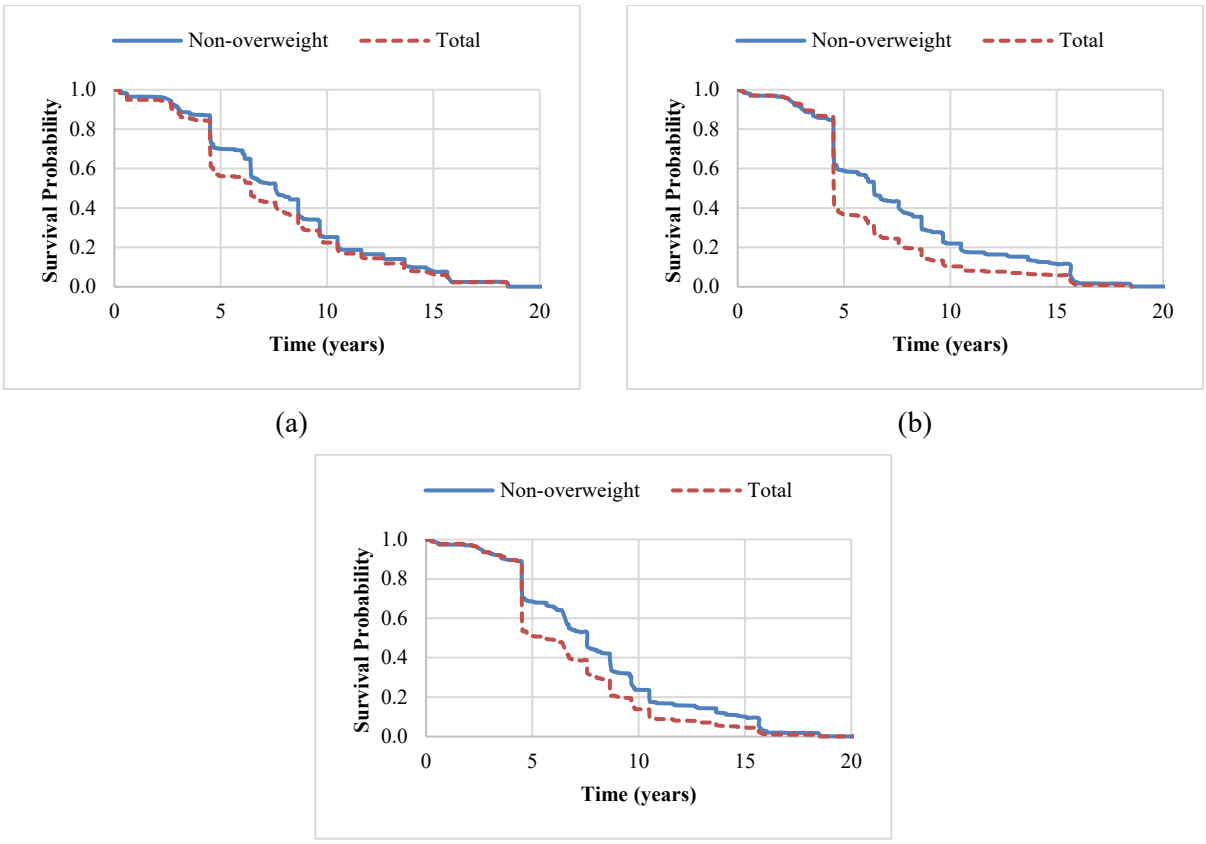

Figure 4.5 Survival probability curves at the selected pavement section: (a) alligator cracking; (b) longitudinal cracking at wheel-path; (c) rut depth at the selected pavement section

4.3.2 Effect of Overweight Traffic on Pavement Life Reduction

The derived predictive model was further used to evaluate the impact of overweight traffic on pavement life for all the selected 128 pavement sections. The survival probability of 50% was used to estimate the median survival life of a pavement section from the survival probability curve of each load-related pavement distress. Figure 4.6 (a)-(c) illustrate the percentage distributions of pavement service life before failure under total and non-overweight traffic. It was clear that the overweight traffic caused more pavement sections to fail after a shorter service life. The reduction ratio of pavement life resulting from overweight traffic was calculated for each pavement section, as shown in Eq. 32.

$$Reduction\ ratio = \frac{L_t - L_n}{L_n} \tag{32}$$

where, L_t is pavement life caused by total traffic; and L_n is pavement life caused by the non-overweight traffic.

Figure 4.6 (d) shows the pavement life reduction ratio resulting from overweight traffic in box plots. Note that the negative values are considered as the outliers impacted by the accuracy of predictive models. For most pavement sections, the reduction ratios were found to be in the range of 16-43% for longitudinal cracking at wheel-path, 3%-42% for alligator cracking, and 0%-33% for rut depth. The median values of the life reduction ratios were found to be 32%, 24%, and 12% for longitudinal cracking, alligator cracking, and rut depth, respectively. This indicates the average pavement failure risk for alligator cracking and longitudinal cracking were more impacted by overweight traffic loading. The t-test was conducted to determine if there were statistically significant differences between the life reduction ratios determined based on different pavement distresses. The calculated p-value for each paired comparison was far smaller than 0.05, which indicated the impact of overweight traffic on alligator cracking, longitudinal racking, and rutting was significantly varied.

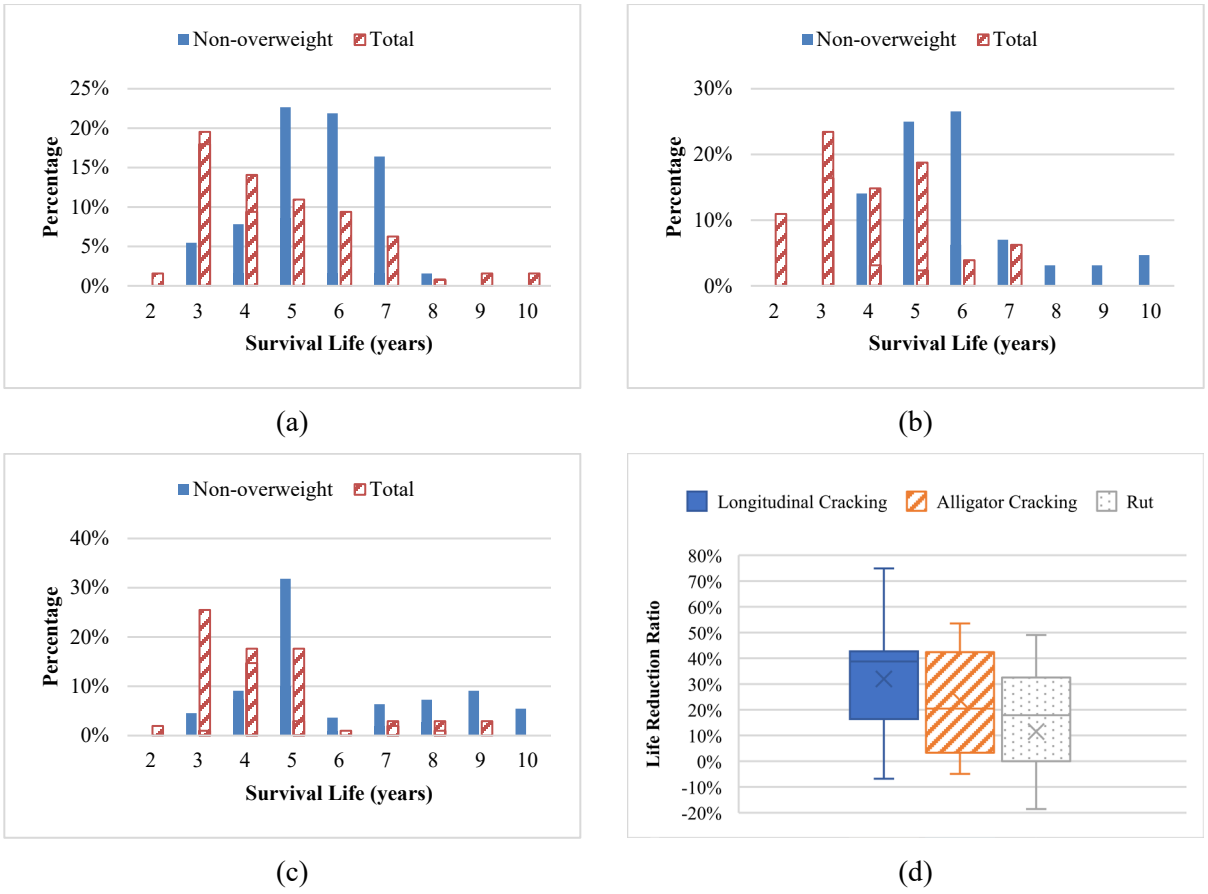

Figure 4.6 Distribution of survival life: (a) alligator cracking; (b) longitudinal cracking; (c) rut depth; and (d) Boxplots of survival life differences under total traffic and non-overweight traffic

These findings demonstrated the ability of random survival forest method for quantifying the impact of overweight traffic on pavement life considering axle load spectra. The survival probability curve of pavement service life at different traffic loading scenarios can be obtained directly. Thus, the random survival forest method provides an easier and faster manner of investigating the impact of overweight traffic on pavement life.

4.4 Summary of Predictive Modeling of Pavement Lifespan Under Overweight Traffic Using Machine Learning

This chapter used random survival forest method to investigate the impact of overweight traffic on asphalt pavement life using traffic data and field measurements from the LTPP database. The traffic data collected from WIM stations in the LTPP database were characterized through the number of axles and axle load spectra.

The random survival forest was proved to be an efficient approach to predict pavement life under the complex interaction of traffic loading, pavement structure, and climate. The variable importance method was used to select explanatory variables in the predictive models. The random survival forest models were developed for three different failure mechanisms (alligator cracking, longitudinal cracking, and rutting). The findings indicated that the explanatory variables regarding axle load spectra of traffic loading explained pavement performance degradation in significant roles. The random survival forest model can generate survival curves with better variable selection and survival prediction that shows less prediction error as compared to the conventional survival analysis.

The random survival forest models were further used to analyze the survival curves of pavement life at different traffic loading scenarios and evaluate the influence of overweight traffic. The reduction ratios of pavement life due to overweight traffic that was estimated based on different failure mechanisms were found having statistically significant differences. The results indicated that pavement failure due to alligator cracking and longitudinal cracking were more impacted by overweight traffic loading.

The study findings indicate the proposed random survival forest model is a promising approach for analyzing the impact of traffic loading on the failure risk of pavement. Due to the ability of random forest model for handling large amounts of variables, the model accuracy can be improved by considering more detailed climate conditions and material properties, such as precipitation, pavement temperature, air void, and asphalt binder type. The developed model can be used to quantify the impact of different influential factors on pavement performance and service life.

5. MECHANISTIC-EMPIRICAL ANALYSIS OF PAVEMENT PERFORMANCE UNDER VEHICULAR DYNAMIC LOADING

This section quantified the impact of dynamic traffic loading on pavement dis-tress of AC overlay on asphalt pavement. DLCs were calculated for each axle type and nonlinear regression models were fitted with respect to axle loads and pavement rough-ness levels. The dynamic loads excited by rough pavement surface condition were considered by transforming the static axle load spectra to the dynamic axle load spectra in MEPDG. Two representative pavement structures on major and minor highways were selected to investigate the impact of dynamic loads on pavement distresses using M-E pavement design. The impact of overweight traffic loading on pavement distresses was quantified by considering dynamic axle load spectra.

5.1 Consideration of Dynamic Loads in Axle Load Spectra

5.1.1 Pavement Profiles and Vehicle Models

Quarter-car models, two degree of freedom systems consisting of the wheel, suspension system, and a quarter of vehicle mass, have been widely adopted to simulate the vehicle behavior and investigate the influence of pavement evenness on dynamic tire forces [29], [104], [105], [106]. Taking advantage of advanced software (such as MATLAB), multibody dynamic truck models were developed to simulate dynamic characters of vehicles considering comprehensive vehicle system components [30], [107]. TruckSim, a multi-body dynamic model with multiple freedoms, is capable of simulating dynamic behaviors of various truck configurations. Multiple bodies can be simulated on the basis of the database embedded for a truck, including steering system, suspension system, power train, sprung mass, and so on [40], [108]. Previous research has used TruckSim to simulate dynamic tire forces of moving vehicles with various truck configurations considering a wide range of vehicle speeds and pavement roughness levels [109], [110].

The dynamic tire forces of different axle configurations excited by pavement surface profiles at specific operational speeds were calculated using TruckSim software. Figure 5.1 illustrates the axle configuration of Class 5, Class 7, and Class 9 trucks used in the study. The dynamic tire forces under single, tandem, and tridem axles were evaluated using the selected representative truck configurations. The spring rates of the tires were computed according to the static load deflection measurements and applied in the previous study related to vehicle dynamics simulation [111]. For the steering axle (Axle 1), the single tire was equipped. The tire width was 275 mm with the spring rate of 932 N/mm. For the drive axles (Axle 2, 3, 4, and 5), dual tire assembly was equipped. The tire width was 275 mm with the spring rate of 829 N/mm.

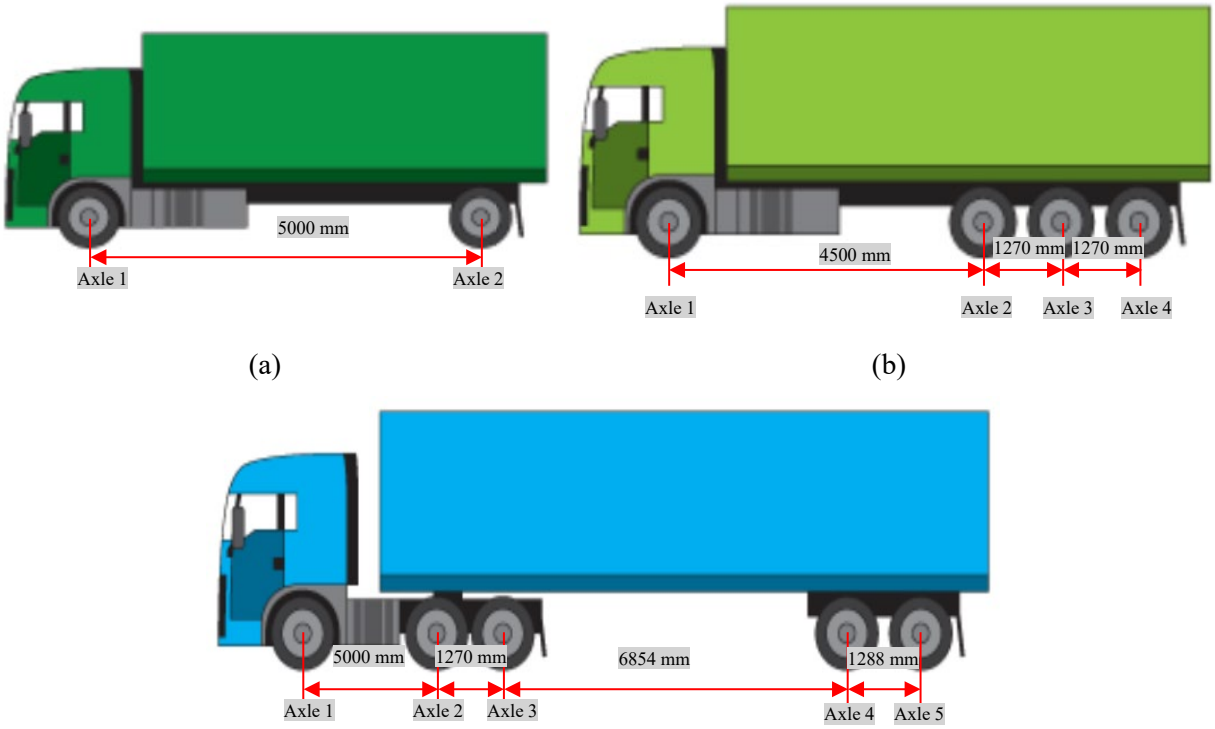

Figure 5.1 Illustration of axle configurations for (a) Class 5; (b) Class 7; and (c) Class 9 trucks (Texas DOT, 2013)

The Long-Term Pavement Performance (LTPP) was founded to collect pavement performance data by the Strategic Highway Research Program (SHRP). The LTPP program consisted of two fundamental categories of studies and some smaller studies to quantify specific pavement related details that have significant influence on pavement performance. The two categories of studies are the General Pavement Study (GPS) and the Specific Pavement Studies (SPS). The pavement profile data of selected pavement sections in New Jersey was extracted from LTPP database [80]. The moving average window of profile measurements was 0.3 m (0.98 ft), and the pavement surface elevation data was recorded at the interval of 0.15 m (0.49 ft). The total length of individual pavement segment was 152.4 m (500 ft) consisted of 1017 surveyed points. Totally 13 pavement profiles of five pavement sections (SHRP_ID = 341003, 341030, 341031, 341033, and 341034) on minor highways and 11 pavement profiles of five pavement sections (SHRP_ID = 340501, 340502, 340503, 340506, and 340560) on major (Interstate) highways were extracted. The measurements were conducted during 1997 - 2007 on the pavement sections of GPS-6S, GPS-2, and SPS-5 study. The range of IRI values of the selected major routes was 0.73-2.78 m/km (46-176 inch/mile). A wide range of IRI values from 0.73 m/km (46 inch/mile) to 4.73 m/km (300 inch/mile) was considered for minor routes. The pavement sections with similar IRI values might have totally different surface profiles, such as pavement sections of 340503, 340507, and 340560. In pavement management system, the IRI values of 1.50 m/km (95 inch/mile) and 2.68 m/km (170 inch/mile) were usually set as the thresholds of pavement conditions ranging fair to good and from poor to fair rating, respectively [112].

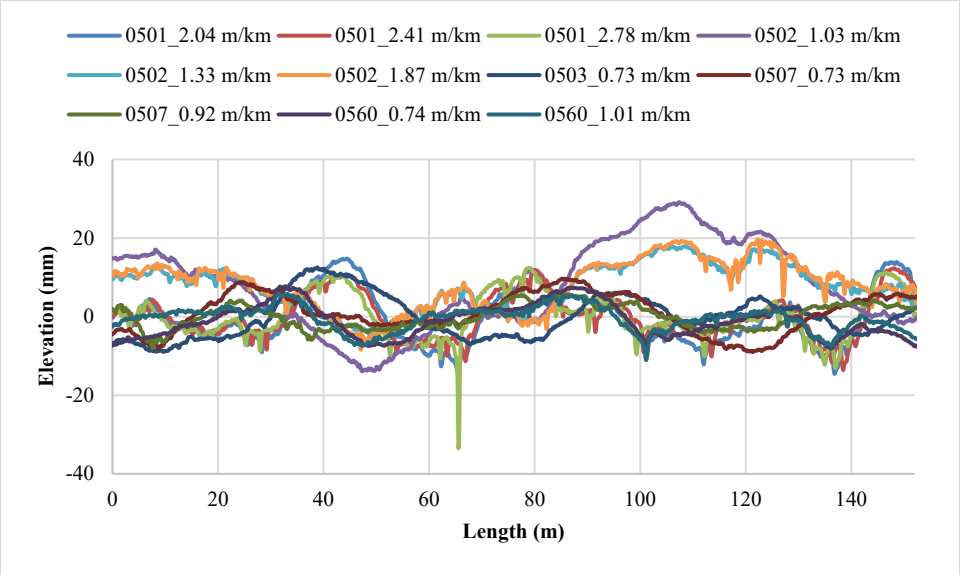

(a)

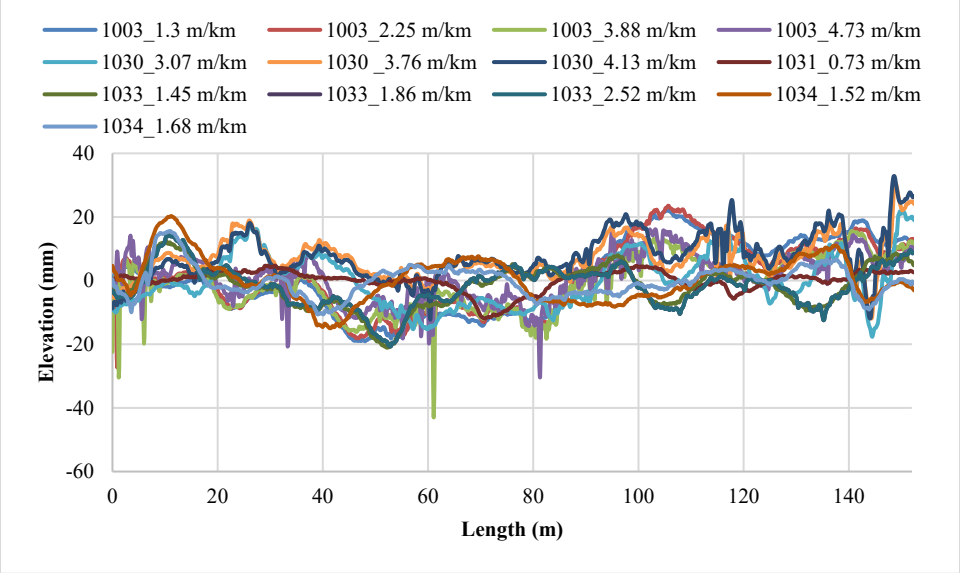

(b)

Figure 5.2 Selected pavement profiles: (a) major highways; (b) minor highways (legend: SHRP_ID_IRI value)

5.1.2 Dynamic Load Coefficients

To investigate the impacts of pavement surface conditions on dynamic loads, DLC was defined as a ratio by dividing the standard deviation of dynamic loads by the mean value [113]. It is well accepted that pavement roughness conditions and vehicle speed are influential factors to DLC. Hassan and McManus (2001) and Bilodeau et al. (2017)related DLC to pavement roughness conditions, while Bonabi (2011) developed regression models of IRI in terms of pavement roughness conditions and vehicle speeds. Few studies have considered the effect of static axle loads on DLC. Elisher et al. (2012) and Múčka (2017) predicted the DLC values in unladen and laden loading scenarios, respectively. Thus, in this study, DLCs of dynamic loads of single, tandem, and tridem axles estimated by the multi-body dynamic models in TruskSim were calculated for each pavement profile considering a wide range of static axle loads. The two vehicle speeds of 80 km/h (50 mph) and 104 km/h (65 mph) were set for minor and major highways, respectively. Figure 5.3 shows the effects of IRI and static axle loads on DLCs on minor and major highways. It indicated that DLC tends to increase as pavement roughness levels increase and decrease with the increasing of static axle loads.

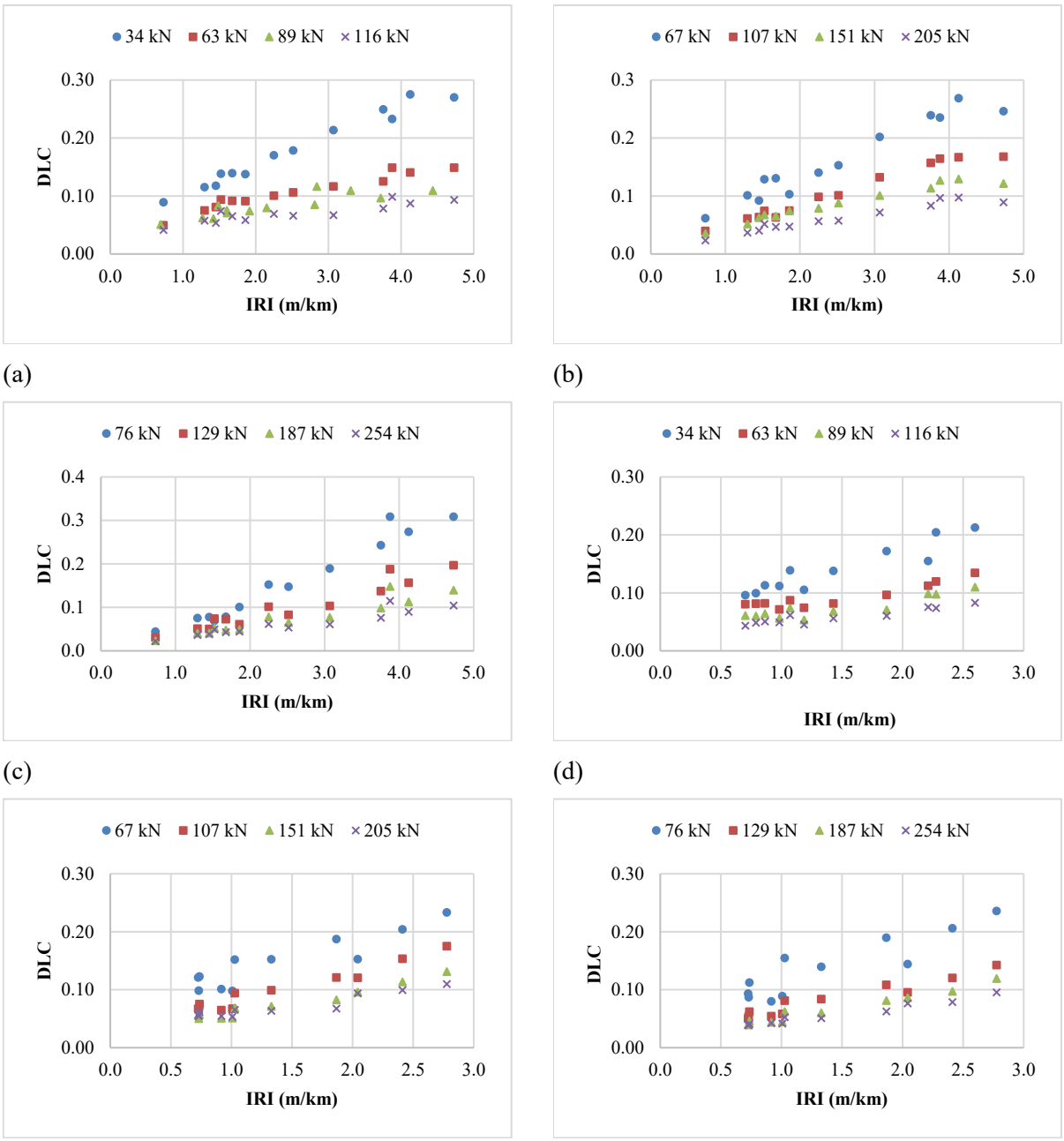

Figure 5.3 Change of DLC with IRI and axle loads: (a) single axle (minor); (b) tandem axle (minor); (c) tridem axle (minor); (c) single axle (major); (d) tandem axle (major); and (e) tridem axle (major)

Based on the calculated DLCs, a nonlinear regression model was fitted with respect to axle load and pavement roughness for each axle type, as expressed by Eq. 33. The vehicle speed was not included as a continuous variable in the regression model since two different speeds were considered for major and minor highways, respectively.

$$DLC_{i,k} = a \times ln(Q_k) + b \times IRI + c \tag{33}$$

Where, $DLC_{i,k}$is dynamic loading coefficient of axle type i (i = 1 for single, 2 for tandem, and for tridem); $Q_k$is static axle load (kips); *IRI* is international roughness index of pavement profile (m/km); and *a*, *b*, and *c* are fitting coefficients.

Table 5.1 presents the parameters of regression model in Eq.1 for the major and minor highways. Regression models were derived for single, tandem, and tridem axles loads with the acceptable R-squared values. Taking advantage of these models, the DLCs of specific static axle loads could be predicted for determination of dynamic axle load spectra given the axle load interval.

Table 5.1 Parameters of regression model of DLC with respect to IRI and axle load

Route Type	Axle Type	a	b	c	R-Squared value
Major highway (104 km/h)	Single	0.067	0.030	0.232	89
	Tandem	0.072	0.042	0.277	87
	Tridem	0.068	0.042	0.265	86
Minor highway (80 km/h)	Single	0.096	0.025	0.308	85
	Tandem	0.089	0.033	0.317	88
	Tridem	0.081	0.041	0.277	82

5.1.3 Dynamic Axle Load Spectra

Dynamic load distribution should consider the impact of deviation of axle loads from static magnitudes. The discrete distribution of axle loads is determined by the percentage of axle passes falling into a set of axle load intervals. The Dynamic Axle Loads Spectrum includes both static axle load spectra and distributions of dynamic loads coming from other axle load intervals [114]. The percentage of dynamic loads d_j in the interval *j* comes from dynamic loads induced by axles with static loads of Q_k. The dynamic axle load spectra, the total percentage d_j of all axle loads in a given load interval *j* is calculated as a sum of dynamic loads from all the static axle load spectra intervals *k*. The percentage of dynamic loads d_j is computed using Eq. 34.

$$d_{i,j} = \sum_{k=1}^{n} s_k \frac{1}{DLC_{i,k} Q_k \sqrt{2\pi}} exp\left(-\frac{(Q_k - Q_j)^2}{2DLC_{i,k}^2 Q_k^2}\right) \tag{34}$$

where, $d_{i,j}$are the percentage of dynamic loads; Q_j are dynamic loads (kips); and s_k are the percentage of number of axles with static load Q_k determined from WIM data.

It was assumed that dynamic loads can be characterized as normal distribution with the average value in the middle of a given interval and standard deviation, which has been proved and applied in previous works [32], [114]. The DLC values in the formula would change with the pavement roughness levels and axle load intervals designated by MEPDG. Figure 5.4 illustrates the comparison of static axle load spectra and dynamic axle load spectra on major and minor highways. The dynamic loads at three different IRI

values of 1 m/km (63 inch/mile), 2 m/km (126 in/mile) and 3 m/km (190 in/mile) were compared with the static loads on smooth pavement surface. The spikes in the distribution of axle loads were flattened after transformation because of the greater deviation of dynamic loads of vehicles. The increase of DLC led to a reduction in the percentage of lighter loads but increase in the percentage of heavier loads. The heavier axle loads were expected to accelerate pavement deterioration in M-E pavement design. The distinction of load distribution on tandem and tridem axles were more obvious, especially for the IRI value of 3 m/km.

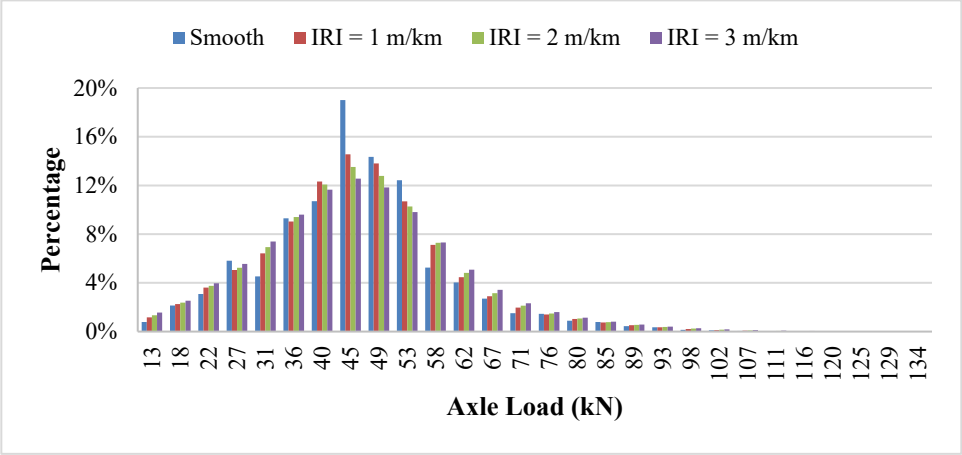

(a)

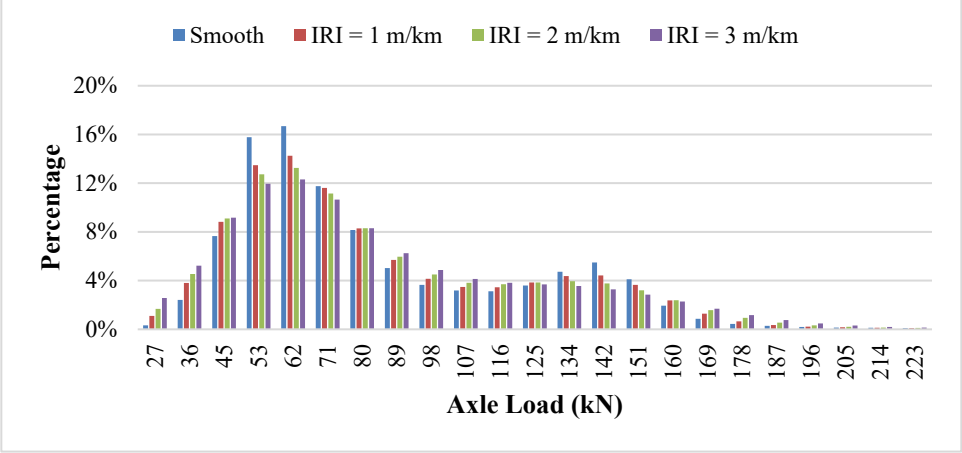

(b)

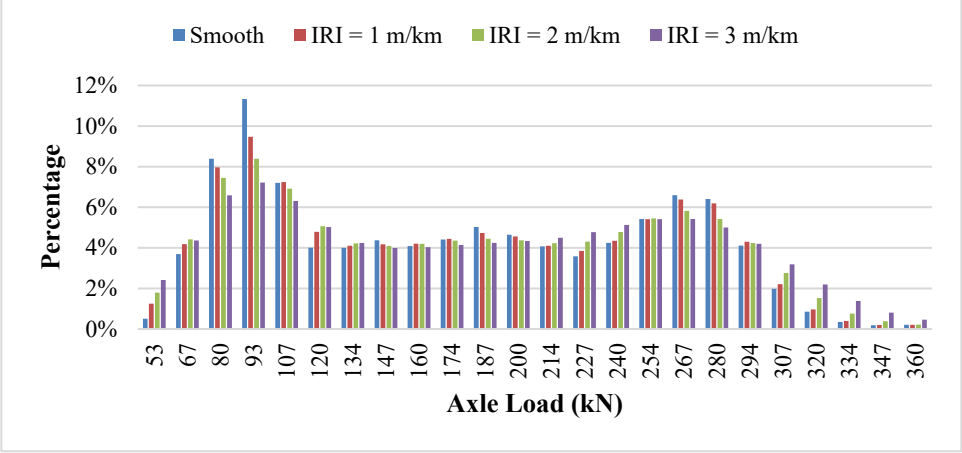

(c)

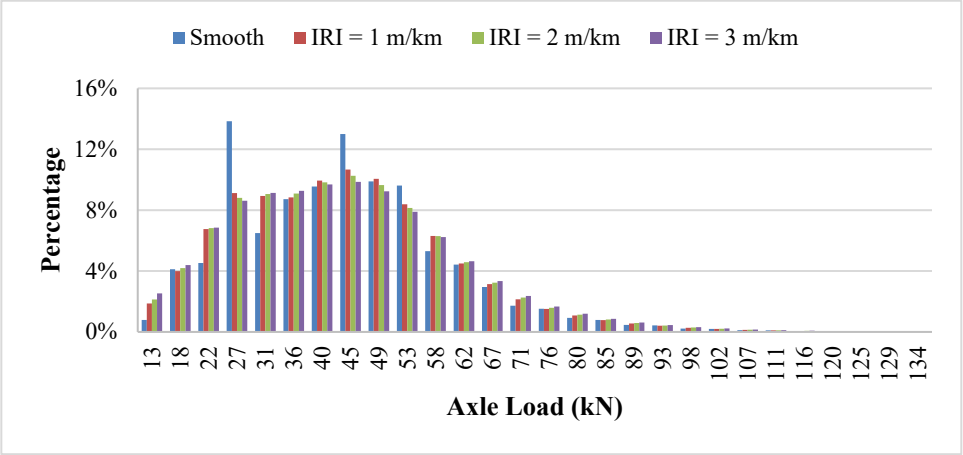

(d)

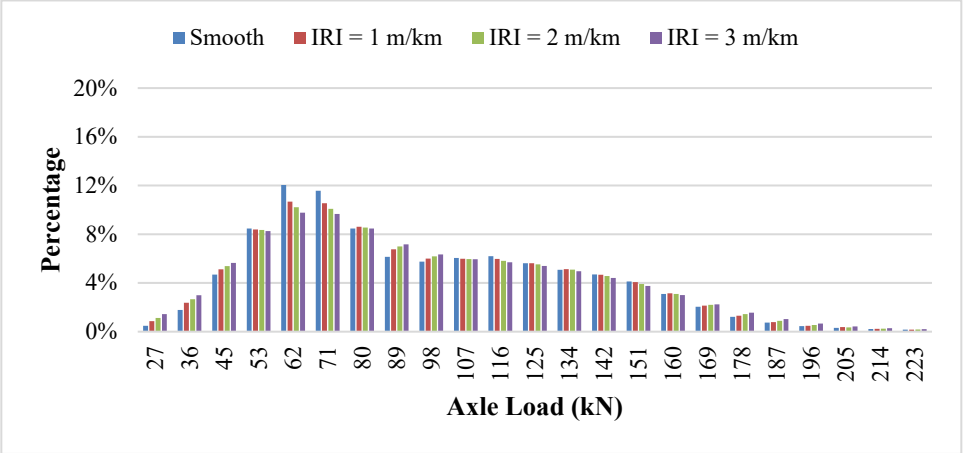

(e)

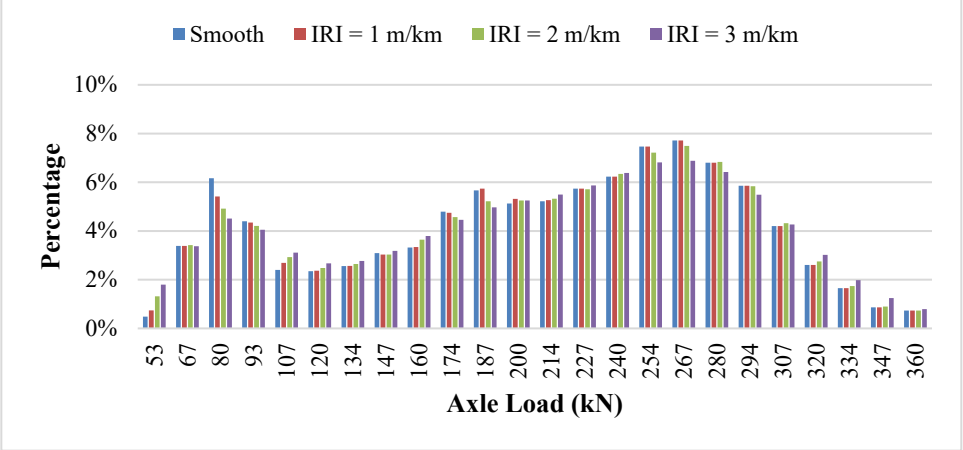

(f)

Figure 5.4 Static and dynamic axle load spectra: (a) single axle (major); (b) tandem axle (major); (c) tridem axle (major); (d) single axle (minor); (e) tandem axle (minor); and (f) tridem axle (minor)

5.2 Mechanistic-Empirical Pavement Analysis Considering Dynamic Axle Loads

5.2.1 Analysis Inputs and Assumptions

Asphalt overlay is commonly used for rehabilitating asphalt pavements with or without milling part of original surface layer. In this study, two AC overlays with different thicknesses of existing AC layers (254 mm and 152.4 mm) were designed as the representative pavement structures of major and minor highways in M-E pavement design. The thicknesses of new AC layers were 50.8 mm. Table 5.2 shows the inputs of material property, traffic, and climate. Figure 5.5 presents the dynamic modulus of asphalt mixture in overlay at different temperatures and loading frequencies, which was set as the Level 1 input in MEPDG. The material properties of mixture in AC overlay were obtained from producer, while the mixture's default material properties were designated for the existing AC layer. For both pavement structures, a 254-mm base layer and a 254-mm subbase layer were laid on the subgrade, and the typical material properties in NJ were designated for the base layer, subbase layer, and subgrade.

Table 5.2 Pavement structure and material inputs for Pavement ME

Input	Parameters		Major highway	Minor highway
Material Property	AC Overlay	Thickness (mm)	50.8	
		Air Void (%)	6.2	
		Total Binder Content (%)	5.4	
		Effective Binder Content by Volume (%)	10.5	
		Asphalt mixture	9.5M64 (level 3)	
	Existing AC Layer	Thickness (mm)	254	152.4
		Air Void (%)	5	
		Total Binder Content (%)	5	
		Effective Binder Content by Volume (%)	11.6	
		Asphalt mixture	9.5M64 (level 3)	
	Base	Thickness (mm)	254	
		Classification	A-1-a	
		Resilient Modulus (MPa)	552	
	Subbase	Thickness (mm)	254	
		Classification	A-1-b	
		Resilient Modulus (MPa)	414	
	Subgrade	Classification	A-1-a	
		Resilient Modulus (MPa)	731	
Traffic	Two-way annual average daily traffic (AADT)		2202	1575
	Operational speed (km/h)		104	80
Climate	Mean annual air temperature (°C)		11.7	
	Mean annual precipitation (mm)		1306	

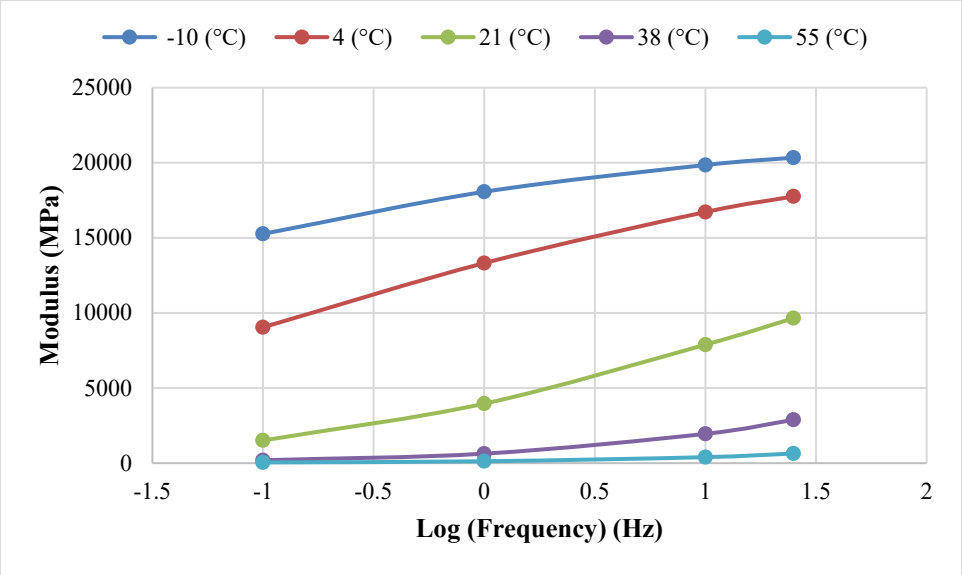

Figure 5.5 Dynamic modulus of asphalt mixture for overlay

The dynamic axle load spectra were modified using Eq. 34 based on the estimated DLC by Eq. 33 and static axle load spectra from WIM data in LTPP database. Vehicle class distribution and axles per truck were updated according to the modified axle load spectra. The default monthly adjustment factor was used. The two-way annual average daily traffic (AADT) of minor and major highways were 1575 and 2202, respectively. The operational speeds of minor and major highways were 80 km/h (50 mph) and 104 km/h (65 mph), respectively. The environmental data was required to perform an analysis in the MEPDG. The climate data at the station US NJ-144169 (latitude: 40.05; longitude: -74.4) in Jackson Township, NJ was applied for the pavement structures on major and minor highways using M-E pavement design. The default parameters in transfer functions were applied for M-E analysis to quantify the impact of dynamic loads on pavement performance.

5.2.2 Impact of Dynamic Loads on Pavement Performance

In general, the new asphalt overlay shows a similar cracking pattern which matches the fatigue cracking in the existing asphalt layer after opening to traffic. The cracking propagation from the existing AC layer into and through the new AC overlay is named as reflective cracking. The occurrence of reflective cracking tends to cause water infiltration, rapid deterioration of the underlying pavement structure, and reduction of pavement service life. Reflective cracking is the result of strain concentration in the AC overlay due to the movement induced by shearing or bending action from traffic loading and daily/seasonal temperature changes in the existing asphalt pavement at the vicinity of cracks. Thus, reflective cracking is one of the asphalt overlay failure criteria. Regarding AC overlay rutting, it is well accepted that rutting or permanent deformation is the combined result of densification due to volume change of asphalt mixture and repetitive shear deformation because of plastic flow without volume change. The rut depth in the AC layer is another failure criteria of AC overlay design. Rutting depth is impacted by many factors, such as binder content, binder type, mix type, temperature, load level, and initial density after compaction [115].

In M-E pavement design, reliability is a combined indicator of probability that each performance measure will be less than a specific level over the analysis period [27]. The reliability level of 90% was considered in the analysis. In the M-E analysis, the initial IRI values were assumed to be 1 m/km (63 inch/mile) for both types of highways, and the terminal IRI values at the 20th year of service period were found to be 2.25 m/km (142 inch/mile) and 2.32 m/km (146 inch/mile) for major and minor highways, respectively. When the initial IRI was 2 m/km (126 inch/mile), the terminal IRI values at the 20th year of service period were 3.97 m/km (250 inch/mile) and 4.03 m/km (254 inch/mile) for major and minor highways, respectively. Besides, the initial IRI was found to have no influence on the propagation of pavement distress, except for terminal IRI value. Therefore, the IRI values of 1m/km, 2 m/km, and 3 m/km, which included a reasonable range of IRI values during pavement service period, were applied to derive the dynamic axle load spectra to evaluate the effect of dynamic loads on pavement distresses. The M-E outputs indicated that dynamic loads increased IRI, rut depth (total and AC only), and fatigue cracking (reflective) during the pavement service period. The effect of dynamic loads on reflective fatigue cracking was relatively more significant.

Figure 5.6 illustrates the comparison of reflective fatigue cracking and rut depth under the static and dynamic loads in pavement structures on major highway. Reflective fatigue cracking of AC overlay pavement sections includes reflective cracking and bottom-up cracking in AC layer. The AC overlay shows a similar cracking pattern which matches the existing cracking. Reflective fatigue cracking increased rapidly after the 2-year service period and approached a specific value after a 10-year analysis period. The rut depth in the AC layer accumulated slowly over time. It indicated the impact of dynamic loads on reflective cracking varied during the cracking propagation. The influence became more significant from the 3rd to 7th years, while slight influence was observed at the end of cracking propagation. The impact of dynamic loads on rut depth was found to slightly increase with the accumulation of rut depth with pavement age, but the overall impact was not significant.

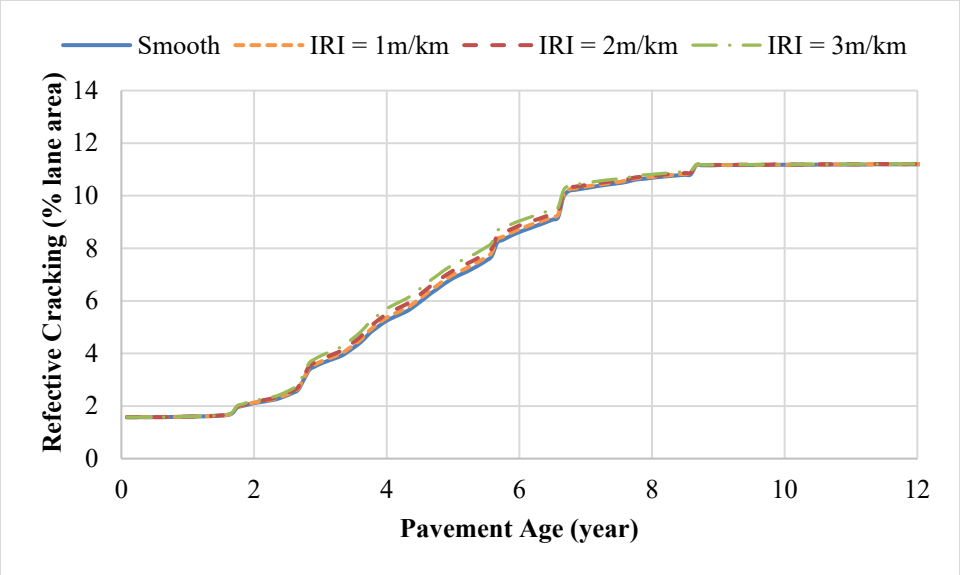

(a)

(b)

Figure 5.6 (a) Fatigue cracking (reflective); and (b) rut depth under the static and dynamic loads on pavement structure on major highway (10% existing cracking)

Figure 5.7 illustrates the reflective fatigue cracking and rut depth in pavement structure on minor highway under the static and dynamic loads. The reflective fatigue cracking propagated rapidly after the 2.5-year service period and approached to a constant value after 15-year analysis period. Compared to the trend of reflective fatigue cracking, the impact of dynamic loads on rut depth was relatively small. The impact of dynamic loads on reflective cracking and rut depth varied depending on pavement age, and the influence was not so significant as compared to the influence on major highways. To quantify the susceptibility of pavement distress to dynamic loads, the increasing ratio due to dynamic loads was defined by Eq. 35.

$$R_{s-d} = \frac{D_s - D_d}{D_s} \tag{35}$$

where, R_{s-d} is the increasing/decreasing ratio due to dynamic loads; D_s is pavement distress estimated using static axle load spectra; and D_d is pavement distress estimated using dynamic axle load spectra.

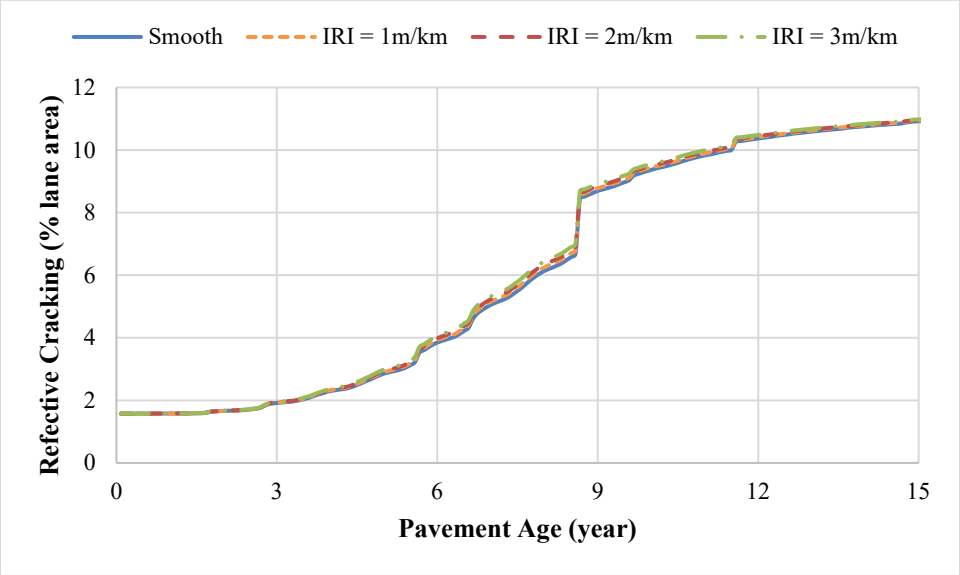

(a)

(b)

Figure 5.7 (a) Fatigue cracking (reflective); and (b) rut depth under the static and dynamic loads on pavement structure on minor highway (10% existing cracking)

The fatigue cracking in the existing AC layer was a potential influential factor for cracking propagation. The cracking percentage in existing layers were set as 5%, 10%, and 15%, which covered a full-scale range observed in field inspection. Table 5.3 shows the increasing ratio of reflective fatigue cracking considering different levels of existing fatigue cracking in AC layer. As expected, the cracking percentage increased with pavement roughness levels increased. Existing cracking raised the increasing ratio of reflective fatigue cracking. The ratio of reflective fatigue cracking increased then

decreased over time. For major highways with the existing fatigue cracking of 10%, the dynamic axle loads increased the reflective fatigue cracking by 2.1% after a 3-year service period when the IRI of pavement profile was 1 m/km. The reflective fatigue cracking was increased by 4.5% if the IRI was 2 m/km, and the reflective fatigue cracking was increased by 8.2% when the IRI was 3 m/km.

For minor highways with the existing fatigue cracking of 10%, the increasing ratios of reflective fatigue cracking were 2%, 3.6% and 5.4% after a 7-year service period for the IRI values of 1 m/km, 2 m/km, and 3 m/km, respectively. Therefore, the influence of dynamic axle loads on the pavement structure of major highways was more significant than that of minor highways. The impact of dynamic loads on reflective fatigue cracking was distinguished at early stage of service period and eliminated after 10-year analysis period when the propagation of reflective cracking reached to a specific level. The impact of dynamic loads became much less significant after the pavement was fully deteriorated, which was primarily determined by the existing cracking for overlay design. The selection of distress threshold and analysis period would dominate the increasing ratio.

Table 5.3 Effect of existing cracking on increasing ratio of reflective fatigue cracking due to dynamic loads

Type	Existing Cracking %	IRI	3-Year	5-Year	7-Year	10-Year	15-Year	20-Year
Major	5%	1 m/km	1.4%	1.6%	0.5%	0.0%	0.1%	0.1%
		2 m/km	3.2%	3.4%	1.0%	0.1%	0.1%	0.2%
		3 m/km	5.7%	6.1%	1.6%	0.1%	0.2%	0.3%
	10%	1 m/km	2.1%	2.0%	0.6%	0.0%	0.0%	0.1%
		2 m/km	4.5%	4.2%	1.1%	0.1%	0.1%	0.2%
		3 m/km	8.2%	7.5%	1.9%	0.1%	0.2%	0.3%
	15%	1 m/km	2.4%	2.1%	0.5%	0.1%	0.1%	0.1%
		2 m/km	5.3%	4.5%	1.1%	0.1%	0.1%	0.1%
		3 m/km	9.6%	8.1%	1.9%	0.1%	0.2%	0.2%
Minor	5%	1 m/km	0.4%	1.1%	1.6%	0.7%	0.2%	0.1%
		2 m/km	0.6%	2.0%	2.8%	1.2%	0.4%	0.1%
		3 m/km	1.0%	2.9%	4.1%	1.8%	0.5%	0.1%
	10%	1 m/km	0.6%	1.7%	2.0%	0.9%	0.2%	0.1%
		2 m/km	1.1%	3.1%	3.6%	1.4%	0.4%	0.2%
		3 m/km	1.7%	4.6%	5.4%	2.0%	0.5%	0.2%
	15%	1 m/km	0.9%	2.1%	2.3%	0.8%	0.3%	0.1%
		2 m/km	1.6%	3.7%	4.0%	1.5%	0.4%	0.1%
		3 m/km	2.4%	5.6%	6.0%	2.1%	0.6%	0.1%

5.2.3 Impact of Overweight Traffic on Pavement Performance under Dynamic Loads

Previous studies have proved that overweight trucks would accelerate pavement deterioration and shorten pavement service life using M-E pavement design method [20], [24]. Rys et al. (2016) quantifies the fatigue life reduction of asphalt pavement caused by combined traffic on the basis of the axle load distribution and percentage of overweight vehicles. They found that the increase of percentage of overweight vehicles from 0% to 20% could induce as high as 50% reduction in fatigue life of asphalt pavement. Titi et al. (2018) investigated the influence of overweight truck traffic on the pavement performance of four flexible pavement structures in Wisconsin using the M-E pavement design method and field investigation. It was suggested that the proportion of pavement damage induced by overweight trucks increased most of the pavement distresses by 0.5% to 4%. Few studies have investigated the overweight impact on pavement distresses considering dynamic loads due to rough surface conditions. In this study, the impact of overweight traffic on reflective fatigue cracking of AC overlay on asphalt pavement would be investigated using the dynamic axle load spectra in M-E pavement design.

New Jersey Department of Transportation defined 356 kN (80 kips) as the legal limit of gross vehicle weight. 1 kip (1000-pound force) equals to 4.45 kN (kilonewton). The legal weights of single axle on non-Interstate and Interstate highways are 100 kN (22.4 kips) and 89 kN (20 kips), respectively. The legal weight of tandem axle is 151 kN (34 kips) [96]. The WIM data was categorized into two traffic groups. The first group included the trucks within the legal weight limit and the overweight trucks (total traffic), and the second group only included the trucks within the legal weight limit (non-overweight traffic). The considered legal weight limits on single, tandem, and tridem, and quad axles were 89 kN (20 kips), 151 kN (34 kips), 187 kN (42 kips), and 240 kN (54 kips), respectively. Figure 5.8 presents the static and dynamic axle load spectra of non-overweight traffic on major and minor highways. The overweight weight percentage were 5.4%, 5.8%, 6.2%, and 6.5% corresponding to the scenarios of static load on smooth pavement surface and dynamic load on rough pavement surface with the IRI values of 1 m/km, 2 m/km, and 3 m/km. For minor highways, the overweight percentage were 3.5%, 3.6%, 3.7%, and 3.9% when static load and dynamic loads were induced on the rough pavement surfaces and when the IRI values of 1 m/km, 2 m/m, and 3 m/km were considered.

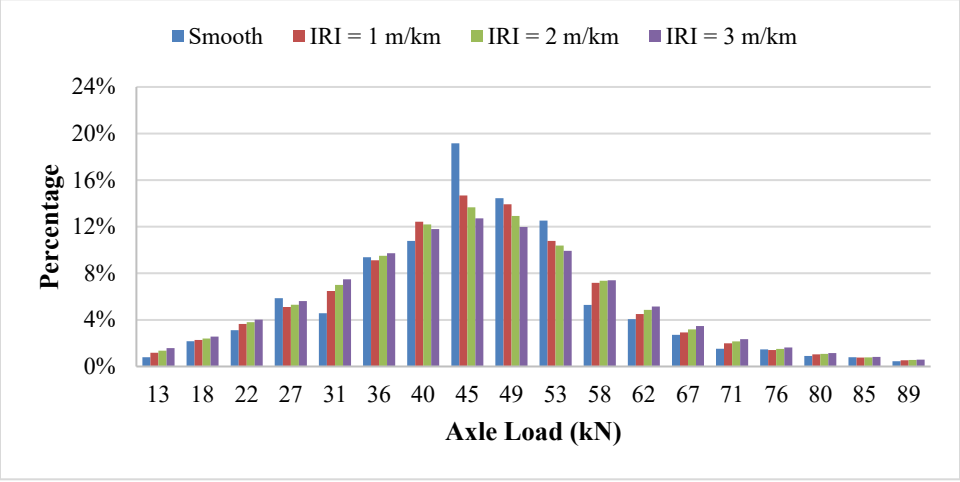

(a)

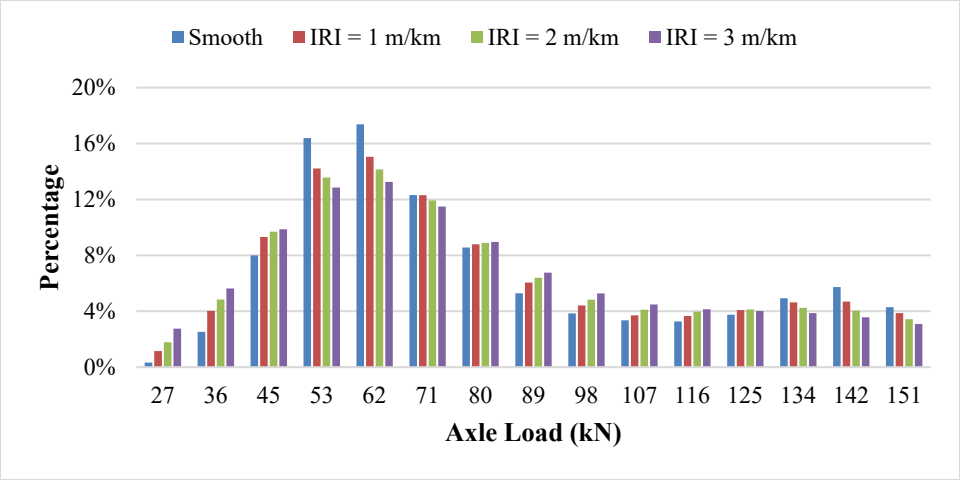
Smooth
IRI = 1 m/km
IRI = 2 m/km
IRI = 3 m/km
20%
16%
12%
8%
4%
0%
Percentage
27 36 45 53 62 71 80 89 98 107 116 125 134 142 151
Axle Load (kN)

(b)

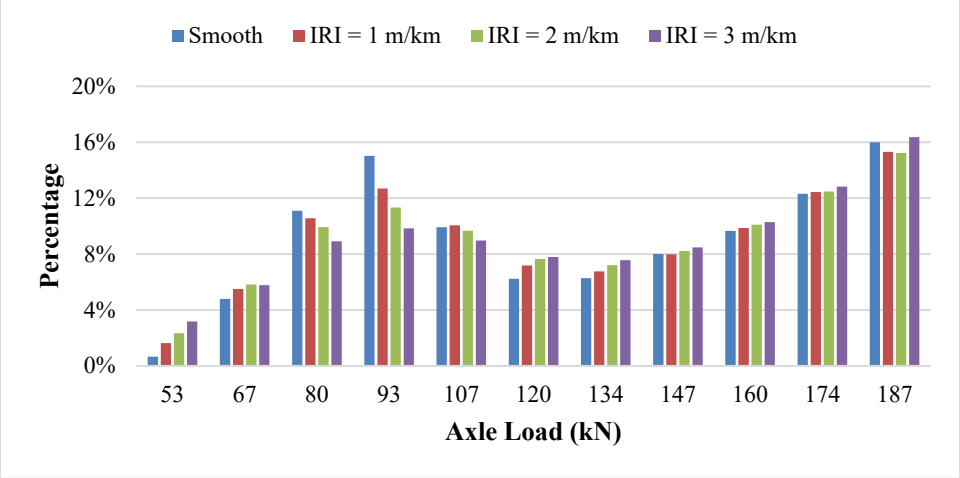
Smooth
IRI = 1 m/km
IRI = 2 m/km
IRI = 3 m/km
20%
16%
12%
8%
4%
0%
Percentage
53 67 80 93 107 120 134 147 160 174 187
Axle Load (kN)

(c)

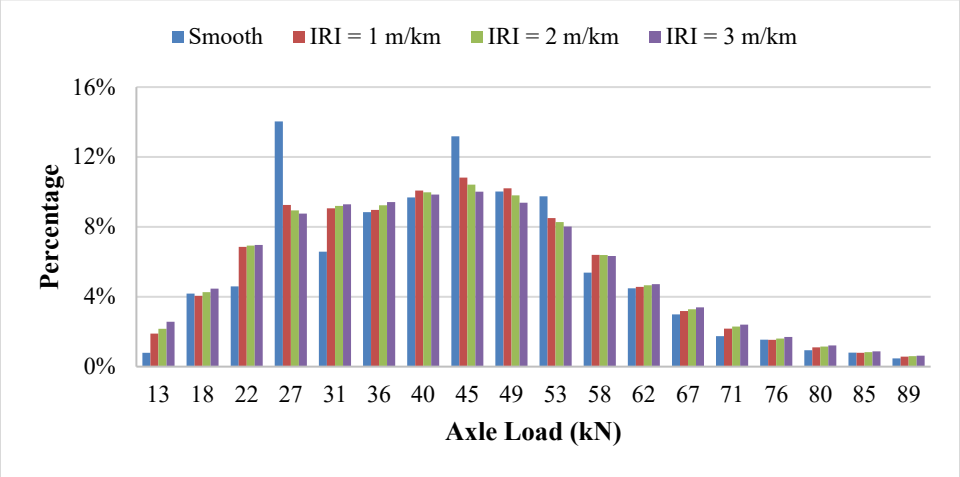
Smooth
IRI = 1 m/km
IRI = 2 m/km
IRI = 3 m/km
16%
12%
8%
4%
0%
Percentage
13 18 22 27 31 36 40 45 49 53 58 62 67 71 76 80 85 89
Axle Load (kN)

(d)

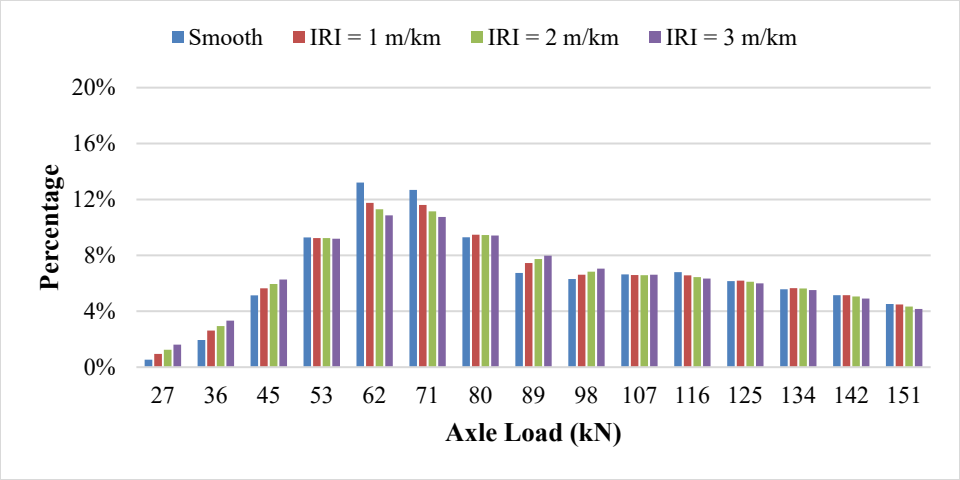

(e)

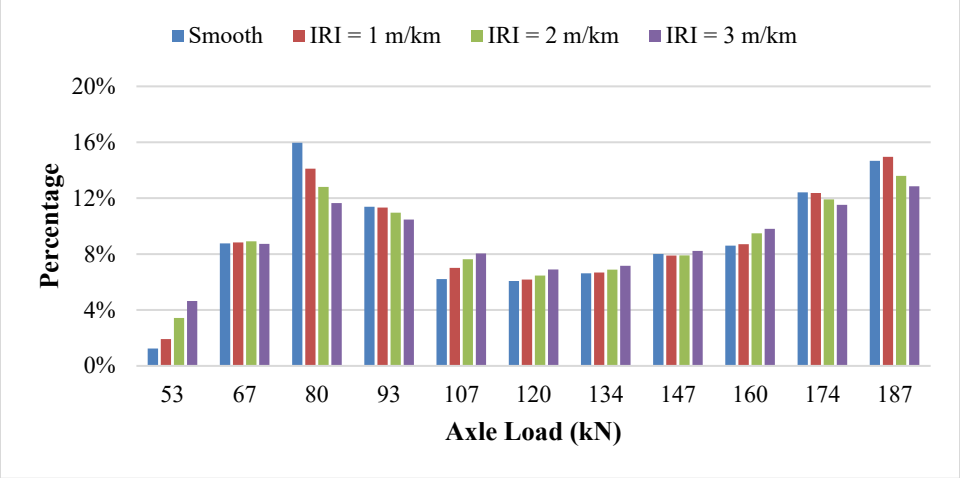

(f)

Figure 5.8 Static and dynamic axle load spectra of non-overweight traffic: (a) single axle (major); (b) tandem axle (major); (c) tridem axle (major); (d) single axle (minor); (e) tandem axle (minor); and (f) tridem axle (minor)

Figure 5.9 (a) illustrates the reflective fatigue cracking in the pavement structures on major highway under the static and dynamic loads of total and non-overweight traffic. Slower propagation of reflective fatigue cracking was observed when dynamic loads were considered because of the exclusion of heavier axle loads in non-overweight traffic scenario. The exclusion of dynamic overweight axle loads decreased the reflective fatigue cracking when dynamic loads were considered. However, the terminal percentages of reflective cracking under total and non-overweight traffic were identical due to the dominant role of existing cracking in the cracking development in pavement overlay design. Figure 5.9 (b) presents the reflective fatigue cracking in the pavement structures on minor highway under the static and dynamic loads of total and non-overweight traffic. Taking into account the fact that dynamic axle load spectra accelerated the pavement distress under total traffic and decelerated the pavement distress under non-overweight traffic, the impact of overweight traffic on pavement distress would be significant when dynamic loads were considered. It suggested that the negative influence of overweight traffic on pavement distresses were underestimated if static axle load spectra were applied in the M-E design.

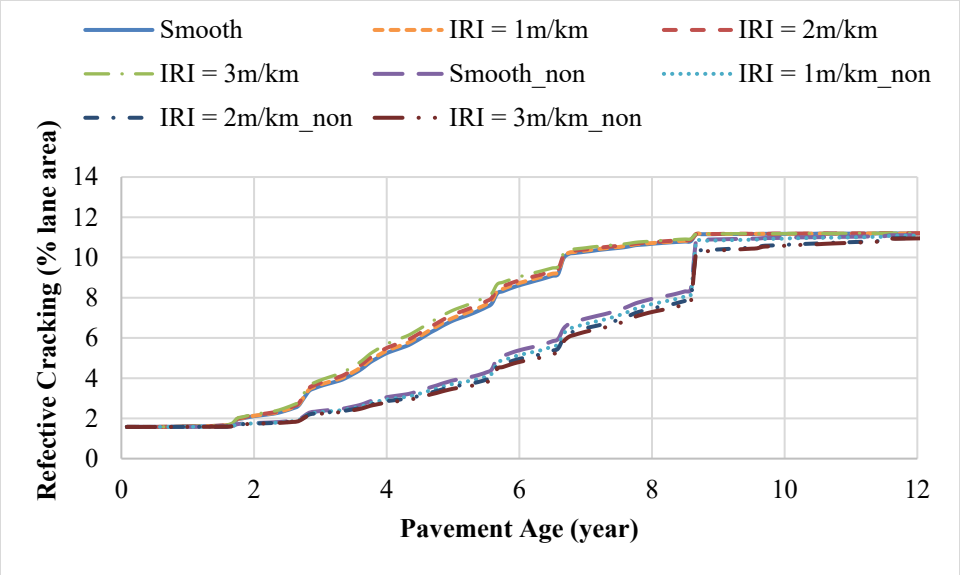

(a)

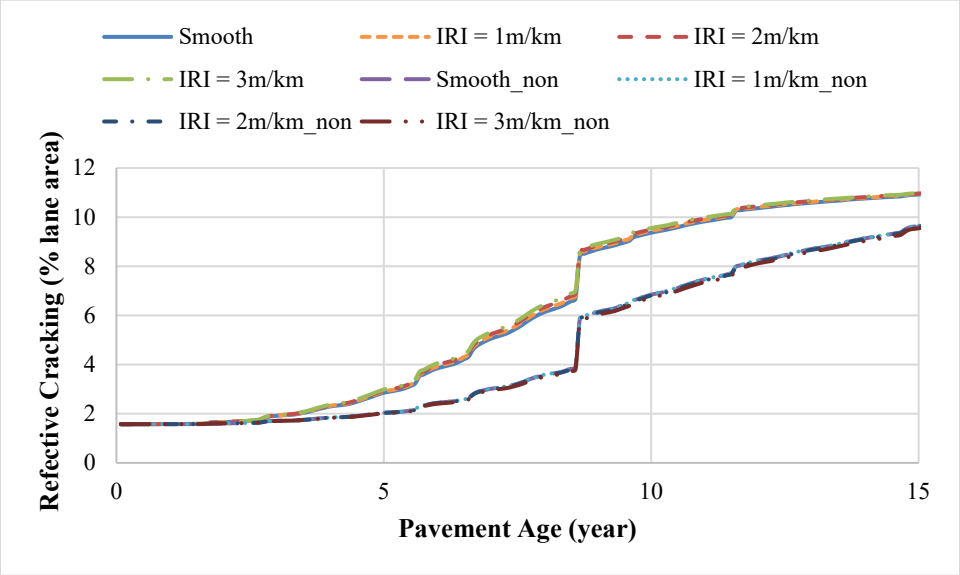

(b)

Figure 5.9 Fatigue cracking (reflective) of (a) major highway and (b) minor highway under total and non-overweight traffic (10% existing cracking)

The design reliability is supposed to be selected in balance with the performance criteria. The recommended reflective fatigue cracking (alligator cracking) of AC overlay on Interstate and primary highways are 10% and 20%, respectively. The recommended rut depth on Interstate and primary highways are 10.16 mm (0.4 inch) and 12.7 mm (0.5 inch), respectively. The recommended reliability level of principal arterials is 90% [116]. The considered criteria of fatigue cracking were 10% and 5% due to the limit of cracking propagation as shown in Figure 5.6 (a) and Figure 5.7 (a). To quantify the effect of overweight traffic loading on pavement distress, the reduction ratio of pavement service life was defined by Eq. 36.

$$R_r = \frac{L_T - L_N}{L_N} \tag{36}$$

where, R_r is the reduction ratio of pavement service life; L_T is the service period when a given level of pavement distress occures under total traffic; and L_N *is the* service period when a given level of pavement distress occures under non-overweight traffic.

Since the terminal rut depth at the end of design life was much smaller than the recommended values as shown in Figure 5.6 (b) and Figure 5.7 (b), the pavement service life determined by rut depth and corresponding reduction ratio due to dynamic loads were not considered in this study. Figure 5.10 shows the impact of overweight traffic on reduction ratio of pavement life considering different percentage of existing fatigue cracking in the AC layers. The considered threshold of reflective fatigue cracking was 5%. The analysis results indicated that the dynamic axle load spectra increased the impact of overweight traffic on reflective fatigue cracking, and the pavement structure on major highway tended to be more sensitive to the overweight traffic loading. One of the reasons would be the greater values of DLC corresponding to the higher operational speed on major highways. Pavement service life was found to be reduced with the existing fatigue cracking increased and the reduction ratio of pavement service life increased with the existing fatigue cracking increased. The effect of existing cracking had more significant impact on the pavement structure on major highway. The service life of pavement structure with 15% existing fatigue cracking was reduced by additional 12%, which increased the reduction ratio of pavement life up to 46%.

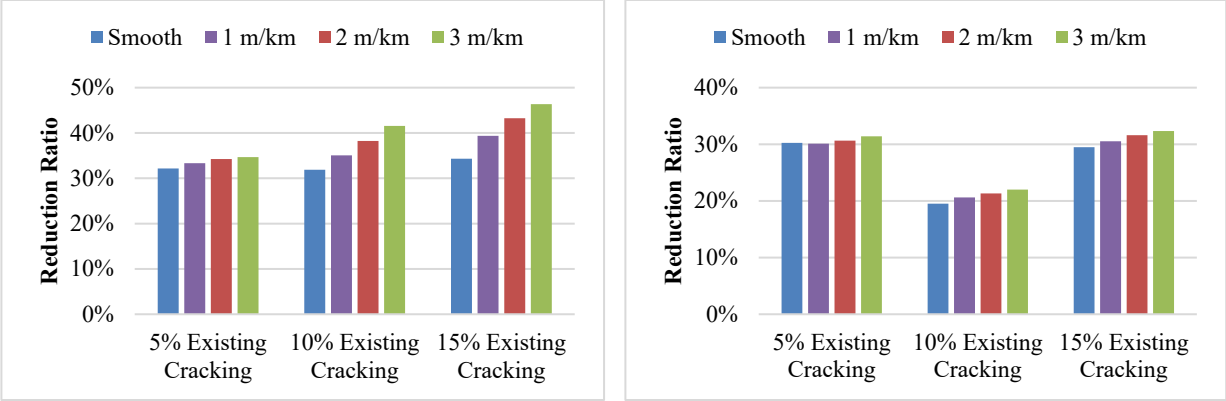

Figure 5.10 Impact of overweigh traffic on reduction ratio of pavement life considering different percentages of existing fatigue cracking: (a) major highway; and (b) minor highway

5.2.4 Discussion

The M-E outputs indicated that dynamic loads increased IRI, rut depth, and reflective fatigue cracking during pavement service period, as expected. The effect of dynamic loads on reflective fatigue cracking was relatively more significant as compared to the effects on rut depth. The impact of dynamic loads on reflective fatigue cracking was distinguished at early stage of service period and eliminated after 10-year analysis period when the propagation of reflective cracking reached to a specific level which was dominated by the existing cracking in AC layer. The impact of dynamic loads on fatigue cracking was not so significant as that in previous work because of the lower vehicle speed and higher level of terminal fatigue cracking. The impact of dynamic loads on rut depth was limited due to the pavement structure type [114] .

The analysis results indicated that the dynamic axle load spectra enhanced the impact of overweight traffic on reflective fatigue cracking, and the pavement structures on major highways would be more sensitive to the overweight traffic loading due to the greater DLCs excited at higher operational speed on major highway. The pavement service life was found to decrease with the percentage of existing fatigue cracking increased, and the reduction ratio of pavement service life increased with the existing fatigue cracking percentage increased. The effect of existing cracking had more significant impact on the pavement structure on major highway.

5.3 Summary of Mechanistic–Empirical Analysis of Pavement Performance

This study quantified the impact of dynamic traffic on pavement distress of AC overlay on asphalt pavement using M-E pavement design method. Dynamic tire forces were calculated for single, tandem, and tridem axles considering various IRI values of pavement profiles and axle loads. The calculated DLCs of dynamic tire forces increased as IRI values increased but decreased with axle loads increased. The nonlinear regression models of DLC with respect to IRI and axle loads were derived to predict the DLC values given any axle load interval designated by MEPDG. The dynamic loads excited by rough pavement surface condition were considered by transforming the static axle load spectra to dynamic axle load spectra. After the modification, the spikes in the distribution of axle loads were flattened because of the greater deviation of dynamic loads. The increase of DLC led to a decrease in the percentage of lighter loads but an increase in the percentage of heavier loads.

The impact of dynamic loads on reflective fatigue cracking was distinguished at early stage of service period and eliminated after 10-year analysis period when the propagation of reflective cracking reached to a specific level which was dominated by the existing cracking in AC layer. The dynamic axle load spectra enhanced the impact of overweight traffic on reflective fatigue cracking, and the pavement structures on major highways tend to be more sensitive to the overweight traffic loading because of the greater DLCs excited at higher operational speed on major highway.

A methodology was proposed to quantify the dynamic axle load spectra on the performance of AC overlay on flexible pavement considering pavement longitudinal unevenness, and typical pavement structures of a major route and a minor route were illustrated in the case study. The proposed method could be extensively applied to other flexible pavement structures in MEPDG. In future study, the analysis results need to be verified based on the field pavement performance subjected to the dynamic loads and static loads which might be difficult to capture in the field survey now.

6. PREDICTING ASPHALT PAVEMENT TEMPERATURE WITH REGRESSION AND NEURAL NETWORKS

The precision of WIM measurement systems can be significantly influenced by pavement temperature variations, which alter strain signals collected by sensors beneath the pavement. Studies have shown substantial changes in elasticity modulus during winter, underscoring the importance of accurate pavement temperature data. Despite the direct collection of pavement temperature by embedded sensors, researchers seek alternative approaches due to limitations such as cost and durability issues. Pavement temperature prediction models, leveraging comprehensive weather data, including temperature, humidity, wind, and precipitation, offer promising avenues. However, challenges persist in data acquisition methods, as many research models' validations rely on estimates due to a lack of true pavement temperatures at various layers. Additionally, existing prediction models often focus solely on air temperature or pavement surface temperature, neglecting crucial environmental data. Furthermore, available models typically target specific depths of interest, lacking a complete understanding of prediction performance across various depths, including the base layer. These challenges underscore the need for robust solutions in WIM technology to ensure accurate and reliable measurements.

This study aims to overcome challenges in pavement temperature modeling by employing empirical modeling techniques to predict temperature variations at different depths, including the base layer. By integrating data from nearby weather stations and field observations at MnROAD, the research will develop and compare multiple models to accurately predict road temperature, offering insights for selecting features and determining optimal sensor placement for enhanced weigh-in-motion system performance.

6.1 Field Study Facility

The experimental data were collected through a field test conducted at MnROAD, a pavement test track consisting of various research materials and pavements owned and operated by the Minnesota Department of Transportation. MnROAD includes 3 miles of mainline (I-94 interstate), 3.5 miles of the original westbound I-94, and a 2.5-mile low volume road. There are over 80 distinct test sections located on the mainline and the original westbound I-94. The layout of the sensors used to collect data for the field test is shown in Figure 6.1(a). The pavement temperature was collected in the location depicted in Figure 6.1(c). Meanwhile, as shown in Figure 6.1 (b) and (d), two weather stations located on the north-west (NW) and south-east (SE) sides of the test road section were used to collect weather conditions such as: wind speed and direction, air temperature, humidity, etc. Furthermore, Figure 6.2 displays the cross-section of the structure of the tested pavement, which comprises hot mix asphalt (HMA), MnDOT Class 6 granular base, MnDOT Class 3 sub-base, selected granular layer, and clay loam [117].

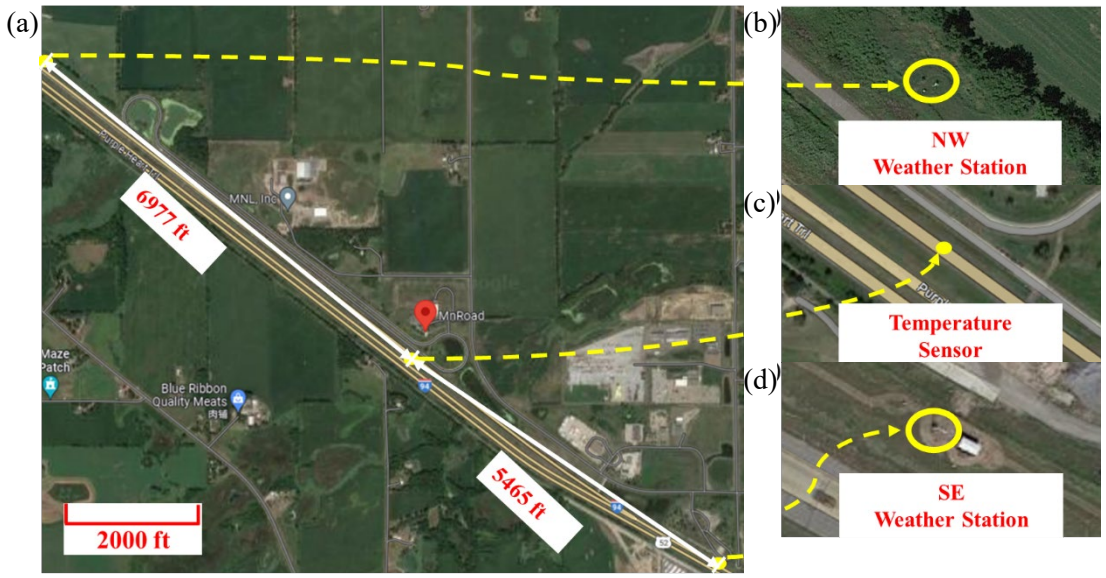

Figure 6.1 Satellite view of the (a) MnROAD research area; (b) NW weather station; (c) road embedded temperature sensor location; and (d) SE weather station

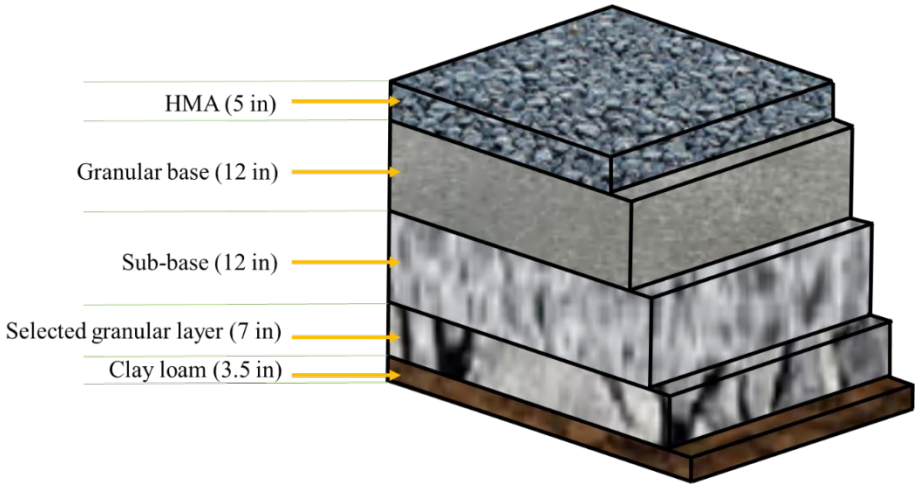

Figure 6.2 Cross section of the pavement in tested road section

6.2 Weather Factors and Temperature Data Collection

To predict the temperature of asphalt pavement at various depths using weather station (NW) data, this study utilized a dataset spanning 52 days from August to September, with recordings taken every 15 minutes for 24 hours per day.

True pavement temperature data beneath the pavement surface, ranging from 0.25 to 12 inches, was collected using the thermocouple embedded at the test location. These ground truth measurements then were used to verify the accuracy of the prediction models. In addition, the models were validated using weather data from a second weather station (SE).

Table 6.1 presents a comprehensive list of the weather factors collected from the weather stations. These factors include wind speed and direction, air temperature, humidity, barometric pressure, solar radiation, and precipitation.

Table 6.1 Weather factors collected by NW and SE weather station

Description	Unit
Air Temperature	Celsius
Atmospheric Pressure	Millibars
Heated Rain Gauge Precipitation	inches
Relative Humidity Percent	%
Net Radiation	Watts/Square Meter
Wind Direction from North	Degrees
Wind Average Speed	Meter/Second
Gust Maximum Speed	Meter/Second
Gust Direction from North	Degrees

Among the collected weather factors, an example of air temperature data is presented in Figure 6.3 (a). The air temperature range for NW and SE weather stations is from 3.98° to 32.16° and 4.85° to 32.75° Celsius, respectively. The temperature data collected by the thermocouple is shown in Figure 6.3 (b), and from this data it is clear to see that pavement temperature at a depth of 0.25 inches has the largest variation and temperature at a depth of 12 inches has the smallest variation within the same day. Given space limitations, this plot only shows the temperature at a depth of 0.25 inches rather than display all data at seven depths. Figure 6.3 (c) shows a comparison between the air temperature collected by the two weather stations and the temperature measured 0.25 inches below the pavement surface. The lowest and highest temperatures were recorded at a depth of 0.25 inches below the road surface, with values of 8.41° and 51.65° Celsius, respectively. It is clear that the pavement temperatures at 0.25 inches differ significantly from the corresponding air temperatures collected by NW and SE weather station.

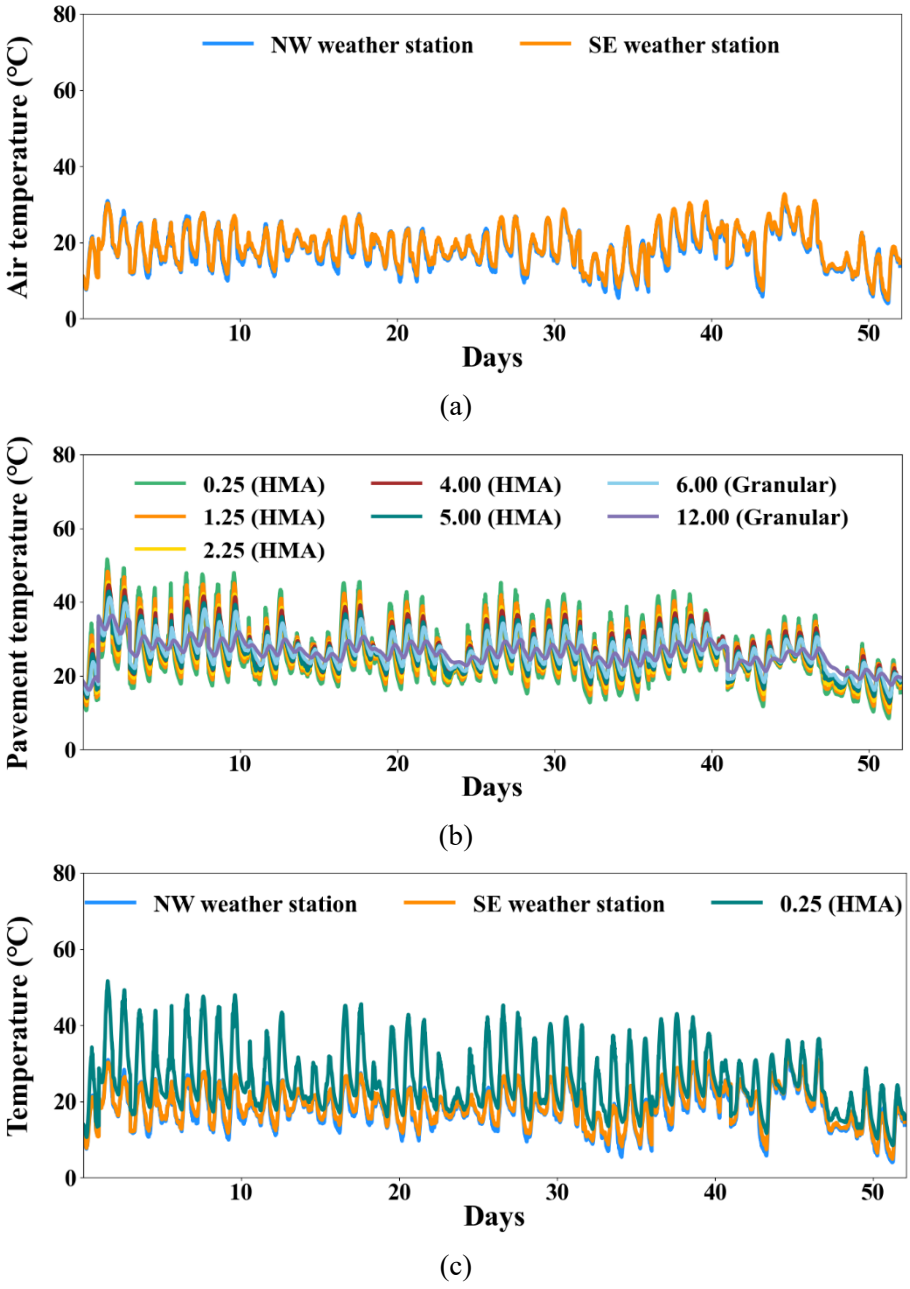

Figure 6.3 Collected temperature by (a) the NW and SE weather stations; (b) thermocouple at varied depts of pavements, and (c) comparing the NW and SE weather stations and the thermocouple's data at a depth of 0.25 inch

6.3 Data Analysis and Development of Prediction Models

As there are multiple weather factors that can influence the temperature of the pavement's surface and other layers, it is important to recognize that some factors have a significant influence while others have marginal effects, leading to a trade-off between including all factors for improved accuracy and the corresponding increase in processing time and costs. [118]. A normality test on both the surface temperature and base layer's temperature data and the weather station data was conducted, to select the

appropriate correlation tests because some tests have the normality assumption. Then the input factors correlation levels with pavement temperature for pavement prediction models are determined with the correlation coefficient method chosen through the normality test. This study intends to train regression models with 1) all nine weather factors and 2) only the ones that show a strong to weak correlation relationship with asphalt pavement temperature. Four regression models are evaluated in this study.

6.3.1 Normality test and feature selection methods

Optimal data analysis relies heavily on selecting appropriate feature selection methods, which requires first assessing the dataset's conditions, including its normal distribution. In this study, the Shapiro-Wilk test, a widely used normality test [119], was chosen for this purpose because it has been shown to have greater power in detecting non-normality compared to other normality tests [120]. Given a variable O with ordered random samples, $O_1, O_2, O_3, \dots, O_l$ (l is the total number of the random samples), where $O_1 \leq O_2 \leq O_3 \leq \cdots \leq O_l$, $\bar{O}$ is the sample mean, Shapiro and Wilk [121] proposed the W test based on the statistic which is defined as:

$$W = \frac{(\sum_{l=1}^{m} a_l O_l)^2}{\sum_{l=1}^{m} (O_l - \bar{O})} \tag{37}$$

where

$$a_l = (a_1, \dots, a_l) = \frac{m^T V^{-1}}{(m^T V^{-1} V^{-1} m)^2} \tag{38}$$

where $m = (m_1, \dots, m_l)^T$ denote the expected values of the order statistics of a sample of independent and identically distributed random variables, drawn from the standard normal distribution. The covariance matrix, V, characterizes the relationship between these order statistics [122].

Two widely recognized methods for feature selection are Pearson's and Spearman's correlation coefficients [123], [124]. Pearson's correlation coefficient necessitates normally distributed continuous variables and relies on a parametric test for computation, whereas Spearman's correlation coefficient is a non-parametric measure of the strength and direction of the relationship between two variables, which does not assume that the data follow a normal distribution [125]. Given two variables X_1 and X_2, with n samples each, the Pearson correlation coefficient (r_p) and Spearman's correlation coefficient (r_s) can be determined by [124]:

$$r_p = \frac{\sum_{j=1}^{n} (X_{1,j} - \overline{X_1})(X_{2,j} - \overline{X_2})}{\sqrt{(\sum_{j=1}^{n} (X_{1,j} - \overline{X_1})^2)(\sum_{i=1}^{n} (X_{2,j} - \overline{X_2})^2)}} \tag{39}$$

where, $X_{1,j}$ and $X_{2,j}$ are the variable samples, and j = 1, 2, 3, … n. $\overline{X_1}$ and $\overline{X_2}$ are means of the values in X_1 and X_2 variable.

$$r_s = 1 - \frac{6 \sum_{j=1}^{n} {d_j}^2}{n(n^2 - 1)} \tag{40}$$

where, d_i^2 is the difference between the j^{th} pair of the ranked variables, r_p and r_s both range in value from +1 to -1, where a value of +1 indicates a perfect positive correlation and a value of -1 indicates a perfect negative correlation between the two variables.

6.3.2 Pavement temperature prediction based on regression analysis

This study utilized four different methods for regression analysis, including 1) linear regression model, 2) simple polynomial regression model, (3) polynomial regression model (including a power of degree of the same input features), and 4) artificial neural network (ANN) modelling. Each model offers unique advantages. Linear regression stands out for its simplicity and ease of interpretation, providing a straightforward means to model variable relationships. Simple polynomial regression introduces curvature, improving modelling accuracy for complex dependencies. Polynomial regression with different degrees offers flexibility, capturing intricate relationships in various scenarios. ANN modelling excels at handling complexity and nonlinearity. Using the values of the correlation coefficients, this study determined the strength of the relationship between the weather factors and asphalt pavement temperature, ranging from perfect to weak. Relevant weather factors were included in the analysis to predict the temperature of the pavement's surface and base layer using various regression models. The comprehensive examination under different conditions and feature sets equips researchers with valuable insights for selecting the most suitable model for their specific research requirements. Details of the models employed in this study are presented below.

Linear regression model

Linear regression is a statistical method used to model the relationship between a dependent variable and one or more independent variables. It is often preferred for its simplicity, making it easy to understand and interpret. Given N independent variables (X_1, X_2, X_3, … X_N) and a dependent variable (Y), the X and Y following the linear regression relationship as [126]:

$$Y_j = \beta_0 + \beta_1 X_{1,j} + \beta_2 X_{2,j} + \beta_3 X_{3,j} + \cdots + \beta_N X_{N,j} + \varepsilon_j \quad (41)$$

where β_0 represents the Y-intercept of the regression surface, β_j (j = 1,2, 3, …, N) is the slope of the regression surface with respect to variable $X_{i,j}$, Y_j is the dependent variable value for observation j, and ε_j represents the random error component for the j^{th} case.

Polynomial regression model

Polynomial regression is a type of regression analysis that models the relationship between a dependent variable and one or more independent variables by fitting a polynomial equation to the data. Compared to the linear regression model, polynomial regression fits a broad range of functions, providing a better approximation of the relationship between the dependent and independent variables, especially when the relationship is curvilinear [127]. To clearly present the research, this study specifies two types of polynomial regression. The first type includes interaction effects, which differ from linear regression. The second type includes higher order polynomial terms of the same input features. For the first type of the model, according to the equations used by Kim et al. [128] and Qiu et al. [129], when the degree of the polynomial regression model is set to 2, the model includes only the features that are products of, at most, two distinct input features. This means that the terms with a power of 2 of the same input features are excluded. The resulting equation can be expressed as:

$$Y_j = \beta_0 + \beta_1 X_{1,j} + \cdots + \beta_N X_{N,j} + \beta_{N+1} X_{1,j} X_{2,j} + \cdots + \beta_{\frac{N(N+1)}{2}} X_{(N-1),j} X_{N,j} + \varepsilon_j \quad (42)$$

For the second type polynomial regression model that includes terms with a power of 2 of the same input features can be expressed as:

$$\begin{aligned} Y_j = \beta_0 + \beta_1 X_{1,j} + \cdots + \beta_N X_{N,j} + \beta_{N+1} X_{1,j} X_{2,j} \\ + \cdots + \beta_{\frac{N(N+1)}{2}} X_{(N-1),j} X_{N,j} + \beta_{\frac{N(N+1)}{2}+1} {X_{1,j}}^2 + \cdots + \beta_{\frac{N(N+3)}{2}} {X_{N,j}}^2 \\ + \beta_{\frac{N(N+3)}{2}+1} {X_{1,j}}^2 X_{2,j} + \beta_{N^2+N} {X_{(N-1),j}}^2 X_{N,j} + \varepsilon_j \end{aligned} \tag{43}$$

Artificial neural network model

ANN has been widely used to solve the regression problems through a learning process by adjusting the values of the connection weights among the neurons [130]. Shan et al. [131] conducted a study on asphalt pavement deformation, which incorporates various factors, laboratory tests, and three neural network algorithms. This study used the multilayer perceptron, which is the most widely adopted ANN model in different industries [132]. A multilayer perceptron may have one or more hidden layers and finally an output layer. Multilayer perceptron is described as being fully connected, with each node connected to every node in the next and previous layer [133]. Two hidden layers were considered in this study as shown in Figure 6.4. Activation maps are processed through a nonlinear activation function. While the traditional activation function is typically a sigmoid function [134], the rectified linear unit (ReLU) has gained popularity in recent years [135] because ReLU has been shown to accelerate the convergence of stochastic gradient descent when compared with sigmoid functions. Furthermore, ReLU can be easily implemented by thresholding activation maps at zero [136].

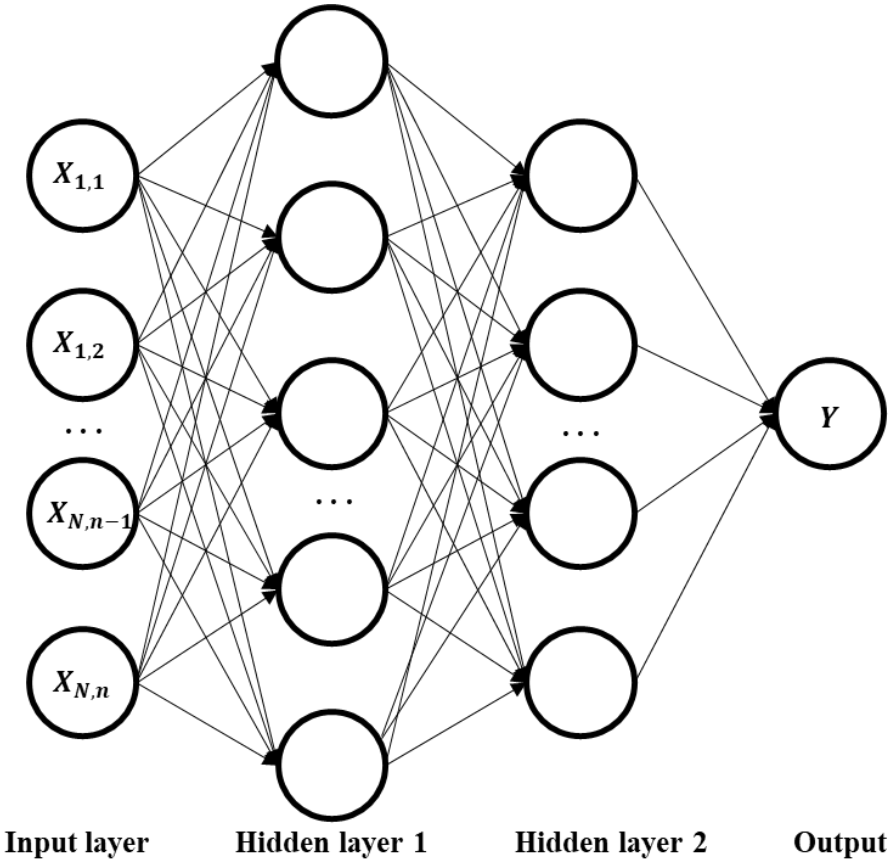

Figure 6.4 A multilayer perceptron with two hidden layers

To assess the predictive ability of the proposed models, this study used two evaluation metrics: root mean squared error (RMSE) and R-squared (R^2). While RMSE can be informative, it has a range between zero and positive infinity and may not provide meaningful information about the performance of the regression with respect to the distribution of the ground truth elements [137]. Therefore, Chicco et al. suggest that R^2 should be used as the standard metric to evaluate regression analyses in any scientific domain [137]. The RMSE and R^2 value is produced by [138]:

$$RMSE = \frac{\sum_{j=1}^{n}\left(\hat{Y}_j - Y_j\right)^2}{n} \tag{44}$$

$$R^2 = \frac{SSR}{SST} = \frac{\sum_{j=1}^{n}\left(\hat{Y}_j - \bar{Y}\right)^2}{\sum_{j=1}^{n}\left(Y_j - \bar{Y}\right)^2} \tag{45}$$

where SSR and SST is sum of squared regression and sum of squared total (total variation), respectively. $\hat{Y}_j$ is the predicted value of dependent variable for observation j.

6.4 Evaluation of Weather Factors on Temperature of Asphalt Pavement using Statistical Analysis and Machine Learning Models

In this section, true pavement temperatures at various depths are used to test the normality of the weather factors and asphalt pavement temperature. This assessment aimed to establish the relationship between asphalt pavement temperatures and various weather factors. Subsequently, the correlation coefficient was calculated to help determine which factors can be used to fit the four different regression models. The analysis of the results involved examining the R^2 and RMSE values under 28 conditions (7 different depths and 4 different sets of features selected based on different correlation coefficients levels) for each regression model.

6.4.1 Normality Test of Weather Factors and Asphalt Pavement Temperature

The normality of true temperature in asphalt pavement and weather factors collected by weather stations was investigated in this section, to check if the data conforms to a normal distribution. The Shapiro-Wilk test is employed to assess the normality of the true temperature in pavement and weather factors, and the resulting p-Values are reported in Table 6.2. The p-Values for all the tested parameters are less than 0.05, indicating that none of the features follow a normal distribution. Results suggest that the weather station factors and asphalt pavement temperature values did not follow a normal distribution.

6.4.2 Correlation Analysis between Weather Factors and Road- embedded Temperature Sensors

In order to predict the temperature of pavement's surface and base layer accurately, this study utilized the weather factors (as presented in Table 6.1) collected by the weather stations as predictor variables, and the accuracy of the prediction was examined by the thermocouple temperature sensors embedded in the pavement.

Table 6.2 Results of Shapiro-Wilk Test for Normality of Weather Factors and Asphalt Pavement Temperature

Features	**p**-Value
Air Temperature	9.70E-04
Atmospheric Pressure	8.02E-03
Heated Rain Gauge Precipitation	3.61E-15
Relative Humidity Percent	5.41E-04
Net Radiation	2.37E-05
Wind Direction from North	2.29E-03
Wind Average Speed	3.19E-03
Gust Maximum Speed	2.32E-04
Gust Direction from North	1.65E-02
0.25 (HMA)	9.82E-36
1.25 (HMA)	1.22E-30
2.25 (HMA)	2.23E-24
4.00 (HMA)	9.35E-22
5.00 (HMA)	5.91E-17
6.00 (granular)	9.81E-12
12.00 (granular)	8.11E-26

Therefore, to predict the pavement and base layer's temperature, this study starts with all the available weather factors. Spearman's correlation coefficient was used to choose which weather factors would be included in the prediction since all the weather factors did not follow a normal distribution. The values of Spearman's correlation coefficient between the weather factors and the temperature at various depths below the road surface are shown in Figure 6.5. The results showed that there were no features that highly influenced the temperature at a depth of 12 inches. When the depth was between 0.25 inches and 6 inches, air temperature and relative humidity percent had a high influence on the temperature of surface and base layer, and net radiation influenced the temperature when the depth was more than 2.25 inches. Additionally, the correlation between the features and the asphalt pavement temperature decreased as the depth increased. The top significant weather conditions are air temperature, humidity, and radiations for temperatures at all depths especially for temperatures between surface to about 2.25 inches.

Depth	0.25	1.25	2.25	4.00	5.00	6.00	12.00
Air Temperature	0.89	0.86	0.80	0.75	0.72	0.61	0.28
Net Radiation	0.65	0.53	0.40	0.31	0.25	0.10	-0.17
Relative Humidity Percent	-0.63	-0.62	-0.60	-0.57	-0.55	-0.47	-0.26
Gust Maximum Speed	0.29	0.20	0.11	0.05	0.00	-0.10	-0.31
Wind Average Speed	0.23	0.15	0.07	0.02	-0.02	-0.11	-0.28
Heated Rain Gauge Precipitation	-0.16	-0.16	-0.15	-0.12	-0.14	-0.10	-0.05
Atmospheric Pressure	-0.10	-0.10	-0.11	-0.11	-0.11	-0.11	-0.07
Wind Direction from North	0.02	0.01	0.00	-0.01	-0.01	-0.03	-0.05
Gust Direction from North	0.02	0.01	0.00	-0.01	-0.01	-0.03	-0.04

$|r_s| \geq 0.4$
$|r_s| \geq 0.2$
$|r_s| \geq 0.1$
$|r_s| \geq 0$

Figure 6.5 Spearman's correlation coefficient between weather factors and temperature of the surface and base layer at various depths

6.4.3 Prediction of Surface and Base Layer's Temperature based on Weather Factors

This study explores various models to predict the surface and base layer's temperature using weather factors. The models considered include linear regression, simple polynomial regression, polynomial regression (including a power of degree of the same input features), and artificial neural network (ANN).

To fit the data to the four models, the study selected all weather factors and the weather factors based on their Spearman's correlation coefficient at three levels as being more than 0.1, 0.2, or 0.4. Since the correlation coefficient between weather features and temperature of surface and base layer changes at different depths, the number of features that fit the models also changes. This means that the number of independent variables and parameter values used to predict temperature are different even when fitting them to the same type of model.

For the entire weather station dataset, this study randomly assigned 80% of the data for training the models and the remaining 20% for testing the model's performance. The evaluation metrics used were R^2 and RMSE. To ensure consistency across all models, the same seed number was used to randomly split the data into training and testing sets for different depths. Otherwise, the results may vary if different random seeds are used.

Table 6.3 to 6.6 present the R^2 and RMSE obtained when fitting the features to the linear regression, polynomial regression, polynomial regression (excluding a power of degree of the same input features), and ANN; the number of features depends on the setting of the correlation coefficient values. When the correlation coefficient is more than 0.4, there are no R^2 and RMSE values available for the depth of 12 inches. This is because, at that depth, none of the features have a correlation coefficient greater than 0.4, which means that there is no significant relationship between the weather factors and the road temperature at that depth.

Linear regression

Table 6.3 displays the number of weather factors included in the model (n), and the two model performance measurements (R^2 value and RMSE) calculated with the NW weather station data. Referring to Table 6.3, the more features or weather factors will be included in the model if the Spearman's correlation coefficient rule is less utilized to guide the feature selection. For example, if we select the model based on strong correlation ($R^2 \geq 0.4$), a lower number of features will be selected (3 for depth at 0.25 inches), however if the correlation requirement is relaxed, more features will be selected (9 for $|r_s| \geq 0$). It is clear to see that the model performs better when the model includes more weather factors as R^2 values increase and RMSE values decrease which indicates a weaker relationship between the variables and a slight decrease in the accuracy of the predictions. However, there is minimal benefit gain when the Spearman's correlation coefficient is less than 0.2. The accuracy and relationship decrease for the linear regression model as the depth increases as shown when the R^2 value decrease and RMSE value increase slightly as the depth below the pavement increases from 0.25 to 4 inches. When the depth increases from 5 inches to 12 inches, corresponding to the granular base layer, distinct from the HMA layer above it, the R^2 value continues to increase. Additionally, when the absolute value of the correlation coefficient is less than 0.2, RMSE decreases. However, when the correlation coefficient is greater than or equal to 0.2, the RMSE increases on the granular base layer.

Table 6.3 Evaluation of linear regression model for predicting surface and base layer's temperature

Depth (in)	Correlation coefficient	$\|r_s\| \geq 0.4$	$\|r_s\| \geq 0.2$	$\|r_s\| \geq 0.1$	$\|r_s\| \geq 0$
	n	3	5	7	9
0.25 (HMA)	R^2	0.85	0.88	0.88	0.88
	RMSE	3.11	2.81	2.73	2.74
	n	3	4	7	9
1.25 (HMA)	R^2	0.78	0.82	0.83	0.83
	RMSE	3.32	3.01	2.94	2.94
	n	3	3	6	9
2.25 (HMA)	R^2	0.77	0.77	0.77	0.77
	RMSE	3.34	3.34	2.96	2.96
	n	2	3	5	9
4.00 (HMA)	R^2	0.64	0.67	0.69	0.74
	RMSE	3.51	3.36	3.26	2.99
	n	2	3	5	9
5.00 (HMA)	R^2	0.60	0.65	0.67	0.73
	RMSE	3.44	3.22	3.13	2.84
	n	2	2	7	9
6.00 (granular)	R^2	0.46	0.46	0.61	0.68
	RMSE	3.55	3.55	3.01	2.73
	n	0	4	5	9
12.00 (granular)	R^2		0.39	0.50	0.51
	RMSE		2.75	2.47	2.46

*n represents the number of weather factors included in the model.

Simple Polynomial Regression

As presented in table 6.4, compared to the linear regression model, fitting the features to a simple polynomial regression model shows performance improvements in the R^2 and RMSE values, except for depths of 2.25 inches where Spearman's correlation coefficients are greater than or equal to 0.2. The maximum R^2 value achieved is 0.91, representing a 0.03 improvement compared to the performance of the linear regression model. Additionally, the RMSE value shows a reduction of 0.36. Overall, the trend remains similar when varying both the Spearman's correlation coefficient and the depth. When the Spearman's correlation coefficient is lower, indicating a weaker initial correlation between variables, and there are more features in this range, it suggests that when incorporating features into the model based on the lower correlation coefficient, a larger number of features will be included. The inclusion of more features in the model improves its performance. However, the additional improvement in performance becomes less significant when adding more features with lower correlations. Based on the features obtained from the weather stations considered in this study, the models exhibit lower accuracy in predicting temperature as the depth increases.

Table 6.4 Evaluation of simple polynomial regression model for predicting surface and base layer's temperature

Depth (in)	Correlation coefficient	$\|r_s\| \geq 0.4$	$\|r_s\| \geq 0.2$	$\|r_s\| \geq 0.1$	$\|r_s\| \geq 0$
	n	3	5	7	9
0.25 (HMA)	R^2	0.87	0.90	0.91	0.91
	RMSE	2.93	2.55	2.40	2.38
	n	3	4	7	9
1.25 (HMA)	R^2	0.81	0.85	0.87	0.87
	RMSE	3.13	2.79	2.53	2.51
	n	3	3	6	9
2.25 (HMA)	R^2	0.74	0.74	0.83	0.84
	RMSE	3.15	3.15	2.56	2.50
	n	2	3	5	9
4.00 (HMA)	R^2	0.66	0.71	0.74	0.81
	RMSE	3.40	3.17	2.97	2.52
	n	2	3	5	9
5.00 (HMA)	R^2	0.62	0.68	0.73	0.81
	RMSE	3.36	3.05	2.84	2.39
	n	2	2	7	9
6.00 (granular)	R^2	0.47	0.47	0.66	0.77
	RMSE	3.51	3.51	2.81	2.33
	n	0	4	5	9
12.00 (granular)	R^2		0.42	0.55	0.59
	RMSE		2.67	2.36	2.23

*n represents the number of weather factors included in the model.

Polynomial Regression (Including a Power of Degree of the Same Input Features)

The data in Table 6.5 indicates that the polynomial regression model includes not only the interaction terms between different input features ($X_{1,j}X_{2,j}, X_{2,j}X_{3,j}, \dots, X_{(N-1),j}X_{N,j}$) as simple polynomial model but also includes higher power terms of the same input features ($X_{1,j}{}^2X_{2,j}, X_{2,j}{}^2X_{3,j}, \dots, X_{(N-1),j}{}^2X_{N,j}$). Table 6.5 presents the inclusion of features in the model and showcases the model's performance in terms of R^2 and RMSE at different depths and correlation coefficient scales. The polynomial regression model achieves a maximum R^2 value of 0.92, which is slightly superior to the simple polynomial regression and notably better than the linear regression. The overall pattern remains consistent with the previous two models.

Table 6.5 Evaluation of polynomial regression model (including a power of degree of the same input features) for predicting surface and base layer's temperature

Depth (in)	Correlation coefficient	$\|r_s\| \geq 0.4$	$\|r_s\| \geq 0.2$	$\|r_s\| \geq 0.1$	$\|r_s\| \geq 0$
	n	3	5	7	9
0.25 (HMA)	R^2	0.88	0.91	0.92	0.92
	RMSE	2.82	2.42	2.34	2.31
	n	3	4	7	9
1.25 (HMA)	R^2	0.82	0.87	0.88	0.88
	RMSE	2.98	2.57	2.46	2.41
	n	3	3	6	9
2.25 (HMA)	R^2	0.77	0.77	0.84	0.85
	RMSE	2.98	2.98	2.47	2.41
	n	2	3	5	9
4.00 (HMA)	R^2	0.67	0.74	0.75	0.83
	RMSE	3.36	2.99	2.90	2.43
	n	2	3	5	9
5.00 (HMA)	R^2	0.63	0.72	0.74	0.82
	RMSE	3.32	2.86	2.77	2.33
	n	2	2	7	9
6.00 (granular)	R^2	0.50	0.50	0.67	0.78
	RMSE	3.40	3.40	2.76	2.28
	n	0	4	5	9
12.00 (granular)	R^2		0.50	0.63	0.64
	RMSE		2.47	2.14	2.09

*n represents the number of weather factors included in the model.

Artificial Neural Network (ANN)

Table 6.6 demonstrates that the ANN model provides the highest level of accuracy in predicting pavement temperature. When considering all nine weather factors to forecast the pavement temperature at a depth of 0.25 inches, the ANN model achieves an impressive R^2 value of 0.96 and a RMSE of 1.69. When the depth increases to 12 inches, the RMSE reaches its lowest value of 1.40 and R^2 is 0.85. The overall pattern remains consistent with the previous three models. All models suggest increased performance when more weather factors are included, but with a decreasing marginal gain, and shows that prediction accuracy decreases as the depth of the pavement increases.

Table 6.6 Evaluation of artificial neural network model for predicting surface and base layer's temperature

Depth (in)	Correlation coefficient	$\|r_s\| \geq 0.4$	$\|r_s\| \geq 0.2$	$\|r_s\| \geq 0.1$	$\|r_s\| \geq 0$
	n	3	5	7	9
0.25 (HMA)	R^2	0.90	0.93	0.95	0.96
	RMSE	2.58	2.14	1.84	1.69
	n	3	4	7	9
1.25 (HMA)	R^2	0.86	0.90	0.92	0.93
	RMSE	2.69	2.22	1.99	1.84
	n	3	3	6	9
2.25 (HMA)	R^2	0.81	0.81	0.91	0.92
	RMSE	2.74	2.74	1.88	1.79
	n	2	3	5	9
4.00 (HMA)	R^2	0.69	0.78	0.83	0.90
	RMSE	3.28	2.77	2.42	1.81
	n	2	3	5	9
5.00 (HMA)	R^2	0.66	0.75	0.81	0.90
	RMSE	3.17	2.69	2.37	1.73
	n	2	2	7	9
6.00 (granular)	R^2	0.51	0.51	0.76	0.88
	RMSE	3.39	3.39	2.34	1.65
	n	0	4	5	9
12.00 (granular)	R^2		0.63	0.73	0.84
	RMSE		2.13	1.83	1.40

*n represents the number of weather factors included in the model.

In summary, the results reveal that all nine factors influence the surface and base layer's temperatures and contribute to increasing the R^2 while decreasing the RMSE, even when the included features are only those with small correlation coefficients. However, as the model includes additional features with lower correlation, the marginal gain in performance starts to decrease. In other words, the incremental improvement gained from including marginally correlated features becomes less pronounced. This raises a trade-off issue between time efficiency and higher accuracy because one weather factor is associated with one specific sensor - time efficiency when modelling - while inclusion of multiple weather factors requires additional data collection and resources for processing requirements, but results in higher accuracy. Therefore, finding a balance between data availability, time, and accuracy is crucial. Based on this study's results, only including the features that have a strong relationship with the road temperature does not significantly reduce the R^2 and RMSE values when compared to the model including all the weather features.

Comparing all the models, the ANN performs the best followed by polynomial regression model (including a power of degree of the same input features), the simple polynomial regression model, and lastly the linear regression model.

This research compares the predicted temperature generated by the four models based on all nine weather factors to the real temperature. Due to space limitations, this study presents the performance of four models in predicting the temperature at a depth of 0.25 inches as shown in Figure 6.6. The results show that the predicted temperature generated by the ANN model is almost identical to the real temperature experienced by the pavement, indicating that the ANN model has the best performance among the four models.

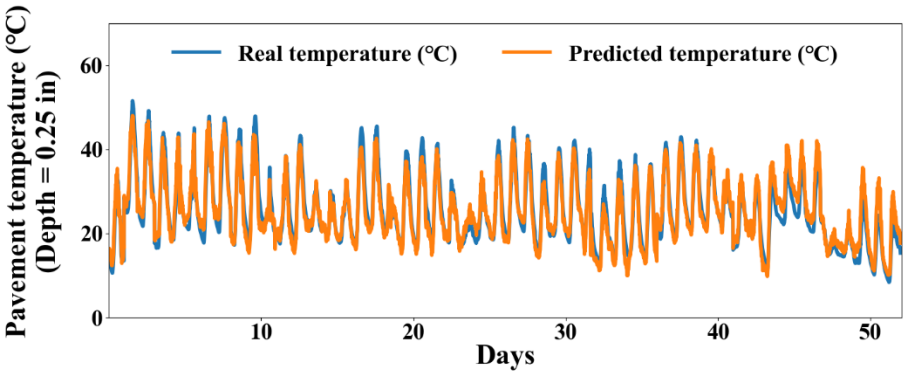

(a)

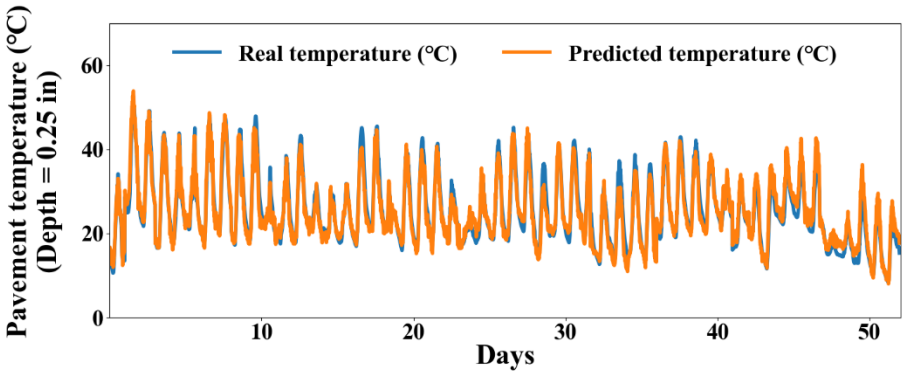

(b)

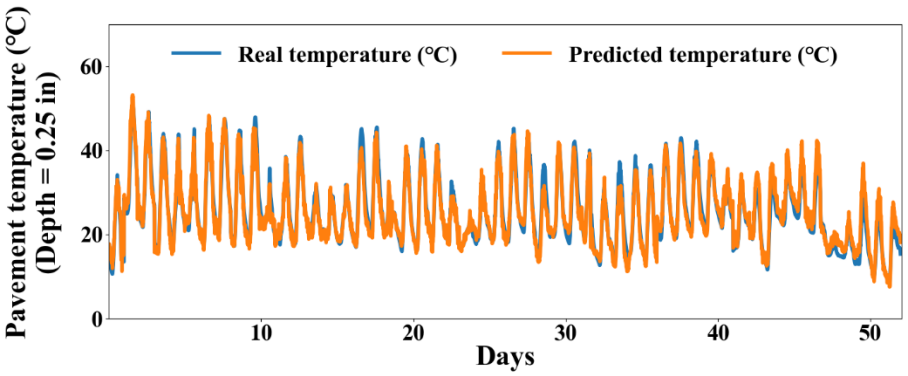

(c)

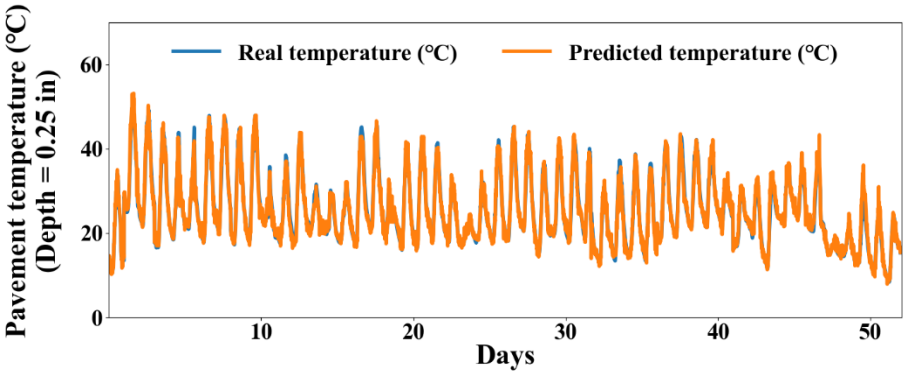

(d)

Figure 6.6 Real surface and base layer's temperature and predicted temperature by the (a) linear regression model; (b) polynomial regression model; (c) polynomial regression model (including a power of degree of the same input features), and (d) ANN model

Model Validation Based on the Secondary Weather Station

To assess the model's effectiveness for other weather stations located in different areas and using different sensors to collect the same weather factors, the performance of the generated model based on the data from the weather station NW was evaluated using weather station SE.

Figure 6.7 displays both the R^2 and RMSE values calculated based on the data from weather station SE (Figure 6.7 (b) and (d)) compared to the measurements with NW station data (Figure 6.7 (a) and (c)). Note the models are constructed with NW station data. So the tests performed with NW station data is considered as in-sample validation and the test performed with SE station data is considered as external-sample validation which can indicate the robustness of the model's performance.

The performance of the models is considered consistent with the two validation results. Overall, there is a little performance loss based on the validation performed with external-sample data compared to the in-sample data. Both performances suggest which models perform worst and which perform best, with the following order of worst to best; linear, simple polynomial (Polynomial 1), polynomial (which includes a power of degree of the same input features, polynomial 2), and ANN as shown in Figure 6.7 (b) and (d).

In general, model performance decreases with increasing depth, and the performance differences were most pronounced at a depth of 12 inches. However, compared to the R^2 values and RMSE calculated using data from weather station NW, those obtained using data from weather station SE showed a more significant decrease as depth increased (Figure 6.7 (b) and (d)). While the decrease in R^2 was not as apparent for depths of 0.25 and 1.25 inches when compared to the data from weather station NW, it became more significant as depth increased.

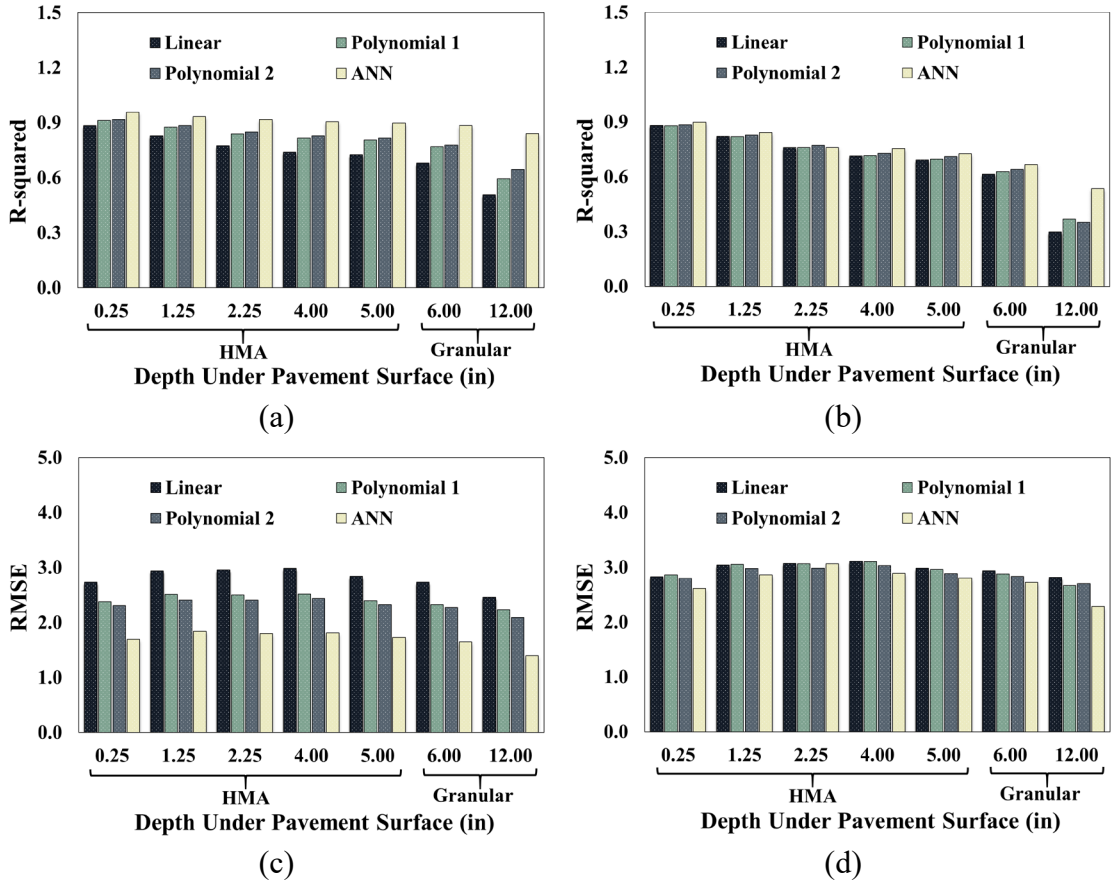

Figure 6.7 R^2 was calculated using data from weather station (a) NW and (b) SE, and RMSE was calculated using data from weather station (c) NW and (d) SE

6.5 Summary of Pavement Temperature Prediction Using Weather Station Data

From this work key findings are summarized as follows:

The pavement temperature data collected from the road embedded temperature sensor and weather stations do not follow a normal distribution. Furthermore, the Spearman's correlation coefficient between the weather factors and surface and base layer's temperature decreased as the depth increased, and results revealed that none of the weather factors have a strong correlation with pavement temperature when the depth is beyond 12 inches.

When more weather factors are included in the models, better performance is achieved. As depth increases, accuracy decreases in predicting pavement temperature.

To achieve the highest level of accuracy while maintaining cost efficiency, it is recommended to install the WIM sensor at a depth of 2.25 inches below the pavement surface. This placement enables accurate temperature calculations using a weather station sensor with a high degree of precision, as indicated by an R^2 value exceeding 0.8. Moreover, this approach streamlines the data requirements by focusing on three essential weather factors: air temperature, humidity, and radiation.

Among the four prediction models, the deep learning-based regression model, ANN, generated the best results at all pavement depths. When all the weather factors were considered and evaluated using the data collected by the embedded temperature sensor, the R^2 value was approximately 0.96, indicating a strong relationship between the predicted and actual temperature values. Additionally, the RMSE was found to be approximately 1.69°C, indicating the low average difference between the predicted and actual temperature values.

For ANN model, the R^2 can reach as high as 0.90 for predicting temperature at 0.25 inches by only including the top 3 weather factors suggested by Spearman's correlation coefficient (air temperature, radiation, and humidity) compared to 0.96 by including all 9 weather factors. This finding translates to a practice trade-off where the loss of prediction performance is only less than 0.06 however the number of sensors needed for data collection is reduced from 9 to 3. This trend is consistent for all the depths however, as depth increases there is more loss of performance in terms of R^2 while holding the same number of the significant weather factors.

The study constructed models with the data from weather station NW, and evaluated the performance based on in-sample R^2 and RMSE. Furthermore, the performance was validated with external data from weather station SE. The results confirmed that the model performance was robust and consistent for both stations, with the best-performing model being the ANN.

As the current study only validated the temperature prediction model in the selected location of Albertville, Minnesota, in future research, the validation of the temperature prediction model in diverse geographical locations will valuable to enhance its robustness and applicability. Additionally, there will be an emphasis on quantifying the temperature adjustment factors based on the predicted pavement temperature to improve the accuracy of the weigh-in-motion weight measurements. Moreover, other weather conditions' direct impacts on WIM weight measurements should be quantified to further improve WIM performance. For example, wind speed and direction can directly affect the wander of vehicles which in turn will impact the performance of a WIM system.

7. ASSESSING VEHICLE WANDERING EFFECT USING IN-PAVEMENT FIBER-BRAGG SENSORS AND CAMERA SYSTEM

After identifying methods to obtain pavement temperature, which significantly influence the accuracy of WIM measurements, this section aims to tackle challenges in WIM systems, with a particular focus on embedded sensor and image-capturing systems. Embedded sensors, despite offering advantages like immunity to electromagnetic interference, face challenges such as the wander effect, leading to inaccuracies in weight measurements due to misalignment with wheel positions. In contrast, image-capturing systems rely on tire inflation pressure data, potentially leading to inaccuracies, and require high-quality cameras for precise figure extraction. These challenges underscore the need for alternative approaches to enhance the accuracy of WIM systems, considering the limitations of both sensor-based and image-based methods.

7.1 Framework for Weigh-in-motion using Camera Data and GFRP-FBG Sensors Fusion

Figure 7.1 further shows the network of the hybrid WIM system, which combines embedded sensor system utilizing in-pavement GFRP-FBG sensors with computer vision through a camera. The camera captures images of the moving vehicle, with a particular focus on the vehicle's wheels. This enables the system to calculate the distance between the sensor and the wheel loading point, which is crucial for KENPAVE's analysis. KENPAVE software is employed to compute stress factors, aiding in the understanding of pavement behavior under changing loading positions and environmental conditions. These stress factors are influenced by sensor installation depth and distance from the loading point, which plays a significant role in the comprehensive analysis of the wander effect's impact. As the vehicle passes over the installed GFRP-FBG sensor, variations in wavelength occur due to temperature and strain changes. Following temperature compensation via a temperature sensor, the strain induced by the vehicle's passage can be computed after include the HMA parameter to calculate. Then after combine the results through the hybrid WIM system, the weight of vehicle can be determined.

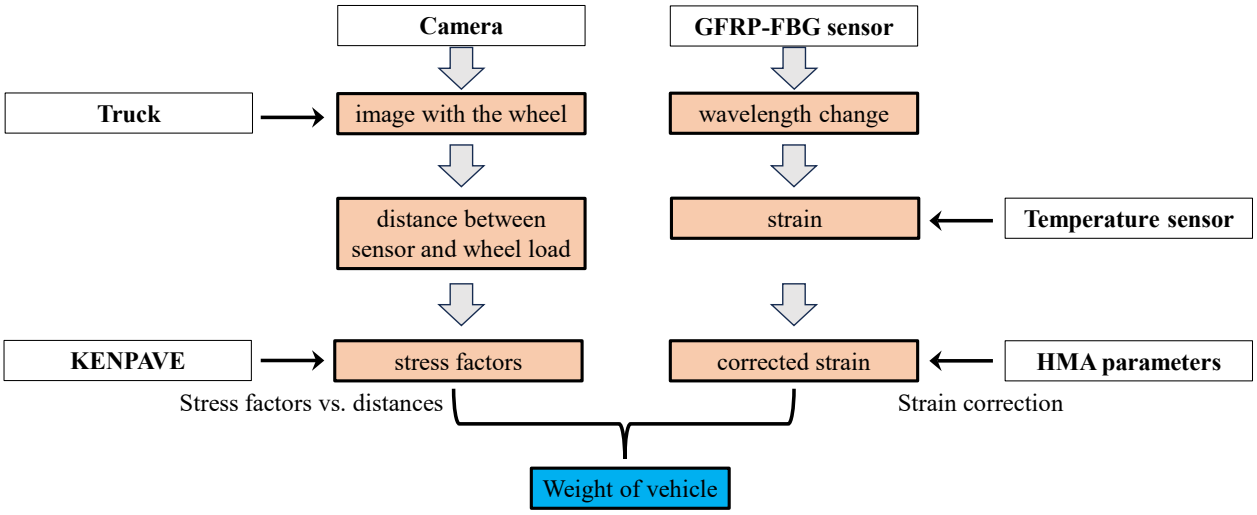

Figure 7.1 Integrated hybrid WIM system for accurate wheel load measurements

7.2 Wheel Load Measurement by GFRP-FBG Sensor

For the objectives of this study, the determination of vehicle weight is predicated on utilization of two GFRP-FBG sensors, either the longitudinal segment of an 3D sensor or an 1D sensor for the determination of vehicle weight, while the temperature sensor (T) is used in temperature compensation. As shown in Figure 2.7, specifically, all sensors can be installed on the right, left, or both side (if enough budget) of the center line within a typical width of the driving lane. FBG-1 needs to be strategically placed above the wheel path, while FBG-2 can be located within a reasonable distance of FBG-1, which is 0.521 m away from FBG-1 as in the example of Figure 2.7 (a). Moreover, FBG-1, FBG-2, and the temperature sensors should be aligned on the same axis. To calibrate the positioning of both the actual elements and the figures, four specific positions are designated in this study. The positions L1 and L3 correspond to placement of the FBG-1 and FBG-2 sensors, respectively. The L2 location is positioned equidistant between L1 and L3 and Location L4 is situated at a certain distance away from L3. Based on layout of the GFRP-FBG sensors, this section details further how to measure wheel load from GFRP-FBG sensors accurately using the hybrid system.

7.2.1 Strain Collection by GFRP-FBG Sensor

For the FBG sensor, a portion of an optical fiber is exposed to an UV laser, and the optical FBG are made by laterally exposing the core of single-mode fiber to a periodic pattern of intense ultraviolet light [90], [139]. The specific wavelength of light (Bragg wavelength) will be reflected by the grating when a broadband incident light is transmitted into the fiber [139]. The Bragg wavelength can expose as [90], [140]:

$$\lambda = 2n\Lambda \tag{46}$$

where n is the effective index of refraction and Λ is the grating periodicity of the FBG.

For the embedded FBG sensors, the measured field interacts with the sensitive optical fiber, causing the wavelength change of the transmitted light in the optical fiber [141], [142]. Once vehicles pass through the GFRP-FBG sensors, the Bragg wavelength changes as a function of temperature and strain, which is dependent on the grating period [90]. The general expression of the strain–temperature relationship for the GFRP-FBG strain sensor and temperature compensation sensor can be described as [140]:

$$\frac{\Delta\lambda}{\lambda} = \frac{\Delta\lambda_{\varepsilon}}{\lambda_{\varepsilon}} + \frac{\Delta\lambda_{T_e}}{\lambda_{T_e}} = (1 - P_e)\varepsilon + (\alpha + \gamma)\Delta T_e \tag{47}$$

$$\frac{\Delta\lambda_{T_e}}{\lambda_{T_e}} = (\alpha + \gamma)\Delta T_e \tag{48}$$

in which λ is the Bragg wavelength of the grating, which experiences strain and temperature changes, and where λ_{T_e} and λ_{ε} is Bragg wavelength of the grating, which only experience temperature and strain change. The $\Delta\lambda_{T_e}$ and $\Delta\lambda_{\varepsilon}$ represents the alteration in Bragg wavelength due to temperature and strain, respectively. α, γ, and P_e are the thermal expansion coefficient, thermal-optics coefficient, and optical elasticity coefficient, respectively. Then, the strain of sensor can be determined as follows:

$$\varepsilon = \frac{1}{(1 - P_e)}\left(\frac{\Delta\lambda}{\lambda} - \frac{\Delta\lambda_{T_e}}{\lambda_{T_e}}\right) \tag{49}$$

7.2.2 Strain Correction based on the Host Material

In addition, for the GFRP-FBG sensor, the optical fiber is covered by the protecting layer (GFRP) and host material (HMA). When the host material is different, the strain transfer error of the GFRP-FBG sensor is also different. Accounting for the impact of the packaging layer between the optical fiber and host material, the relationship between average strain experienced by the GFRP-FBG sensor ($\bar{\varepsilon}_c$) and the actual strain of the host material ($\bar{\varepsilon}_h$) is as follows [143]:

$$\bar{\varepsilon}_h = \frac{\bar{\varepsilon}_c}{1 - \phi} = k\bar{\varepsilon}_c \tag{50}$$

where k is the strain transfer error modification coefficient and ϕ is the measurement error of the packaged GFRP-FBG, which can be computed as [90]:

$$\phi = \left|\frac{\bar{\varepsilon}_c - \bar{\varepsilon}_h}{\bar{\varepsilon}_h}\right| = \left|\frac{cosh(\xi l_f) - 1}{\xi l_f sinh\,(\xi l_f)}\right| \tag{51}$$

where l_f is the gage length of the package GFRP-FBG sensor and the ξ represents the eigen value of its characteristic function, which can be calculated as [143]:

$$\xi^2 = \frac{2}{E_0 {r_0}^2\left(\left(\frac{1}{G_{GFRP}}\right) ln\left(\frac{r_{GFRP}}{r_0}\right) + \left(\frac{1}{G_h}\right) ln\left(\frac{r_h}{r_{GFRP}}\right)\right)} \tag{52}$$

where E_0 and r_0 are the elastic modulus and outer radius of the optical fiber; G_{GFRP} and r_{GFRP} are the shear modulus and outer radius of the protecting layer (GFRP); G_h and r_h is the shear modulus and outer radius of the host material layer.

For different host materials, the shear modulus (G_h) is different, with the dynamic modulus (E) changed. The shear modulus on various temperature and loading frequency was generated using a constant Poisson's ratio (μ) with the following equation [144]:

$$G_h = \frac{E}{2(1+\mu)} \tag{53}$$

The dynamic measurement error is used to correct the strain values generated by the GFRP-FBG sensors based on different temperatures and the loading frequencies, where the temperature is various by seasons, and the loading frequency is influenced by the contact radius of the tire.

For enhanced accuracy in strain values, the dynamic modulus of the material covering the sensor at different temperatures and frequencies is employed to calculate the measurement error between the collected and actual strain values. The dynamic modulus of elasticity and parameters, like the asphalt concrete pavement's thickness and Poisson's ratio for each road layer, are determined through laboratory testing. This data is then fed into the KENPAVE software, which generates the stress factor of the road at various locations and depths. Subsequently, the wheel load can be calculated using Equation 9.

$$F = \frac{\varepsilon_z * E * a}{\alpha_z - v(\alpha_r + \alpha_t)} \tag{54}$$

where ε_z is the vertical strain can be calculated through FBG sensor and temperature sensor, E is the dynamic modulus of elasticity, a is the contact area, v is the Poisson ratio, α_z, α_r, and α_t is the vertical, radial and tangential stress factor.

7.3 Integration of Image-Based Distance Determination and KENPAVE Analysis to Determine the Stress Factor

Given the fixed-sensor position, variations arise in the signal received by the FBG sensor as vehicles with varying wheel loading positions pass. To achieve precise weigh-in-motion data, knowing the wheel-loading positions is paramount. Additionally, accounting for the stress factor based on road parameters and vehicle characteristics becomes crucial in relation to the distance between the wheel loading position and the sensor. Hence, this section introduces methodology for determining wheel-load positions from the figures, featuring the wheels and elucidates the process of calculating the stress factor utilizing the KENPAVE software.

7.3.1 Determining Wheel Load Position using Camera-Captured Figures

Accurately determining the wheel load position is crucial for WIM due to the fixed sensor positions. The signals generated as a vehicle passes over the sensors vary based on the wheel load position. As four positions are identified in this process with two located at the sensor locations (L1 and L3) and the other two adjacent positions. For example, L2 can be situated at a distance of 26 cm from each sensor location, and L4 can be at a distance of 22.9 cm from L3, respectively. These positions are marked by lines as illustrated in Figure 7.2. To ensure safety and avoid direct positioning in front of moving vehicles, the cameras need to be placed right ahead of the vehicle on the roadside.

Despite the camera being properly set up and capturing images with the wheels, an issue arises in accurately determining the precise distance between the wheel loading position and the embedded sensor through image due to visual perspective. Despite distance appearing shorter and the potential for actual distances to remain consistent, this issue persists due to a visual distortion arising from the image's perspective, where objects position farther away seemed compressed, resulting in them appearing shorter even though their true distances remain unaltered. Within this study, the four marked lines (for location L1 to L4), in conjunction with three calibration lines, hold a pivotal role in quantifying the distance between the wheel loading position and the embedded sensor. In scenarios where no vehicles are present, the four marked lines and three calibration lines are shown in Figure 7.2 (a). The known distance between the edge line and the four marked lines traces on the road formed a pivotal aspect in defining the wheel's location. This position is determined through utilization of three calibration lines:

Purple calibration line: White lines usually exist on the side of the highway edge line, which is used as the purple calibration line deliberately positioned consistently above the same spot and is meant to align with the white line. If the purple calibration line fails to align with the white line, it signifies the potential for camera position shifts caused by windy conditions, leading to the possibility of inaccurate determinations of locations.
Red calibration line: The highway edge lines (red line) can be used as another reference as it determines the wheel loading position of trucks in the direction parallel to the edge line.
Yellow calibration line: The lines perpendicular to the highway edge lines (yellow line) can be used to determine the wheel loading position of trucks in the direction vertical to the edge line.

As depicted in Figure 7.2 (a), once the camera positioning is confirmed using the purple line, the lengths of the yellow calibration lines and their corresponding red calibration lines are taken as input variables. These inputs are used to determine the output variable, which represents the actual distance between the edge line and the marked line. The trained model will then be employed to predict the wheel's location, similar to the scenario depicted in Figure 7.2 (b), where the lengths of the yellow and red lines are inputted to determine the wheel's position accurately.

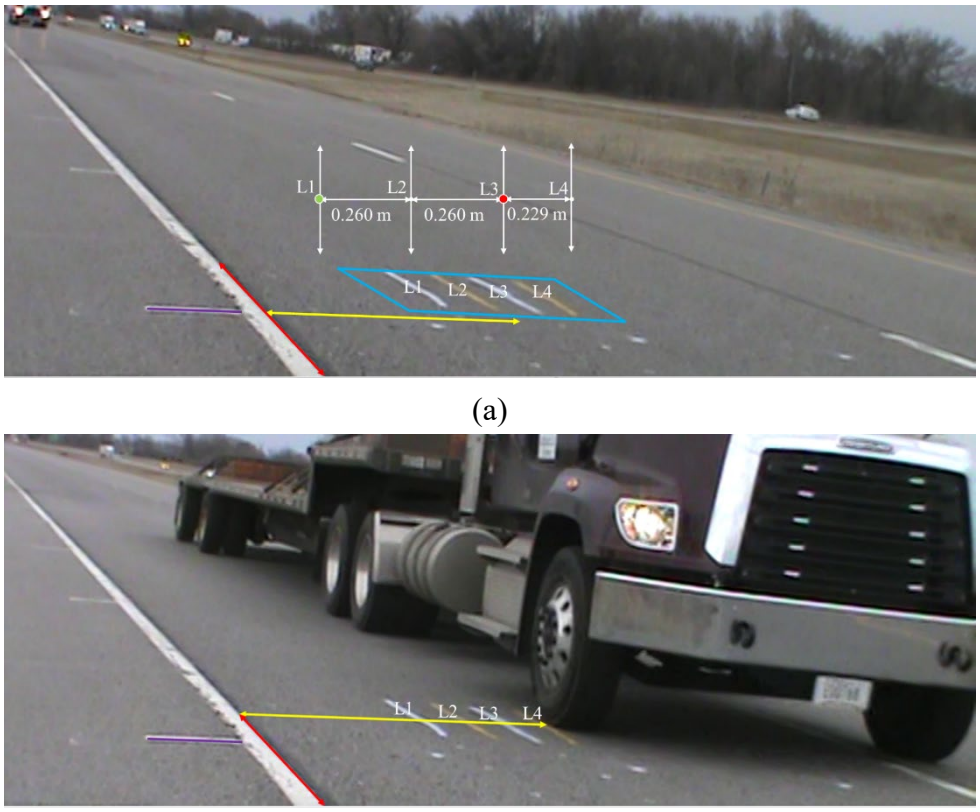

(a)

(b)

Figure 7.2 Accurate wheel load position determination and calibration process (a) calibration area with marked and calibration lines; (b) example of vehicle passing calibration area

7.3.2 Stress Factor Determination using KENPAVE Software

In the field of pavement analysis, when a vehicle's wheels apply pressure to the road surface, resulting deformations manifest at varying depths and positions. Consequently, it becomes essential to determine stress factor at different depths and distances from the loading point (determined by the wheel location in section 2.3.1.), considering elements like contact area, dynamic modulus of the road, temperature, and loading frequency as the vehicle moves along the road.

To address this challenge, the KENPAVE software [145] is employed in this study, offering a solution to the wander effect and providing specialized tools extensively used in civil engineering and pavement analysis. In this study, KENPAVE facilitates the computation of stress factors, crucial for understanding pavement behavior under varying loading position, temperatures, and environmental conditions. Notably, stress factors are influenced by parameters, such as sensor installation depth, distance between the sensor and loading position.

With all the requisite information (including dynamic modulus, Poisson's ratio, and thickness of each road layer at specific temperatures and loading frequencies from the lab) ready for input into KENPAVE, the only missing elements are the contact area and dynamic modulus. Based on the research that compared the real tire contact area (detected by a vehicle driving over paper to record the footprint of the wheel) with the measured contact area by different equations, including rectangular, circular, deflection, and oval

[66], [146], [147], the contact area measured by the oval method generated the lowest average error [66]. The equation to evaluate the contact area based on the oval method is [66]:

$$A = \frac{2}{3} * l * w + \frac{\pi}{3} * \frac{l}{2} * \frac{w}{2} \tag{55}$$

where l and w are length and width of the contact area.

On the other hand, for different pavement road, the dynamic modulus was different, and it is influenced by the temperature and loading frequency. Using dynamic modulus data collected in field and NCAT of the HMA in the field experiments there a dynamic modulus master curve can be developed by shifting twenty-four results gained through testing at different temperature-frequency combi-nations using the following equations [148], [149]:

$$log|E| = \delta + \frac{Max - \delta}{1 + e^{\beta + \gamma * log\omega_r}} \tag{56}$$

where E and Max are dynamic modulus and limiting maximum modulus (6.895 GPa [150]); δ, β, and γ are fitting parameters. The logarithm of the reduced frequency at the reference temperature (ω_r) can be computed based on Arrhenius equation [148], [151]:

$$log\omega_r = log\omega + \frac{\Delta E_a}{19.14714}(\frac{1}{T} - \frac{1}{T_r}) \tag{57}$$

where ω is loading frequency at the test temperature. T_r and T are the reference temperature and test temperature ($^{\circ}$K) with the test temperature determined using the installed temperature sensor situated next to the GFRP-FBG sensor. ΔE_a is activation energy (treated as a fitting parameter).

Assuming the moving load only impacted the sensor within a loading area six times of the contact radius (a) between the tire, the loading frequency can be estimated by vehicle speed divided by the travel length (12 times of the contact radius) [58] as follows:

$$\omega = \frac{v}{12a} \tag{58}$$

Once the contact area and dynamic modulus have been calculated, all necessary input data for the KENPAVE software is available, and the software can then generate stress values and subsequently calculate the stress factor for varying distances between the sensor and the wheel loading position. Considering that sensor positions can differ and even the same vehicle passing by with varying wheel load positions can result in different signals received by the sensor, this study aims to utilize the stress factor produced by the software for calibration purposes. This approach is taken to mitigate the impact of the wandering effect on the accuracy of WIM results.

7.4 Experimental Results and Discussion

The subsequent experimental results and discussion section highlights: 1) Strain values from the same vehicle positioned differently during each drive; 2) A model trained to calculate distances between the wheel loading position and the edge line, aiding in determining the distance between the wheel loading position and the embedded sensor; and 3) Stress factors for varying sensor-wheel distances. Through the

application of strain and stress factors adjusted with distances derived from image analysis, the accuracy of wheel load assessment is evaluated.

7.4.1 Utilizing GFRP-FBG Sensors for Wavelength-based Strain Calculation

Strain calculation was conducted using Equations 2 to 4, with the GFRP-FBG sensors collecting wavelength data and incorporating temperature compensation via a temperature sensor. As a vehicle passed over the sensors, a change in wavelength occurred, illustrated in Figure 7.3 (a). In Figure 7.3 (b), the five wheels corresponded to the wavelength peaks positions. In terms of the wheel location in Figure 7.3 (b), the wheel loading directly above the FBG-1 sensor was farther away from FBG-2. As a result, the wavelength changes and peaks recorded by FBG-1 were larger than those observed by FBG-2, as depicted in Figure 7.3 (a).

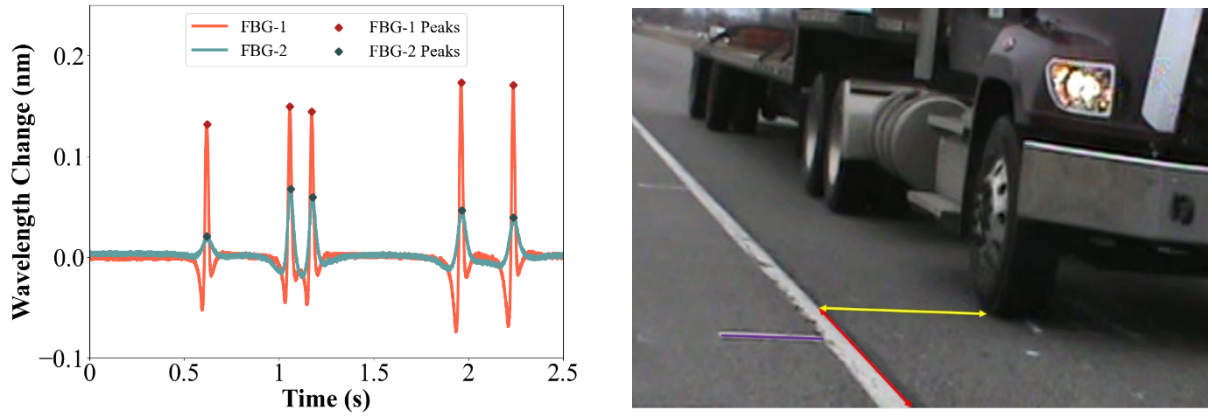

(a) (b)

Figure 7.3 (a) Wavelength change generated by vehicle passage; (b) corresponding wheel loading position for FBG peaks

Given that accuracy in evaluating wheel load is higher when the wheel loading point is in proximity to the sensor, the data from FBG-1 was utilized for cases where the wheel loading point was near FBG-1, and similarly, the data from FBG-2 was employed when the wheel loading point was close to FBG-2. The collected wavelength change data from FBG-1, FBG-2, and the temperature sensor (T) for the 14 vehicle runs and the calculated strain derived from the wavelength change are presented in Table 7.1.

Table 7.1 Wavelength change data and calculated strain for 14 vehicle runs

Vehicle #	Wavelength change (FBG-1)	Wavelength change (T)	Strain (*E-4)	Vehicle #	Wavelength change (FBG-2)	Wavelength change (T)	Strain (*E-4)
1	0.143	-0.002	1.194	8	0.143	0.001	1.186
2	0.132	-0.003	1.111	9	0.153	0.002	1.260
3	0.142	-0.002	1.183	10	0.127	0.000	1.057
4	0.151	-0.001	1.252	11	0.136	-0.002	1.153
5	0.105	-0.001	0.875	12	0.121	0.001	0.988
6	0.113	-0.002	0.951	13	0.126	-0.001	1.055
7	0.112	-0.001	0.931	14	0.082	-0.002	0.696

*unit of wavelength is nm.

7.4.2 Calibration Line Utilization and Modeling for Distance Calculation

With the purple calibration line consistently employed for determining the camera's location, the four distinctive marked lines at locations L1, L2, L3, and L4 each used the same red calibration line, along with 15 yellow calibration lines (as shown in Figure 7.4), which differed for each location. The lengths of the red and yellow calibration lines, measured in meters, are presented in Table 7.2.

These measurements were employed to train a linear regression model as shown in Equation 14 — a fitted equation for calculating the distance from the edge line to the wheel location when inputting lengths of the red (l_r) and yellow calibration lines (l_y). The model's R-squared value and standard error is 0.9989 and 0.3668, when the confidence interval is set at 95%, indicating a good fit to the actual data.

$$distance = -32.307 + 5.148 * l_r + 7.203\, l_y \quad (59)$$

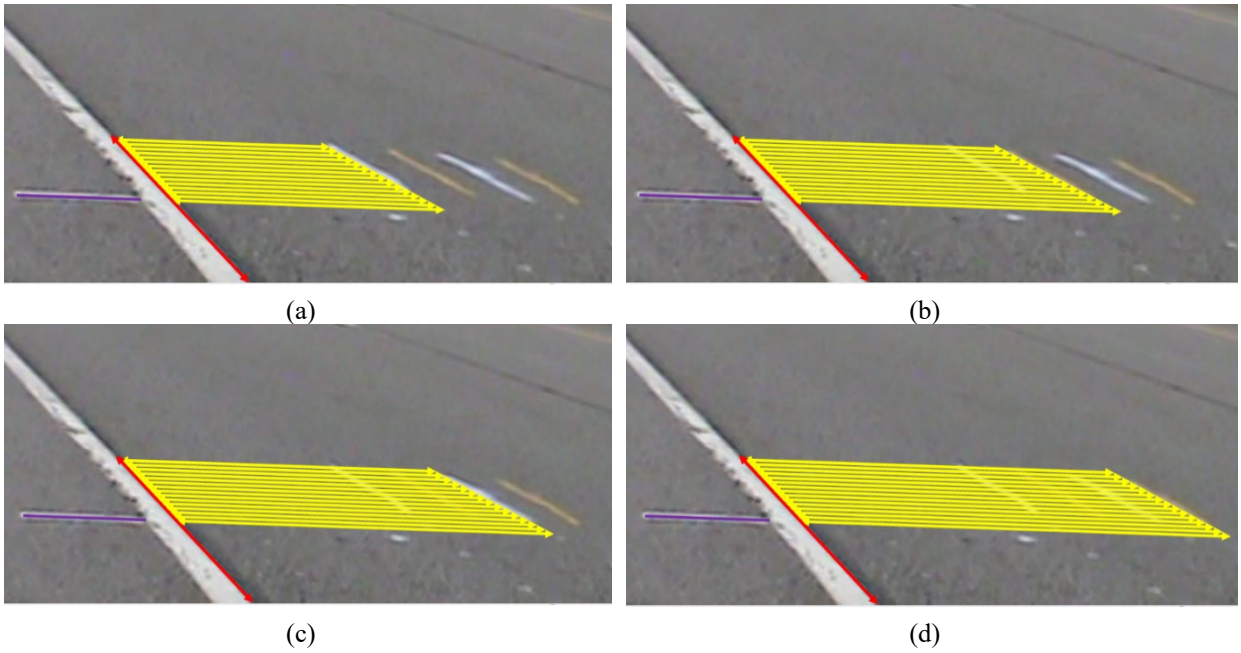

(a) (b) (c) (d)

Figure 7.4 Calibration lines for location (a) L1; (b) L2; (c) L3; (d) L4

Table 7.2 Length of the red and yellow calibration lines used to train the distance model

Number	Red calibration line	Yellow calibration line (L1)	Yellow calibration line (L2)	Yellow calibration line (L3)	Yellow calibration line (L4)
1	0.030	0.114	0.102	0.089	0.073
2	0.032	0.113	0.100	0.087	0.072
3	0.033	0.112	0.099	0.086	0.071
4	0.035	0.111	0.098	0.085	0.069
5	0.037	0.110	0.097	0.084	0.068
6	0.038	0.109	0.096	0.083	0.067
7	0.040	0.108	0.095	0.082	0.066
8	0.041	0.106	0.093	0.080	0.065
9	0.043	0.105	0.092	0.079	0.064
10	0.045	0.104	0.091	0.078	0.063
11	0.046	0.103	0.090	0.077	0.062
12	0.048	0.102	0.089	0.076	0.061
13	0.049	0.101	0.087	0.074	0.060
14	0.051	0.100	0.086	0.073	0.059
15	0.052	0.099	0.085	0.072	0.058

*unit is m.

The identical vehicle was intentionally driven over the sensors a total of 14 times, with seven of these passes deliberately executed near location 1 (FBG-1), and the remaining seven near location 2 (FBG-2). Subsequently, the lengths of the red and yellow calibration lines corresponding to the 14 vehicle runs were incorporated as input for the previously trained model. This model served to estimate the distance from the edge line to the wheel loading position. It's important to clarify that the designated wheel loading position pertains to the right side of the wheel, not the midpoint, which signifies the actual wheel loading location. To rectify this discrepancy, the revised distance was corrected by adding half of the wheel width, equivalent to 0.103 meters. Both the model-derived distances and the adjusted measurements are presented in Table 7.3 for comparison. In this table, a plus sign (+) indicates that the wheel loading point resided on the sensor side closer to the centerline, while a minus sign (-) denotes that the wheel loading point was situated on the sensor side nearer to the edge line. The sequence of vehicles was based on the absolute value of the revised distance derived from the FBG-1 and FBG-2 sensors.

Table 7.3 Model-derived and adjusted wheel loading distances for 14 vehicle runs

Vehicle #	Distance (FBG-1)	Revised Distance (FBG-1)	Vehicle #	Distance (FBG-2)	Revised Distance (FBG-2)
1	-0.125	-0.022	8	-0.101	0.002
2	-0.159	-0.056	9	-0.084	0.019
3	-0.176	-0.073	10	-0.053	0.050
4	-0.192	-0.089	11	-0.040	0.064
5	0.011	0.114	12	-0.033	0.070
6	-0.232	-0.129	13	-0.205	-0.102
7	0.027	0.131	14	-0.212	-0.109

*unit of distance is m.

7.4.3 Stress Analysis with KENPAVE Software in Pavement Structures

The KENPAVE software [145], taking into account various input parameters, including the number of pavement layers, the depth of the GFRP-FBG sensor, layer moduli, individual layer thickness, Poisson's ratio, contact radial, and contact pressure, was employed for stress analysis. Notably, while the software mandates the input of contact pressure, this study did not delve into its determination process. This is because the input value of the contact pressure did not influence the outcome; it was solely used to calculate the stress factor from the software's stress output. Regardless of the heightened stress output resulting from increased input values of the contact pressure, the stress factor, obtained by dividing stress by the contact pressure, remained constant when other input information remained unaltered.

To obtain the contact radius, tire information is essential. For this study, the tire specification was 275/80 R 22.5, where 275 represents the tire width in millimeters, 80 was the aspect ratio and equal to sidewall height divided by section width, "R" was for radial tires, and 22.5 was the rim diameter in inches (57.2 cm). A contact width of 75% of the tire section width is for optimum performance, as suggested by typical design criteria. [152] Therefore, for this tire, the contact width was 0.206 m, with the assumption that the contact width was 60% of the contact length [145], the contact length was 0.344 m. And based on Equation 10, the contact area was 0.066 m^2. With the software defining the contact area as a circle, the input contact radius was 0.145 m.

The pavement information, as shown in Table 7.4 [87], [145], the contact pressure, and contact radius of the one wheel were input to the software KENPAVE to generate the stress, when the distance between the center of the contact area and the sensor (installed 0.127 m under the road) was from 0 to 1.168 m. The software generated a comprehensive array of outputs, including vertical, radial, tangential, shear stress, and vertical displacement data, covering a radial coordinate range from 0 to 116.8 m. This research employed the vertical, radial, and tangential stress relative to weight to derive vertical, radial, and tangential factors (as depicted in Figure 7.5). Subsequently, these factors contributed to the utilization of Equation 9 for the determination of vehicle weight.

Table 7.4 Parameters input to the software KENPAVE

Layer	Thickness (m)	Poisson's Ratio	Dynamic modulus (GPa)
HMA	0.127	0.35	4.826
granular base	0.305	0.35	0.414
sub-base clay loam	0.305	0.35	0.276
granular	0.178	0.4	0.083
clay loam	0.089	0.4	0.083

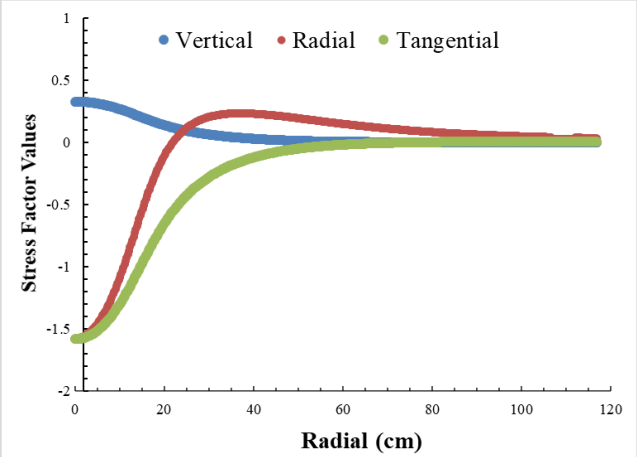

Figure 7.5 Vertical, longitudinal, tangential stress factors

7.4.4 Accuracy Assessment of Vehicle Load Monitoring

Having acquired the strain, distances between the sensors and wheel loading position, and the fitted stress factor to these distances, the calculation of the wheel load for the first right single wheel became feasible. Considering the same vehicle positioned differently during each drive, Table 7.5 provides the computed distances between the wheel and the sensor, calculated weight, and accuracy. The weight of the first right single wheel was assumed to be one-half of the weight of the first axle, which totals 26,022 N. This value was utilized as the actual weight of the first right single wheel for accuracy assessments. Generally, accuracy is closely linked to the distance between the wheel loading point and the sensors. For the FBG-1 sensor, the average accuracy reached 87.831% when the absolute distance from the FBG sensor to the wheel loading point was less than 0.089 meters, decreasing to 84.206% when the distance fell below 0.131 meters. Meanwhile, the FBG-2 sensor achieved an average accuracy of 94.645% when the sensor-to-wheel loading point distance was less than 0.070 meters. When the distance is less than 0.109 meters, the FBG-2 sensor will maintain an average accuracy of 91.027%. Figure 7.6 illustrates the alteration in vehicle measurement accuracy in response to changes in the distance between the two embedded GFRP-FBG sensors and the wheel loading position. As the distance between the sensors and the wheel loading position increases, there is a noticeable and consistent reduction in measurement accuracy. This observation underscores the importance of maintaining relatively close proximity between the sensors and the wheel loading point for optimal accuracy in vehicle weight measurement. Therefore, it is recommended to install the GFRP-FBG sensors approximately every 0.09 meters and 0.07 meters to achieve around 85% and 95% accuracy, respectively. Considering the significance of both driving speed and the distance between the wheel loading point and the FBG sensor, it's worth noting that this study primarily focuses on analyzing the distance's impact on the results. This choice is driven by the practical challenge of controlling heavy trucks to drive at the same speed and the same location. To validate the influence of speed on the measurement results, it's imperative to conduct additional runs with consistent

speeds and controlled wheel loading positions. Further analysis of speed's impact on measurement accuracy will be incorporated in future research.

Table 7.5 Vehicle load accuracy based on dynamic modulus of elasticity, KENPAVE stress factors, and GFRP-FBG strain evaluation

Vehicle #	Revised Distance (FBG-1)	Weight (FBG-1)	Accuracy (%)	Vehicle #	Revised Distance (FBG-2)	Weight (FBG-2)	Accuracy (%)
1	-0.022	26750.916	97.199	8	0.002	26275.504	99.026
2	-0.056	26429.119	98.435	9	0.019	28168.385	91.752
3	-0.073	29826.825	85.378	10	0.050	24817.696	95.372
4	-0.089	33747.883	70.310	11	0.064	28061.367	92.163
5	0.114	27505.864	94.298	12	0.070	24698.723	94.915
6	-0.129	32990.593	73.220	13	-0.102	30495.575	82.808
7	0.131	33672.318	70.601	14	-0.109	21117.985	81.154

*unit of the distance and weight is m and N.

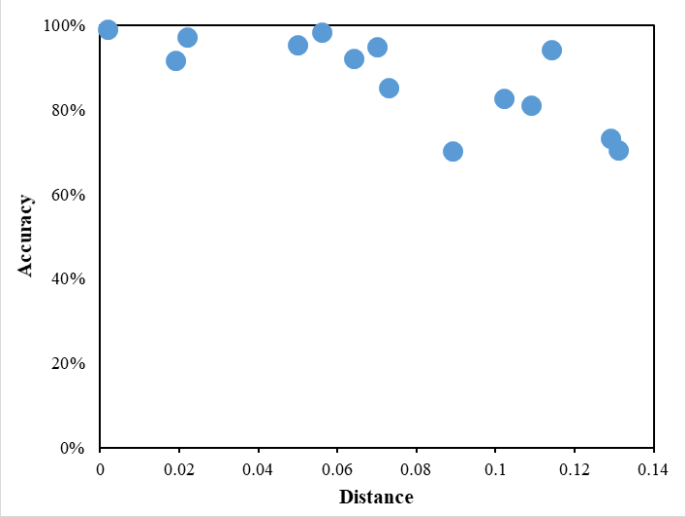

Figure 7.6 Vehicle measurement accuracy vs distance between the embedded sensor and wheel loading position.

7.5 Summary of Mitigating Vehicle Wandering Effect with In-Pavement Sensor-Camera Hybrid System

This study proposes an in-pavement sensor-camera hybrid system for wheel load detection on highway to assess the wandering effect of vehicle on the accuracy of WIM systems based on GFRP-FBG sensors. The hybrid system effectively addressed key challenges in WIM systems using either only FBG sensors or computer vision, including the lack of comprehensive research on the influence of vehicle wandering on WIM accuracy and the persistent difficulties in achieving accurate contact pressure assessment for vehicles using computer vision techniques. By integrating the spatial information from the computer vision with strain assessments from GFRP-FBG sensors, an effective calibration approach was employed in this study to mitigate the wandering effect and enhance the accuracy of the WIM system based on FBG sensors. Key findings and conclusions from the study can be summarized as below:

Applying calibration line to generate model for distance prediction: This study employed distinct marked lines (L1, L2, L3, and L4) to develop a linear regression model accurately estimating the distance from the edge line to the wheel loading position. This model's reliability is supported by a strong R-squared value of 0.9989 when the confidence interval is set at 95%, providing a solid basis for precise distance calculations.

Investigation of the wander effect: Given the fixed position of the sensor and the significant impact of varying wheel loading positions on the collected signals, this study accounted for the wandering effect using KENPAVE software. The outputs encompassed vertical, radial, and tangential stress, covering a sensor-wheel loading distance range of 0 to 116.8 meters. Vertical, radial, and tangential factors were derived relative to weight, contributing to the determination of vehicle weight.

High-accuracy WIM measurement: Highly accurate measurement was achieved by taking account factors such as the GFRP-FBG sensor assessed strain, distance between the sensor and wheel loading position, and KENPAVE software-derived stress factors. Accuracy is closely tied to the proximity of the wheel loading point to sensors. FBG-1 achieves an average accuracy of 87.831% for distances under 0.089 meters, decreasing to 84.206% when the distance less than 0.131 meters. In contrast, FBG-2 achieves 94.645% accuracy for distances less than 0.070 meters and maintains 91.027% accuracy for distances under 0.109 meters.

In conclusion, this study effectively validated applicability of the proposed sensor-camera hybrid system for assessing single-wheel loads while the vehicle is in motion. Through a combination of using high-sensitive, strong, and durable GFRP-FBG sensors, precise calibration methods, and advanced software analyses, this study provides valuable insights into weight evaluation techniques, particularly accounting for the wandering effect. The sensor-camera hybrid system's innovative approach, which addresses the wandering effect, improves weight measurements for moving vehicles. This enhanced accuracy has practical applications in transportation infrastructure maintenance, traffic management, environmental impact assessment, pavement design, and research and development, contributing to safer roads and more efficient transportation systems. While this study primarily focuses on analyzing the distance's impact on results due to practical challenges in controlling speed and location, it acknowledges the limitation of not fully exploring the impact of speed, truck load types and configuration, and installation layers within the pavement. Future research will address this limitation by conducting additional runs with controlled conditions to evaluate speed's influence on measurement accuracy. Furthermore, while the study effectively evaluated single-wheel weights using the proposed methodology, future research avenues will include dual-wheel weight assessments. Analyzing load distribution and strain patterns in dual-wheel configurations could enhance our understanding of multi-axle vehicle behavior and its impact on pavement integrity, providing essential insights for both research and practical transportation scenarios.

8. HYBRID WIM SYSTEM WITH COMPUTER VISION & IN-PAVEMENT SENSORS

In 2022, the United States recorded 283.4 million vehicles, with light trucks accounting for 10.9 million units sold during that year [153]. The growing number of vehicles, particularly trucks, can lead to accelerated wear and increased structural stress on road infrastructure. This increased demand poses additional challenges for road maintenance, impacting the long-term integrity of the roadway system. Hence, efficient road maintenance is vital for ensuring safe, sustainable, and economically viable transportation infrastructure, minimizing repair costs, enhancing road safety, and facilitating reliable traffic flow. Road maintenance is significantly influenced by factors such as vehicle traffic volume, diverse vehicle types, and varying weights, all contributing to the degradation of road infrastructure. Of particular concern is the impact of heavy trucks, whose substantial weight and associated stresses pose significant challenges, accelerating the deterioration of roads.

Two commonly used methods for obtaining vehicle weight are static weigh stations and weigh-in-motion (WIM) stations. Static weigh stations offer high accuracy but have drawbacks as they influence traffic and may pose safety concerns. These stations are often situated next to highways, requiring vehicles to come to a complete stop or driving at a very low speed for weight measurement, resulting in significant time delays [5]. This becomes especially problematic when the volume of vehicles is high, and the capacity of static weigh station is insufficient to survey all passing heavy commercial vehicles. In contrast, WIM stations offer benefits by providing real-time vehicle weight without disrupting them. However, concerns arise regarding the accuracy of vehicle weight measurements. Various factors can influence WIM accuracy, including driving speed, weather conditions, pavement temperature, and road roughness [154], [155], [156], [157]. Following the ASTM 1318E-09 standard, recognized as the primary WIM standard in the United States, it outlines performance requirements for WIM systems categorized as type I, II, and III. The standard specifies axle load accuracy tolerances of $\pm$ 20%, $\pm$ 30%, and $\pm$ 15% for type I, II, and III systems [139]. Type I and II systems, characterized by lower accuracy, are well-suited for traffic data collection with slight variations in performance requirements. In contrast, Type III systems are optimal for screening vehicles suspected of weight or load limit violations, pre-selecting them for static weigh stations [139]. Therefore, the integration of a highly accurate WIM system holds the potential for substantial benefits in enhancing efficiency and safety in vehicle weight monitoring processes.

There are two primary data acquisition methods to perform WIM measurements including embedded sensor systems and image capture systems [158]. The embedded sensor system, also known as in-pavement sensor system, integrates a data acquisition system with in-pavement sensors placed beneath the road, such as bending plates, load cell plates, polymer piezoelectric sensors, quartz piezoelectric sensors, and strain gauge strip sensors [139]. However, electrical sensors in this system face challenges such as environmental susceptibility, electromagnetic interference, limited lifespans, and moderate measurement errors [58]. Fiber Bragg grating (FBG) technology emerges as a promising alternative for WIM, offering immunity to electromagnetic radiation, non-conductive nature, lightweight design, spark-free operation, intrinsic safety, high sensitivity to strain, and compatibility with structural elements [59]. Therefore, FBG sensors are widely used in research applications like structural health monitoring [60], [61], [62]. For asphalt pavement monitoring, researchers utilize FBG sensors to assess the performance of multilayered asphalt pavement [159]. However, given that WIM necessitates installing sensors beneath the pavement road, it is crucial to employ protective packaging to safeguard them against damage during installation and throughout their service life. The materials commonly employed for sensor packaging encompass fiber reinforced polymer (FRP) options like glass fiber reinforced polymer (GFRP) [160], polypropylene sleeves [161], and silicone tubes [162]. In addressing the demanding sensor service environment (under highway pavement), the packaging structure must fulfill several requirements,

including a substantial measurement range, strength, construction ease, durability, long-term stability, fatigue resistance, and resistance to elevated temperatures [58], [64], [90]. Therefore, GFRP has been proved effective for packaging FBG sensors. Nevertheless, an unavoidable challenge in employing in-pavement sensors for WIM measurements is the wander effect. Given that most of the in-pavement sensors operate as point or local sensors in WIM, their precision is significantly affected by the wander effect, arising from misalignment with actual wheel positions [61]. This mismatch, stemming from static sensor placement, introduces inaccuracies and uncertainties in weight measurements [57].

Another popular approach in WIM systems is the use of road-side image-capturing systems, eliminating the need for installing sensors beneath the road. Feng et al. [65] introduced a novel methodology using computer vision to analyze moving vehicle images, extracting tire deformation parameters and calculating vehicle weight based on tire information [65]. They estimated the vertical deflection of tires using computer vision for three fully-loaded concrete trucks and four empty concrete trucks, resulting in average errors of 2.36% and 4.85%, respectively. Kong et al. [66] employed computer vision techniques for non-contact WIM solutions. They evaluated the proposed method on SUVs and trucks under various conditions, showing robust performance with a maximum error in vehicle weight identification below 10%. While advantageous in eliminating the need for in-pavement sensor installation, these studies rely on manufacturer-provided inflation pressure [71], potentially introducing inaccuracies due to variations in tire conditions [67], [68], [69], [70]. This limitation is particularly significant for trucks carrying heavy loads, where actual contact pressure may deviate from recommended values. Although researchers attempt to include tire deformation to mitigate this influence on accuracy, it still relies on statistical estimation.

Consequently, the WIM system with only embedded in-pavement sensors or image-capturing has limitations. Embedded sensors may have the wander effect issue, and image-capturing struggles with precise inflation pressure. Despite challenges, embedded sensors offer real-time weight calculations, while image-capturing excels in capturing detailed vehicle information. Hence, the authors' earlier research [158] introduced a system that integrates embedded in-pavement strain sensors and image-capturing systems, yielding promising outcomes. A hybrid system integrating image-capturing systems with embedded sensors, which accurately determined the location of the wheel passing over the area of the embedded sensors, offered a more comprehensive solution. Prior research solely relied on image-capturing systems to obtain figures, requiring manual intervention using hands and eyes to identify vehicle wheels. The process also involved using a generated model to predict the distance between the wheel loading position and the wheel to address the wander effect. This approach proved time-consuming and demanded extensive human involvement.

Even though extensive studies have been conducted on WIM, there are still research gaps, which include the following:

The in-pavement sensor systems for WIM measurements faces an inherent challenge known as the wander effect. These sensors, typically operating as point or local sensors, are significantly impacted by misalignment with actual wheel positions, resulting in inaccuracies and uncertainties in weight measurements.

Image-capturing systems obviate the need for in-pavement sensor installation but depend on manufacturer-provided tire inflation pressure data, potentially leading to inaccuracies due to tire condition variations. Moreover, this approach necessitates high-quality cameras for precise figure extraction. Research explored a hybrid system, involving manual identification of vehicle wheels and predicting distances to address the wander effect. This approach required extensive human involvement.

Therefore, this paper explores a hybrid WIM system that integrates computer vision and in-pavement sensors automatically, designed for efficiency with minimal human input and exhibiting considerable potential for real-time vehicle weight detection. This system is cost-effective, utilizing a limited number of sensors and one low-cost camera. Additionally, the study minimizes traffic disruption by automatically calibrating the camera to ensure high accuracy even in adverse weather conditions. Utilizing the developed hybrid system, there was a substantial enhancement in the accuracy of WIM measurements employing in-pavement strain sensors. This improvement enabled the application of cost-effective WIM systems compliant with the ASTM 1318E-09 standard. Its implications extend to areas such as transportation, road maintenance, and ensuring compliance with weight regulations, presenting valuable contributions to both research and industry.

This paper used the GFRP packaged FBG sensors as the in-pavement strain sensors to demonstrate the effectiveness of the hybrid system. The GFRP-FBG sensors were chosen due to their high sensitivity to strains, high survival rate and little lead time during installation, less requirement in maintenance, long life cycle, and immunity to electromagnetic field. A camera was installed on the roadside where the in-pavement sensors were installed for the needs of computer vision to address vehicle wander effect of in-pavement strain sensors. Specifically, the primary role of computer vision is to determine the wheel's location, enabling the calculation of the distance between the GFRP-FBG sensor and the wheel loading position. This section introduces how these two technologies were integrated to determine the vehicle's weight, providing details about the contribution of each technology in WIM measurement.

8.1 Framework of The Hybrid System

The working principle of the proposed hybrid WIM system, as shown in Figure 8.1, involves two sections employing both cameras and in-pavement sensors to acquire vehicle weight. The left side shows the computer vision procedure that processes the images captured by the camera to detect the position of wheels in the vehicle. To accurately determine the distance between the wheel loading position and the in-pavement sensor, calibration lines, which were marked on the pavement, were utilized. Distances between each calibration line were recorded for image distance calibration, ensuring accurate real-distance measurements using computer vision. Additionally, the software KENPAVE was employed to determine stress factors for vehicles at different distances between the in-pavement sensor and the wheel loading position. The stress factor in pavement engineering is employed to quantify the distribution of stress within pavement layers, which influenced by various factors such as traffic loads, material properties, and environmental conditions. This factor is important in the assessment of pavement performance and the design of durable roadway infrastructure.

On the right side, highlighted in the green box, the procedure of using in-pavement sensors (GFRP-FBG sensors) to determine strain is illustrated. The wavelength changes collected by the embedded sensor, along with temperature data from a temperature sensor, were used to calculate strain caused by the wheel load. This strain was then corrected based on hot mix asphalt (HMA) parameters. The corrected strain, along with stress factors, was used to derive the vehicle's weight.

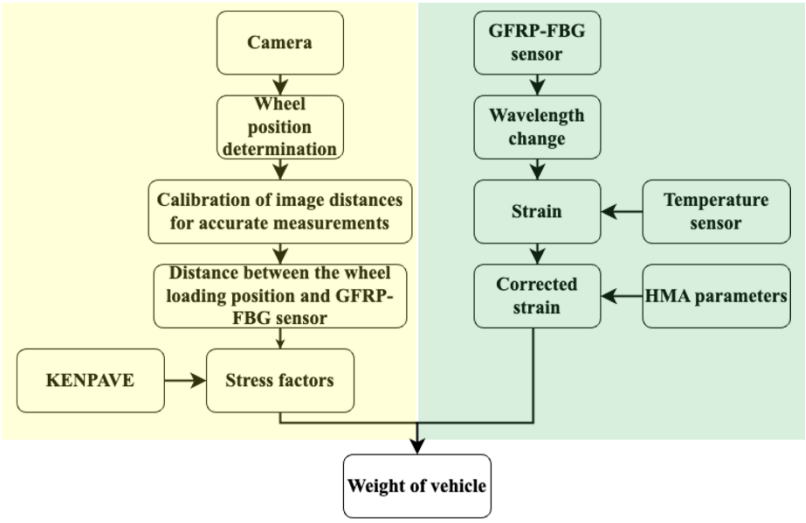

Figure 8.1 Hybrid weigh-in-motion system layout: integrating computer vision and in-pavement sensors

8.1.1 Distance Measurement Between Wheel Loading Position and In-pavement Sensor through Computer Vision

Given the fixed placement of embedded in-pavement strain sensors beneath the road, variations in the distance between the sensor and the wheel loading position result in differences in the calculated strain. Therefore, it is crucial to pinpoint the exact position where the vehicle's wheel passes through. To address this, computer vision was employed in this section to detect the wheel's position and measure the distance between the wheel's loading position and the sensor location.

Wheel Position Determination

To ascertain the distance between the wheel loading position and the sensor, it is essential to determine the wheel's position. This is crucial as the sensor location remains fixed beneath the pavement. This paper utilized images captured by a roadside camera to photograph vehicles as they pass through, with a specific focus on extracting information related to the vehicle's wheels. Given the use of a normal camera in this study, the aim is to achieve the process of obtaining wheel-related data without the need for sophisticated and costly equipment. Nonetheless, challenges arise in accurately determining the wheel's position, prompting the development of necessary processes for adjusting the figures to enhance accessibility.

The image captured by the camera positioned on the roadside is depicted in Figure 8.2(a). Given the varying light conditions throughout the day and across seasons, determining the wheel's position becomes challenging, particularly in low-light situations. Consequently, adjustments were made to the brightness of the image containing the vehicle to enhance clarity, as shown in Figure 8.2(b). Also, to accurately determine the wheel's position in this study, it is crucial to identify its edges. Therefore, the investigation contemplated employing Gaussian blur to diminish noise and enhance the clarity of the edges [163], [164] as shown in Figure 8.2(b). Further enhancing image analysis capabilities, the conversion to the HSV (Hue, Saturation, Value) color space is pivotal for tasks where color information is paramount [Figure 8.2(c)]. Unlike RGB (Red, Green, Blue), HSV's separation of color components facilitates a more intuitive analysis [165], [166]. This conversion significantly streamlines the extraction of color-specific features, contributing to precise and efficient image analysis.

Wheel edge detection was then performed in the modified images; the initial step involved recognizing and highlighting the black sections, as shown in Figure 8.2(d). Recognizing that black sections on the image may not exclusively represent the wheel, all regions containing black were identified using contours. To improve result precision, smaller contours were filtered out, considering the size of the wheel [Figure 8.2(e)]. The method allows for facilitating precise localization of the wheel by isolating relevant areas that represent the wheel's distinctive features, thereby enhancing accuracy in position determination.

An additional filter becomes necessary as all wheels in the figure are initially included. Given the study's objective of determining the distance between the wheel loading position and the sensor, it is crucial to capture the wheel's edge when it approaches the sensor. Thus, the analysis focused on discerning the wheel and its position when it enters the sensor's proximity. This targeted approach assisted in identifying the contour corresponding to the wheel, leveraging the fixed position of the red square area in Figure 8.2(f) near the sensors for precise differentiation.

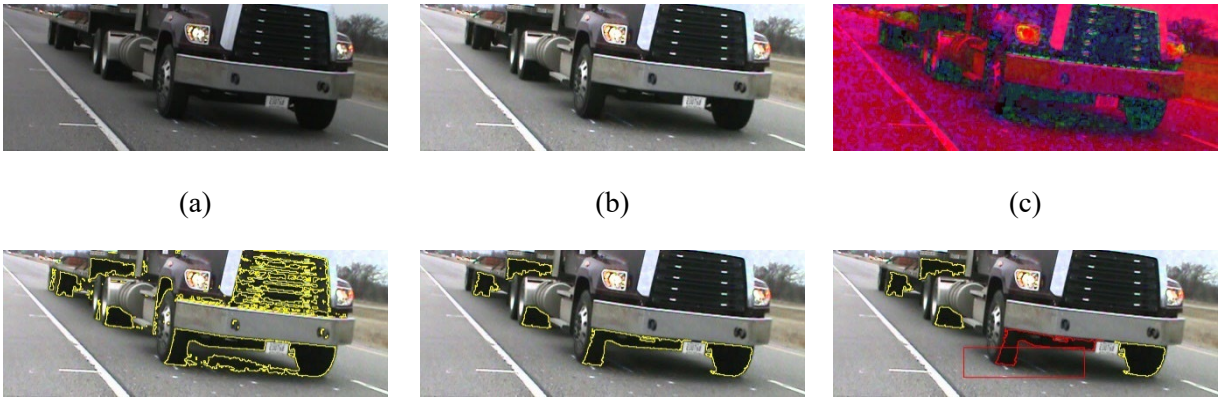

Figure 8.2 Wheel identification through image analysis: (a) image captured roadside; (b) brightness adjustment and Gaussian blur for edge delineation; (c) conversion to HSV color space; (d) black mask and contour for wheel location; (e) filtering out smaller contours; (f) targeted approach with red square near sensors for precise differentiation

Distance Calibration for Accurate Image Evaluation

Upon identifying the edge of the wheel near the sensor, it becomes imperative to undertake calibration for accurate distance evaluation. Given that the camera is positioned on the roadside rather than the front for security and ease of installation without disrupting traffic, the conventional method of determining distance in pixels and converting it to real distance cannot be directly applied to the captured images. This is due to the perspective distortion—objects appearing larger when close to the camera and smaller when farther away—which, if disregarded, would compromise the accuracy of distance determination between the sensor and the wheel. Consequently, this study explores the application of calibration lines to adjust distances based on the varying proximity of objects in the images.

The four calibration lines were used in this study prior to the field test: two positioned just above the two sensors, marked in the same color (white); and two more located in the middle of the two sensors and next to the sensor closest to the centerline, both marked in the distinct color yellow. The measured distances between each pair of calibration lines are carefully assessed and utilized for calibration purposes. The images were taken at an angle of 45 degrees between the camera and the calibration lines, and the

distance from the camera to the white calibration lines, which are closest to the edge line, is approximately 4 meters. These images of the calibration lines were captured when no vehicle was over them. Similar processes involving Gaussian blur and HSV applied to the image were employed to determine the position of the wheel. Masks, which are binary images that highlight specific areas while hiding others, were used to isolate the calibration lines. Yellow and white masks are defined for the calibration lines, and contours for these lines are identified within the defined area, encompassing the sensors and the paved road with the calibration lines, as indicated by the red rectangular area in Figure 8.3(a). The contours of the calibration lines are easily identified, considering they were painted with a width of 0.06 meters. However, for calibration purposes, it is crucial to find the midpoint of the width of the lines and apply the actual distance between them for accurate adjustment. Therefore, this study used the middle of the width of the lines to represent the calibration lines, as shown in Figure 8.3(b).

Given that the four calibration lines run parallel to each other and are perpendicular to the width of the wheel, each line was divided into multiple points with consistent distances between them. Figure 8.3(c) depicts the subdividing of the calibration lines into 50 points, and in Figure 8.3(d), 50 parallel lines (in red) were generated based on the subdivision points. These parallel lines were subsequently used to determine the position of the wheel's center and aided in determining the distance between the sensor and the wheel in the following sections. For better clarity, Figures 8.3 (e) and (f) present the subdivision of calibration lines into 5 points and parallel lines as a demonstration.

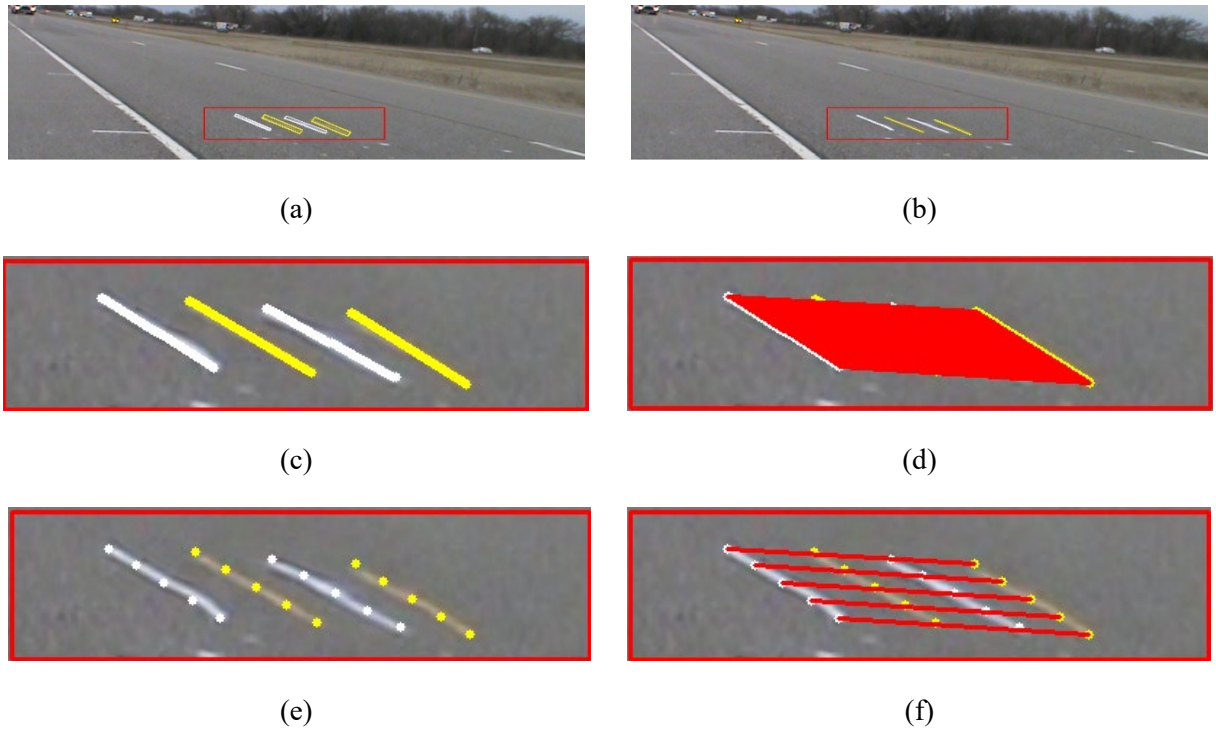

Figure 8.3 Image processing and calibration: (a) capturing calibration lines and defining contours; (b) calibration using line width midpoint; (c) subdividing calibration lines into 50 points; (d) establishing 50 parallels lines; (e) subdividing calibration lines into 5 points; (f) establishing 5 parallels lines

Determining the Distance between In-pavement Sensor and Wheel Loading Position

After obtaining the parallel lines in Figure 8.3, these lines were used to determine the loading position of the wheel, which is crucial for accurately establishing the distance between the sensor and the wheel. Given the non-smooth edge of the wheel, obtaining the line representing the wheel and road becomes challenging.

Utilizing the identified wheel contour from Figure 8.2(f) and the parallel lines in Figure 8.3(d), the blue line represents the parallel line closest to the bottom of the wheel; and this line was used to identify a point (highlighted in green) with a 5-pixel tolerance, as shown in Figure 8.4(a). These green points were then used to determine a line representing the connection between the wheel and the road, which in turn determines the width of the vehicles for calculating the contact area in the subsequent process. In addition, this line allowed for establishing the middle point of the line to represent the wheel's center (wheel loading position). Once the wheel loading position was obtained, parallel lines were employed to determine the distance between the sensor and the lines. As depicted in Figure 8.4(b), the line (in black) closest to the wheel's center (green point) was determined and generated. With knowledge of the pixel distances between the green and red points on both sides and the actual distance between them, the distance between the sensor and the center of the wheel can be accurately determined.

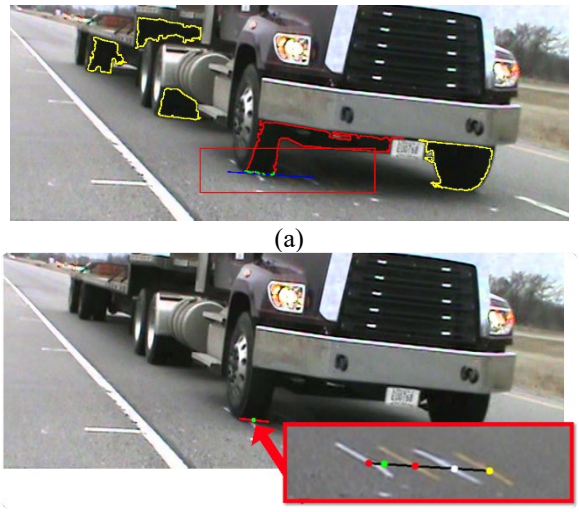

(a) (b)

Figure 8.4 (a) Identification of wheel position using nearest parallel line; (b) locating the bottom parallel line closest to the wheel in blue and highlighting points on the closest parallel lines and calibration lines with red markings

Except for the condition depicted in Figure 8.4(b), where the wheel's center is located between the first white (W1) and yellow (Y1) lines, three additional conditions are considered, as illustrated in Figure 8.5. These include to the left of W1, between the first yellow (Y1) and second white (W2) calibration lines, and between the second white and yellow lines (Y2). The condition next to Y2 is excluded, as the left wheel of the vehicle will not traverse that area unless turning into another lane. The evaluation process is outlined in Figure 8.6 through pseudocode, with input parameters including the position of the closest two points (P_M), sorted based on their x-values to ensure the first point is on the left side of the second point. The position of the center of the wheel is represented as P_{CW}. Points on the closest parallel line and lines W1, Y1, W2, and Y2 are denoted as P_{W1}, P_{Y1}, P_{W2}, and P_{Y2}. The pixel distance from P_{CW} to the closest two points (P_{DM}) is sorted from large to small. Real distances between W1 and Y1 ($RD_{W1,Y1}$), Y1 and W2 ($RD_{Y1,W2}$), and W2 and Y2 ($RD_{Y2,W2}$) are defined. The maximum pixel distance between W1 and Y1 is denoted as $MP_{W1,Y1}$. The output is the distance between the center of the wheel and the sensor (D_{CW_S}).

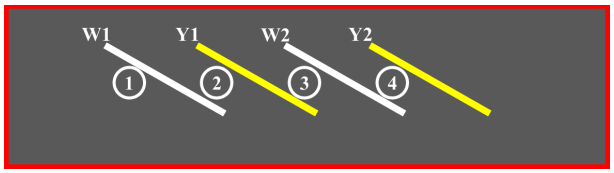

Figure 8.5 Multiple conditions for wheel center position and distance calculation

Algorithm 1 Pseudocode for calculating distance between center of wheel and sensor

Input: P_M, Pc_W, P_{W1}, P_{Y1}, P_{W2}, Pc_W, PD_M, $RD_{W1,Y1}$, $RD_{Y1,W2}$, $RD_{Y2,W2}$, $MP_{W1,Y1}$
Output: $D_{CW\ S}$
Start:
1: if P_M [0] == P_{W1}:
2: if Pc_W[0][0] - Pc_W[1][0] > $MP_{W1,Y1}$: % condition 1, closer to sensor under W1
3: $D_{CW\ S} = RD_{W1,Y1}$*(PD_M[0]/(- PD_M[0]+ PD_M[1])) % distance to sensor under W1
4: else: % condition 2, closer to sensor under W1
5: $D_{CW\ S} = RD_{W1,Y1}$*(PD_M[0]/(PD_M[0]+ PD_M[1])) % distance to sensor under W1
6: elif P_M [0] == P_{Y1}: % condition 3, closer to sensor under W2
7: $D_{CW\ S} = RD_{Y1,W2}$*(PD_M[1]/(PD_M[0]+ PD_M[1])) % distance to sensor under W2
8: elif P_M [0] == P_{W2}: % condition 4, closer to sensor under W2
9: $D_{CW\ S} = RD_{W2,Y2}$*(PD_M[0]/(PD_M[0]+ PD_M[1])) % distance to sensor under W2

Figure 8.6 Pseudocode for distance calculation

8.1.2 Strain Evaluation and Correction with GFRP-FBG Sensor

Sensing Principle

The GFRP packaged FBG sensors were selected to be the in-pavement strain sensors for WIM measurements in this study. A FBG sensor is fabricated by exposing a segment of a single-mode fiber's core to an intense ultraviolet light pattern through UV laser irradiation [90], [139]. This exposure leads to the formation of the grating, which reflects a specific wavelength of light, referred to as the Bragg wavelength, when broadband incident light is transmitted into the fiber [139]. The expression for the exposed Bragg wavelength is given as [90], [140]:

$$\lambda = 2n\Lambda, \tag{60}$$

where n is the effective index of refraction and Λ is the grating periodicity of the FBG sensor.

For FBG sensors, the sensitive optical fiber interacts with the measured field, resulting in a wavelength shift in the transmitted light [141], [142]. As vehicles pass above the FBG sensors, the Bragg wavelength dynamically changes in response to temperature and strain, influenced by the grating period [90]. Describing the strain–temperature relationship for FBG strain sensors and temperature compensation sensors, the general expression is formulated as [140]:

$$\frac{\Delta\lambda}{\lambda} = \frac{\Delta\lambda_\varepsilon}{\lambda_\varepsilon} + \frac{\Delta\lambda_{T_e}}{\lambda_{T_e}} = (1 - P_e)\varepsilon + (\alpha + \gamma)\Delta T_e, \tag{61}$$

$$\frac{\Delta\lambda_{T_e}}{\lambda_{T_e}} = (\alpha + \gamma)\Delta T_e, \tag{62}$$

where λ is the Bragg wavelength of the grating, experiencing changes in both strain and temperature. The λ_{T_e} and λ_ε represent the Bragg wavelength of the grating, responding exclusively to alterations in temperature and strain. The $\Delta\lambda_{T_e}$ and $\Delta\lambda_\varepsilon$ indicate the shifts in Bragg wavelength due to temperature and strain, respectively. α, γ, and P_e are the thermal expansion coefficient, thermal-optics coefficient, and optical elasticity coefficient, respectively.

Strain Evaluation and Correction

Based on the preceding Equations (1-3), the expression for evaluating strain is presented here as:

$$\varepsilon = \frac{1}{(1-P_e)}\left(\frac{\Delta\lambda}{\lambda} - \frac{\Delta\lambda_{T_e}}{\lambda_{T_e}}\right). \tag{63}$$

However, Equation (4) cannot be directly applied to the GFRP-FBG sensors since the FBG sensors were packaged using GFRP materials. The protective GFRP layer envelops the FBG sensor before the sensor is embedded under the pavement. Positioned within the pavement and shielded by the surrounding material, the GFRP-FBG sensor's strain transfer error varies with different host materials. Considering the impact of the packaging layer between the optical fiber and host material, the relationship between the average strain experienced by the GFRP-FBG sensor ($\bar{\varepsilon}_c$) and the actual strain of the host material ($\bar{\varepsilon}_h$) of the pavement is represented by equation 5 [143]. Here, ϕ is the measurement error of the packaged GFRP-FBG, and its calculation is given by equation 6 [90].

$$\bar{\varepsilon}_h = \frac{\bar{\varepsilon}_c}{1-\phi}, \tag{64}$$

$$\phi = \left|\frac{\bar{\varepsilon}_c - \bar{\varepsilon}_h}{\bar{\varepsilon}_h}\right| = \left|\frac{cosh(\xi l_f)-1}{\xi l_f sinh\,(\xi l_f)}\right|, \tag{65}$$

where l_f is the gage length of the package GFRP-FBG sensor and ξ represents the eigenvalue of its characteristic function, which can be computed as [143]:

$$\xi^2 = \frac{2}{E_0 {r_0}^2\left(\left(\frac{1}{G_{GFRP}}\right)ln\left(\frac{r_{GFRP}}{r_0}\right) + \left(\frac{1}{G_h}\right)ln\left(\frac{r_h}{r_{GFRP}}\right)\right)}, \tag{66}$$

where E_0 and r_0 denote the elastic modulus and outer radius of the optical fiber, respectively; G_{GFRP} and r_{GFRP} represent the shear modulus and outer radius of the protecting layer (GFRP); and G_h and r_h stand for the shear modulus and outer radius of the host material layer.

In this study, the GFRP-FBG sensors were installed inside asphalt concrete pavement. The distinct host material, asphalt concrete, exhibits varying shear modulus (G_h), which is associated with changes in dynamic modulus (E). The shear modulus under diverse conditions of temperature and loading frequencies is determined utilizing a consistent Poisson's ratio (μ), as expressed by Equation 8 [144]. These modifications consider the dynamic measurement error when correcting the strain values obtained from the GFRP-FBG sensors, addressing variations in temperature throughout seasons and loading frequencies influenced by the wheel's contact radius.

$$G_h = \frac{E}{2(1+\mu)}. \tag{67}$$

For various types of pavements, the dynamic modulus may vary, influenced by temperature and loading frequency. Utilizing field-collected dynamic modulus data and NCAT HMA field experiments, a dynamic

modulus master curve is constructed. This involves shifting 24 results obtained from tests at different temperature-frequency combinations using Equations 9 and 10 [148], [149], where E and Max represent dynamic modulus and limiting maximum modulus (6.895 GPa [150]), and δ, β, and γ are fitting parameters. The logarithm of the reduced frequency at the reference temperature (ω_r) is computed using Arrhenius equation [148], [151], where ω is the loading frequency at the test temperature. T_r and T are the reference temperature and test temperature (°K), respectively, with the test temperature determined by the installed temperature sensor adjacent to the GFRP-FBG sensor. The activation energy is denoted as ΔE_a and treated as a fitting parameter.

$$log|E| = \delta + \frac{Max-\delta}{1+e^{\beta+\gamma*log\omega_r}}, \tag{68}$$

$$log\omega_r = log\omega + \frac{\Delta E_a}{19.14714}\left(\frac{1}{T} - \frac{1}{T_r}\right). \tag{69}$$

The loading frequency, assuming the moving load affects the sensor within a loading area six times the contact radius (r), can be estimated by vehicle speed (v) divided by the travel length (12 times the contact radius) [58] as follows:

$$\omega = \frac{v}{12r}. \tag{70}$$

8.1.3 Dynamic Wheel Weight Measurement

This study utilized the computer vision method described in Section 3.2 to obtain the distance between the wheel and GFRP-FBG sensor, and corrected the strain values through GFRP-FBG, as detailed in Section 3.3. After that, the wheel weight can be computed using Equation 12. This equation involves acceleration (a), Poisson ratio (v) obtained from experimental data, and vertical strain ε_z (determined through the FBG sensor and temperature sensor). As vehicles traverse the road, their weight induces deformation, leading to vertical strain propagation through the surface. Despite its horizontal orientation relative to traffic flow, the FBG sensor will be expanded together with the host matrix and induce strains, which can be detected through the measurement of the shifts of center wavelength in reflected light of the FBG sensors.

$$F = \frac{\varepsilon_z*E*A}{a*(\alpha_z - v(\alpha_r+\alpha_t))}. \tag{71}$$

The only remaining factors to be calculated are the contact area (A) and the stress factors α_z, α_r, and α_t, representing vertical, radial, and tangential stresses, respectively. To accurately calculate the contact area, this study referred to research comparing the real tire contact area (detected by a vehicle driving over paper with a recorded footprint of the wheel) with the measured contact area using various equation methods, such as rectangular, circular, and oval [66], [146], [147]. The oval method yielded the lowest average error [66]. The equation for evaluating the contact area based on the oval method is [66]:

$$A = \frac{2}{3} * l * w + \frac{\pi}{3} * \frac{l}{2} * \frac{w}{2}, \tag{72}$$

where l and w are length and width of the contact area. The width of the contact area can be determined through the computer vision process outlined in Section 2.2.3. With the assumption that the contact width is 60% of the contact length [145], the contact length can then be determined accordingly.

For the value of the vertical, radial, and tangential stress factors in pavement analysis, several factors come into effect. For instance, as a vehicle's wheels exert pressure on the road surface, deformations occur at different depths and positions. The variation in stress values can be attributed to factors like the sensor's depth, the material covering the sensor, the number of road layers, characteristics and thickness of each layer, and overall road properties. Furthermore, elements such as contact area, dynamic modulus of the road, temperature changes, loading frequency during vehicle movement, and a significant factor—the distance between the loading point and the sensor collecting loading data—all contribute to the fluctuations in vertical, radial, and tangential stress factors. In addressing this challenge, this study utilizes the KENPAVE software [145], a widely used tool in civil engineering and pavement analysis, to mitigate the wander effect.

With the provided information, including the contact area of the wheel, dynamic modulus of the host material, and characteristics and thickness of the road, KENPAVE software processes the data to generate stress values and calculate stress factors for different distances between the sensor and the wheel loading position. Given the potential variation in sensor positions and the impact of changing wheel load positions, even for the same vehicle, this study employs the stress factor generated by the software for calibration, aiming to reduce the influence of the wander effect on the accuracy of WIM results.

In evaluating the accuracy of weight determination, this study employed three evaluation methods: accuracy, margin of error (MOE), and mean absolute percentage error (MAPE). Within these approaches, the accuracy offers a straightforward measure of how closely the system's weight estimates align with the true values, simplifying the interpretation of overall performance. The assessment of accuracy can be achieved by utilizing the equation below:

$$Accuracy\ (\%) = 100 * \left[1 - \frac{(\hat{Y}_i - Y)}{Y}\right]\%, \tag{73}$$

where Y is the actual weight of the vehicle and $\hat{Y}_i$ represents the estimated weight of the vehicle in the i^{th} experiment.

MOE offers insight into the variability and uncertainty of estimated weights by quantifying the range within which the true weight is likely to fall, aiding in understanding the precision and reliability of the estimates and thereby crucial for evaluating the overall accuracy of the system. A low MOE indicates that the estimated values are closely clustered around the true value, suggesting a high level of precision and reliability in the estimation process. The MOE with (1- α) % confidence is defined as follows:

$$MOE_{1-\alpha} = \pm \frac{\sigma t_{1-\alpha/2,df}}{\mu\sqrt{N}}, \tag{74}$$

where σ is the standard deviation, df represents the degrees of freedom, $t_{1-\alpha/2,df}$ denotes the t-score, μ is the mean values of the measurement, and N is the sample size.

In order to provide a standardized metric for measuring the deviation between estimated and actual weights, MAPE is employed to offer a percentage representation of this deviation to assess accuracy and consistency, thereby informing system performance enhancements. The MAPE is defined as:

$$MAPA = 100 * \left[\frac{1}{N} * \sum_{i=1}^{N} \frac{|\hat{Y}_i - Y|}{Y}\right]\%. \tag{75}$$

8.2 EXPERIMENTAL RESULTS AND DISCUSSION

To confirm the effectiveness of the hybrid WIM system, a field investigation took place on the westbound lanes of Interstate 94, specifically the MnROAD Mainline between exits 201 and 194 in Albertville, MN, USA as shown in Figure 8.7. A camera positioned on the side of the pavement captures images of vehicles from their front and right side. The sensors were strategically placed beneath the asphalt pavement road, with all data collected through the data box. This section offers insights into the field experiment, covering the location, pavement attributes, and the determination of dynamic modulus for the targeted road segment. It also details the sensor deployment, positioning, and the overall experimental setup. The subsequent section discusses the experimental results, evaluating the hybrid WIM system's performance in real-world conditions.

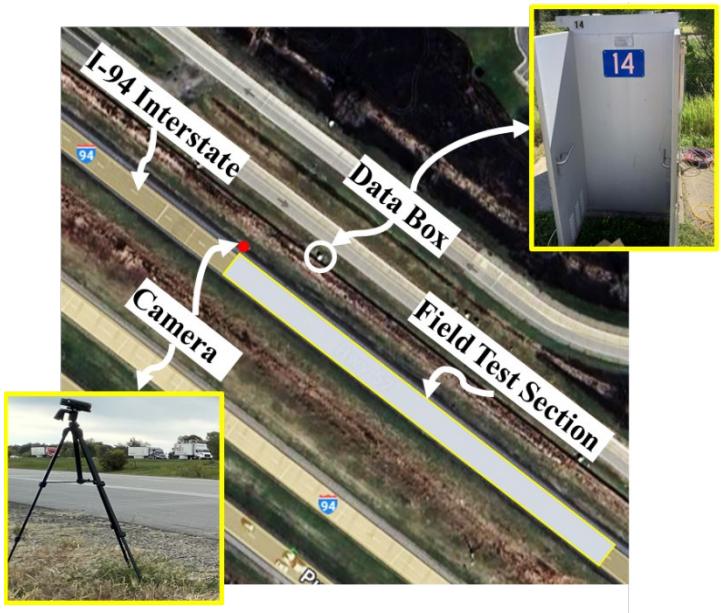

Figure 8.7 Layout of the Hybrid WIM System on Interstate 94

8.2.1 Parameter of Pavement Road

Field tests carried out at the MnROAD mainline on the flexible pavement cross-section, specified in Table 8.1 [87], included GFRP-FBG sensors strategically positioned above the MnDOT Class 5 granular base. Considering that placing the sensor directly near the topmost layer may result in excessively high strain levels, previous research has installed sensors at depths of 0.06 m and 0.22 m from the road surface [167]. Given that the pavement depth in this study is 0.127 m, the sensors were installed at the bottom of the asphalt layer (surface layer). To ensure that the sensors could be covered and placed at the bottom of the surface layer (HMA), a protective layer of HMA was applied to secure the sensors before the installation of the 0.127 m thick HMA layer, ensuring their stability and integrity throughout pavement construction. Dynamic modulus data for this study were sourced from asphalt mixture performance testing experiments conducted by MnROAD and the National Center for Asphalt Technology. The testing involved two specimens (150 mm diameter, 38 mm height), representative of the warm mix asphalt layer in the test section. Dynamic modulus testing included eight frequencies and three temperatures, resulting in 24 temperature and frequency combinations [88].

Table 8.1 Flexible pavement information

Material	Thickness (m)	Poisson's Ratio
HMA	0.127	0.35
Class 5 granular base	0.305	0.35
Class 3 sub-base	0.305	0.35
Selected granular layer	0.178	0.40
Clay loam	0.089	0.40

8.2.2 GFRP-FBG Sensors and Experimental Layout

Two GFRP-FBG sensors were employed in the experiment, aligned parallel to the wheel path. The GFRP-FBG sensors strategically positioned in the longitudinal direction for wheel load detection, which is ideal for high-speed WIM measurements, according to a previous study that utilized a 3D FBG sensor capable of measuring longitudinal, transverse, and vertical directions [58]. They found that the vertical component is highly sensitive to the location of loading. However, it can only effectively respond to a wheel load within 20 cm of the sensor head, posing a challenge to ensure direct alignment of the vehicle over the sensor head during driving. The transverse component of the 3D sensor is less reliant on material properties of the host matrix but still requires the wheel load to be within a 30 cm radius of the sensor. Conversely, the longitudinal component of the 3D sensor demonstrates competitive sensitivity, minimal dependence on property changes of the host matrix due to temperature or loading rate, and sensitivity to loads within a 60 cm radius. Therefore, this study only considers the GFRP-FBG sensors positioned in the longitudinal direction.

The schematic diagram of the GFRP-FBG sensor structure is shown in Figure 8.8. Based on the previous research on the GFRP-FBG sensor [90], essential material parameters were investigated, including the elastic modulus (E_0) and outer radius (r_0) of the optical fiber, shear modulus (G_{GFRP}) and outer radius (r_{GFRP}) of the packaging layer (GFRP), the outer radius of the host material layer (r_h) of the host material layer, and the longitudinal gauge lengths (l_f) of the optical fiber as shown in Table 8.2. The shear modulus of the host material layer (which is HMA in this study) was calculated based on the dynamic modulus of elasticity and Poisson's ratio of the host material. The calculated shear modulus and the parameters were then employed to calculate the measurement error attributable to the host material; this correction was subsequently applied to adjust the strain calculations obtained from the sensor.

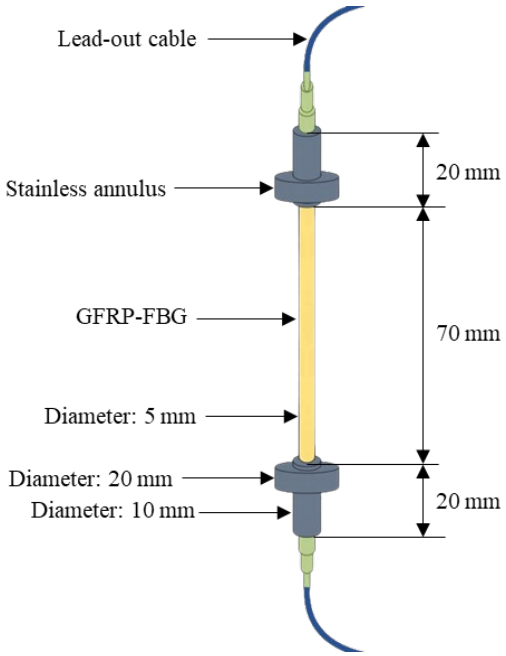

Figure 8.8 The schematic diagram of the GFRP-FBG sensor

Table 8.2 GFRP-FBG sensor strain transfer parameters

E_0 (GPa)	r_0 (mm)	G_{GFRP} (GPa)	r_{GFRP} (mm)	r_h (mm)	l_f (mm)
70	0.0625	5	2.5	25	70

The GFRP-FBG sensor is depicted in Figure 8.9(a), with both sides covered by the base layer while the sensor portion is positioned above the base layer, as illustrated in Figure 8.9(b). Epoxy is then applied to secure the sensor in place, as depicted in Figure 8.9(c), followed by the addition of asphalt (Figure 8.9(d)) before paving with the machine (Figure 8.9(e)) to protect the sensors. Subsequently, a roller truck is used for compaction and smoothing of the new asphalt pavement to ensure a uniform surface, as shown in Figure 8.9(f).

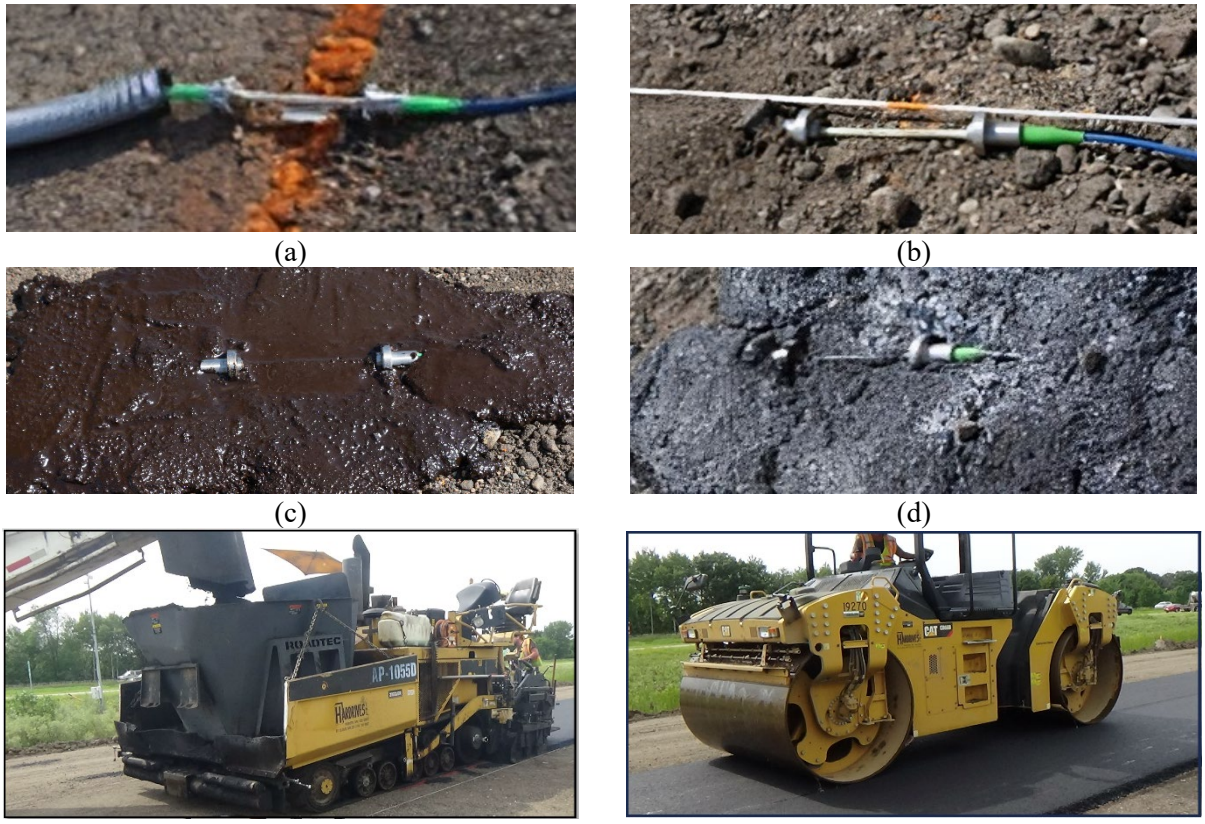

Figure 8.9 (a) GFRP-FBG sensor; (b) sensor positioned above base layer; (c) application of epoxy for sensor adhesion; (d) addition of asphalt to protect sensor; (e) paving asphalt with asphalt paving machine; (f) compaction and smoothing with roller truck

In addition to the GFRP-FBG sensors, a temperature sensor was used for temperature compensation, and a roadside camera captured images for computer vision, as depicted in Figure 8.10. FBG-1 is strategically placed above the wheel path, while FBG-2 is positioned 0.521 m away from FBG-1. Both FBG-1 and FBG-2, and the temperature sensors, are aligned on the same axis. To ensure accurate positioning, four specific locations are designated for calibration in this study.

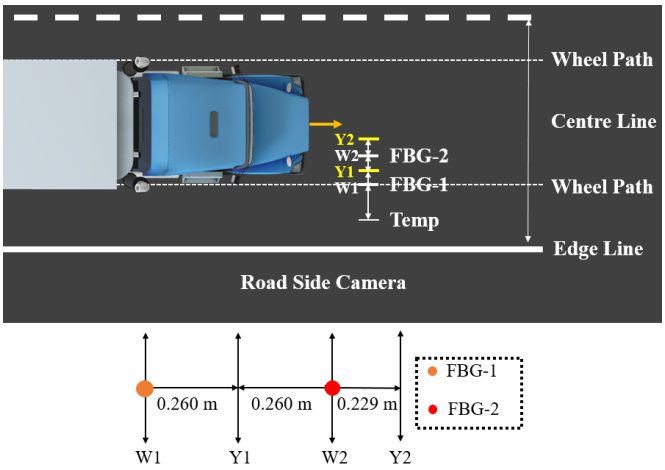

Figure 8.10 Experimental setup layout with GFRP-FBG sensors, temperature sensor, and roadside camera

8.2.3 Field Test for WIM Measurement

The field test involved a Class 9 semi-truck from the MnROAD facility with a total gross weight of 36,196 kg. The individual axle weights for the first, second, third, fourth, and fifth axles were 5,352 kg, 8,006 kg, 7,462 kg, 7,620 kg, and 7,756 kg, respectively. The distances between the wheels were 5.2 m (first to second), 1.4 m (second to third), 10.4 m (third to fourth), and 1.3 m (fourth to fifth), and this study specifically focused on measuring the weight of a single wheel in the first axle.

During the test, the semi-truck passed over the sensor location, and repeated the passage over each position seven times, aiming to align the wheels directly above the sensor positions. Achieving precise control over the truck's movement within the specified areas and at the designated speed proved challenging, particularly when the two locations were close to. Hence, both the sensor data and captured images were utilized to accurately determine the vehicle's speed and location as it passed through the specified points. As the driver maneuvers the truck over the sensors, the distance between the actual passing position and the sensor location can be considered the wandering distance, and this distinction aids in advancing research on the impact of the wandering effect.

8.2.4 Analytical Process for Experimental Results

To accurately measure vehicle weight, the analytical process includes three parts. The first part is studying the stress factors at various wandering distances. Additionally, it reveals the results obtained from computer vision for the distance from the wheel loading position to the sensor (wandering distance), along with the corresponding stress factors. Furthermore, the strain calculated through the GFRP-FBG sensors and temperature sensor, combined with the stress factors corresponding to the wandering distance, is utilized to estimate vehicle weight.

Stress Factors at Various Wandering Distances

Given that the sensor positions were fixed, the collected wavelength by the sensor varied when the vehicle was at different positions. Consequently, the phenomenon of wavelength variation needs to be addressed, and the use of KENPAVE software becomes essential to tackle this challenge. As presented in Figure 8.11, the input data for KENPAVE software include 1) the number of road layers, 2) thickness for each layer, 3) the Poisson's ratio for individual layers, and 4) elastic modulus values at tested

temperatures; using the tested temperature obtained by temperature sensor, the following elastic modulus values were used for HMA, granular base, sub-base clay loam, granular, and clay loam: 4.826, 0.414, 0.276, 0.083, and 0.083 GPa, respectively. After that, the stress factors were calculated using stress overweight, as illustrated in Figure 8.11.

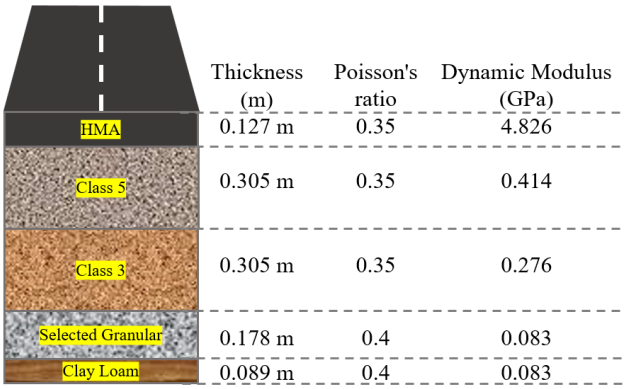

Figure 8.11 Input data of pavement for KENPAVE software

Therefore, Figure 8.12 plots the relationship between calculated stress factors and the sensor-wheel distance. Considering the maximum distance between the sensor and the loading position are close to 0.1 m in this study, stress factor values concerning the distances ranged from 0 to 0.3 m (Figure 8.12). The data in this figure was used to work with the distance between these sensors and was assessed using computer vision. A closer examination of Figure 8.12 reveals intriguing patterns in stress factor variations. As the wandering distance increases, there is a noticeable change in the stress factors recorded by the sensors. These variations could be attributed to the differential distribution of load as a vehicle passes over the sensor array. Understanding these patterns is vital for interpreting the impact of vehicle weight and pressure distribution on road infrastructure. For example, as the distance between the wheel loading position and the sensor increases, the vertical stress factor exhibits a slight decrease from 0.328 to 0.062. The vertical stress factor decreases, which may indicate a reduction in the direct load impact on the sensor as the distance increases. This could suggest a dispersion of the load over a wider area, leading to less intense stress directly above the sensor. Simultaneously, the radial stress factor increases from -1.582 to 0.202, and the tangential stress factor rises from -1.582 to -0.273. Therefore, the observed stress patterns suggest a direct correlation with the vehicle's weight distribution. Additionally, given that there are two embedded sensors and considering the higher accuracy achieved with the sensor closest to the wheel loading position, the subsequent calculation process is configured to automatically select data from the nearest sensor for determining vehicle weight.

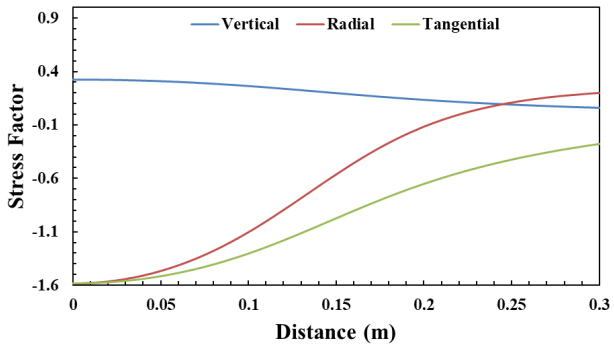

Figure 8.12 Vertical, longitudinal, and tangential stress factors

Computer Vision-Based Wandering Distance and Corresponding Stress Factors

Utilizing the computer vision methodology detailed in Section 2.2 enhances the accuracy of distance measurements, leveraging digital precision for improved results. The wandering distances were determined and presented in Table 8.3. The numerical labeling ranging from 1 to 7 designates sensors positioned close to FBG-1, whereas sensors numbered 8 to 14 are near FBG-2. This sequential arrangement is based on their respective wandering distances, ensuring a methodical and precise representation of proximity for analytical clarity and accuracy. To achieve the highest accuracy in evaluating vehicle weight, the analysis focuses solely on the closest sensor. Consequently, Table 8.3 displays the wandering distance and corresponding vertical, radial, and tangential stress factors for the nearest sensor.

Table 8.3 Stress factors and corresponding wandering distance

Vehicle Number	Distance to (FBG-1) (m)	Vertical Stress Factor	Radial Stress Factor	Tangential Stress Factor
1	0.028	0.323	-1.545	-1.560
2	0.038	0.319	-1.514	-1.542
3	0.053	0.311	-1.449	-1.504
4	0.074	0.295	-1.325	-1.432
5	0.114	0.250	-0.957	-1.216
6	0.119	0.243	-0.902	-1.184
7	0.124	0.237	-0.847	-1.150
Vehicle Number	Distance to (FBG-2) (m)	Vertical Stress Factor	Radial Stress Factor	Tangential Stress Factor
8	0.003	0.328	-1.581	-1.581
9	0.015	0.326	-1.571	-1.575
10	0.058	0.307	-1.422	-1.488
11	0.061	0.305	-1.407	-1.480
12	0.069	0.299	-1.360	-1.452
13	0.094	0.275	-1.160	-1.336
14	0.119	0.243	-0.902	-1.184

This organized presentation allows for comparisons between stress factors recorded at different distances from the FBGs, shedding light on the varying impacts of vehicle weight and pressure distribution. Additionally, the data provides insights into stress patterns, informing future decisions regarding structural integrity and vehicle performance assessment strategies. The application of the proposed computer vision method, as detailed in Section 2.2, plays a vital role in enhancing the precision of distance measurements. This digital accuracy is paramount in accurately determining the stress factors associated with different wandering distances. By leveraging computer vision, the hybrid WIM system overcomes the limitations inherent in traditional WIM systems, offering a more nuanced understanding of vehicle-road interactions.

Accuracy Evaluation of Vehicle Weight Monitoring

As vehicles traverse the road, the FBG sensor's center wavelength changes can detect the strain changes inside the pavement in horizontal direction and through Poisson's effect, the strains in vertical direction can be calculated and further converted into weight of the passing vehicles , as illustrated in Figure 8.13. Each peak signifies a notable alteration in center wavelength, indicating of the strain endured by the road surface under the vehicle's weight. By analyzing the wavelength changes captured by the GFRP-FBG sensor and the temperature sensors, strain can be calculated using equations 4 to 11, and the resulting values are presented in Table 8.4. Subsequently, vehicle weights were determined based on these calculated strain values and the stress factors outlined in Table 8.3. This study specifically focuses on evaluating the weight of the first right single wheel of the truck, with an axle weight of 5,352 kg, resulting in an expected weight of 2,676 kg for the first right single wheel. As demonstrated in Table 8.4, the WIM system is capable of calculating the weight of a single wheel, ranging from 2316 to 3099 kg, with an accuracy of 84.2% to 97.5%, and this performance is indicative of a WIM system with excellent accuracy. Computer vision plays a crucial role in accurately determining the wandering distance between the vehicle wheels and the sensors. This precision is vital, as even minor deviations in distance can significantly impact the accuracy of weight estimations. By providing digital precision, computer vision enhances the overall reliability and effectiveness of the hybrid WIM system.

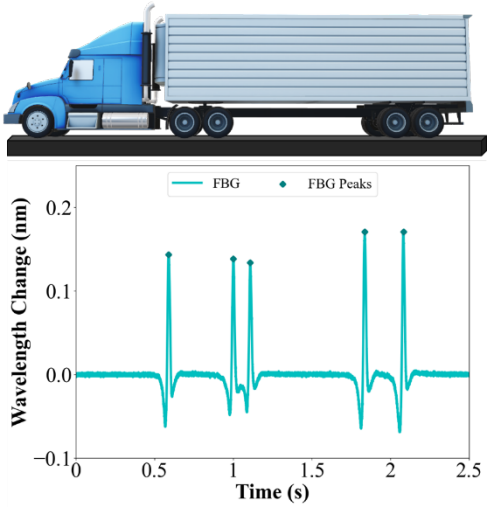

Figure 8.13 Wavelength change peaks induced by vehicle passage

Table 8.4 Strain calculation results and vehicle weights

Vehicle Number	Wavelength Change (FBG) (nm)	Wavelength Change (T) (nm)	Strain ($\times 10^{-4}$)	Distance (m)	Weight (kg)	Accuracy (%)
1	0.143	−0.002	1.194	0.028	2744	97.5
2	0.151	−0.001	1.252	0.038	2920	90.9
3	0.142	−0.002	1.183	0.053	2851	93.5
4	0.132	−0.003	1.111	0.074	2856	93.3
5	0.113	−0.002	0.951	0.114	3046	86.2
6	0.112	−0.001	0.931	0.119	3099	84.2
7	0.105	−0.001	0.875	0.124	3031	86.8
8	0.143	0.001	1.186	0.003	2679	99.9
9	0.153	0.002	1.260	0.015	2861	93.1
10	0.127	0.000	1.057	0.058	2582	96.5
11	0.136	−0.002	1.153	0.061	2839	93.9
12	0.121	0.001	0.998	0.069	2519	94.1
13	0.126	−0.001	1.055	0.094	2977	88.7
14	0.082	−0.002	0.696	0.119	2316	86.5

The accuracy of weight estimation is found to be influenced by the wandering distance between the vehicle wheel and the sensor, with closer proximity resulting in higher accuracy. With distances ranging from 0.028 m to 0.124 m from FBG 1, the average accuracy exceeds 90%. Similarly, distances from the wheel loading position ranging from 0.003 m to 0.119 m result in an average accuracy exceeding 93%. The highest accuracy is achieved when the distance between the sensor and the wheel loading position is 0.003 m. Figure 8.14 illustrates the relationship between accuracy and the different wandering distances of all 14 vehicles from the sensors and wheel loading positions. The results indicate that when the distance is less than approximately 0.1 m, the accuracy exceeds 90%. Furthermore, for wandering distance less than 0.13 m, the accuracy is consistently higher than 85%.

The additional statistical findings depicted in Table 8.5 reveal that among the 14 runs, the estimation process achieves an average accuracy of 91.8%, emphasizing its effectiveness in approximating true values. Considering a confidence level of 95%, the calculated MOE of 127.9 kg for a real weight of 2676 kg provides insight into the range within which the true weight is likely to fall, given the variability in the estimation process. Additionally, the small MAPE of 8.2% underscores the average deviation between estimated and true accuracy values. Therefore, compared to traditional WIM systems, our hybrid approach demonstrates superior accuracy, particularly in scenarios where vehicle positioning varies. The ability of computer vision to precisely measure wandering distances, combined with the sensitive response of GFRP-FBG sensors, results in a more robust and reliable system for vehicle weight monitoring.

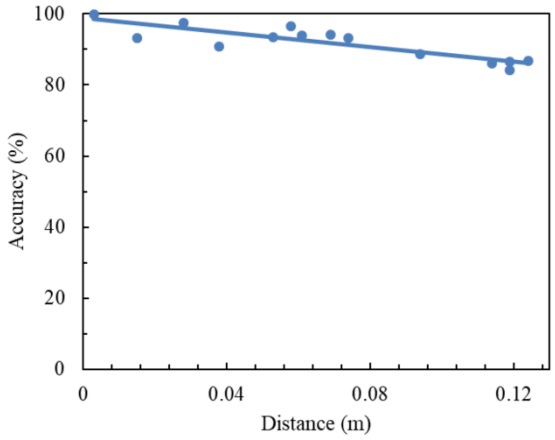

Figure 8.14 Accuracy trends in vehicle weight estimation at varying distances

Table 8.5 Statistical analysis results for accuracy assessment

Degree Freedom	Confidence Level	T Score	Standard Deviation	Average Accuracy	MOE	MAPE
13	95%	2.160	221.442	91.8%	127.9	8.2%

8.3 Summary of Hybrid WIM Systems: Using GFRP-FBG Sensors and Computer Vision to Mitigate the Wander Effect

In conclusion, this study proposed a novel hybrid system for WIM that effectively mitigates the wander effect in vehicle weight assessment. The system can detect wandering distances by utilizing computer vision and when combined with data from in-pavement strain sensors and a temperature sensor, it established a cost-effective and minimally human-involved approach for WIM measurements. Key contributions of this study are summarized below:

This study addresses the challenges encountered by the two main WIM systems and proposes a hybrid system for accurately measuring vehicle weight. The hybrid system is designed for WIM achieved accurate measurements with a low equipment cost, incorporating only two in-pavement sensors, one temperature sensor, and a standard camera.

This study minimizes human involvement and addresses the wander effect by integrating computer vision, which enables automatic distance calculation and calibration. Considering cost-effectiveness and minimizing limitations, this study opts to utilize a standard camera with low cost and low-resolution imagery, which may pose challenges in adverse weather conditions. To address this issue, computer vision technology is employed to accurately determine the distance between the sensor and wheel position.

To minimize disruption to traffic flow, this study positions the camera to the right of the road, capturing images of vehicles from the front right side. However, this arrangement presents challenges in distance calibration, as objects appear closer when nearby and farther when distant. To address this issue, a calibration process is implemented to effectively resolve distance discrepancies.

In adverse weather conditions like strong winds, which can shift the camera angle and lead to inaccurate distance evaluation, this study implements automatic calibration methods to ensure precise distance measurement.
The hybrid system achieves heightened accuracy at closer sensor distances, exceeding 90% for distances under 0.1 m and consistently surpassing 85% for distances under 0.13 m.

This paper holds significant implications for the transportation sector, offering a cost-effective, real-time detection solution for vehicle wheel weight. By minimizing human intervention and enhancing accuracy, the proposed system contributes to improved efficiency in transportation operations and road maintenance. Future research will focus on analyzing the impact of vehicle speed and weather conditions on computer vision results, particularly regarding the determination of the distance between the sensor and wheel loading position, to enhance accuracy. In addition, refinement of the hybrid system will involve exploring the integration of additional embedded sensors to enhance accuracy and broaden applications. The adaptability of the system to diverse vehicle scenarios will be investigated for effectiveness across various transportation contexts. This study will also delve into multi-axle vehicle assessment, including dual-wheel weight evaluations and analysis of load distribution and strain patterns, aiming to advance WIM technology for practical solutions in the evolving transportation industry.

9. CONCLUSION AND FUTURE WORK

The series of studies significantly contributes to the field of pavement engineering and vehicle weight monitoring, focusing on the importance and innovation of WIM systems. In the analysis of traffic loading impacts on pavement performance, SVR models demonstrate the ability to accurately predict pavement distress caused by varying traffic loads. The research highlights that integrating WIM systems into this analysis provides crucial data on real-time axle loads, which enhances the predictive accuracy of machine learning models. This integration enables infrastructure managers to better assess pavement conditions and optimize maintenance strategies, ensuring more efficient use of resources and extending the lifespan of pavement infrastructure.

The investigation into the impact of overweight traffic on pavement survival life utilizes a random survival forest algorithm, emphasizing the critical role of WIM systems in collecting accurate axle load spectra. Overweight vehicles significantly reduce pavement life, leading to severe distresses like alligator cracking and rutting. By providing precise measurements of traffic loads, WIM systems enable the development of more effective regulatory measures and maintenance strategies. This study illustrates how WIM data, coupled with advanced analytics, can guide infrastructure planning and reduce the adverse effects of heavy traffic on road networks.

In the mechanistic-empirical analysis of pavement performance, considering dynamic axle load spectra due to longitudinal unevenness, WIM systems are crucial in capturing the variations in axle loads caused by road surface irregularities. The study shows that longitudinal unevenness can lead to increased dynamic loads, accelerating pavement deterioration. By utilizing WIM data, researchers can better understand the impact of these dynamic loads on pavement performance, offering valuable insights for designing more resilient pavements capable of withstanding modern traffic demands.

The study on asphalt pavement temperature prediction models highlights the importance of incorporating environmental factors alongside traffic data from WIM systems. Using multiple regression and ANN approaches, the research reveals that temperature, solar radiation, and humidity significantly affect pavement temperatures. Pavement temperature data can be used to improve WIM systems accuracy, providing more accurate and real-time insights into how traffic conditions interact with environmental factors. This comprehensive approach supports the development of pavements that are more resilient to climatic variations, ultimately reducing maintenance costs and extending pavement life.

In addressing vehicle weight monitoring, the development of hybrid WIM systems integrating computer vision with in-pavement sensors represents a significant advancement. These systems effectively mitigate the wander effect, a major source of inaccuracies in traditional WIM measurements. By combining spatial data from cameras with strain measurements from sensors, these systems provide highly accurate vehicle weight data, essential for maintaining road infrastructure and ensuring compliance with weight regulations. The successful application of these technologies underscores their transformative potential in enhancing traffic management and road safety.

Lastly, the advanced hybrid WIM system that integrates computer vision and in-pavement sensors further demonstrates the capabilities of modern vehicle weight monitoring solutions. This approach offers precise weight measurements by overcoming challenges related to vehicle position variability and environmental factors. The research highlights the system's potential to revolutionize vehicle weight monitoring, providing crucial data for infrastructure maintenance and regulatory compliance, ultimately supporting more efficient and safer transportation networks.

In the future, expanding machine learning models to incorporate a broader range of traffic conditions, environmental factors, and material properties will enhance the generalizability of findings across various climatic regions and traffic patterns. By integrating real-time data processing capabilities into these models, dynamic adjustments in pavement management strategies can be achieved, optimizing infrastructure resilience and efficiency.

Further development of WIM systems should focus on examining the effects of varying vehicle speeds, multi-axle configurations, and environmental factors on measurement accuracy. This exploration can refine hybrid WIM systems, making them more applicable across diverse road conditions.

Additionally, the exploration of smart pavements and innovative materials should continue, emphasizing the integration of sensors and intelligent systems within pavement structures. This approach will enable proactive maintenance and management, reducing the risk of unexpected failures and enhancing road safety. Future research should also investigate the integration of these technologies into smart transportation networks, optimizing traffic flow and infrastructure utilization to create more efficient and responsive transportation systems.

10. REFERENCES

[1] Statista Research Department, "Number of motor vehicles in U.S.," *Statista*. Available: https://www.statista.com/statistics/183505/number-of-vehicles-in-the-united-states-since-1990/. [Accessed: May 24, 2023]

[2] Z. Xiong, J. Li, and H. Wu, "Understanding operation patterns of urban online ride-hailing services: A case study of Xiamen," *Transport Policy*, vol. 101, pp. 100–118, 2021.

[3] X. Guangnian, L. Qiongwen, N. Anning, and C. Zhang, "Research on carbon emissions of public bikes based on the life cycle theory," *Transportation Letters*, vol. 15, no. 4, pp. 278–295, 2023.

[4] G. Duan, X. Ma, J. Wang, Z. Wang, and Y. Wang, "Optimization of Urban Bus Stops Setting Based on Data Mining," *Int. J. Patt. Recogn. Artif. Intell.*, vol. 35, no. 08, p. 2159028, Jun. 2021, doi: 10.1142/S021800142159028X

[5] D. P. J. Szary and D. A. Maher, "Implementation of Weigh-in-Motion (WIM) Systems," 2009.

[6] J. Wang and M. Wu, "An overview of research on weigh-in-motion system," in *Fifth world congress on intelligent control and automation (IEEE cat. no. 04EX788)*, IEEE, 2004, pp. 5241–5244.

[7] Z. Li and K. C. Sinha, "A methodology to estimate load and non-load shares of highway pavement routine maintenance and rehabilitation expenditures," 2000.

[8] G. P. R. Ong, T. E. Nantung, and K. C. Sinha, "Indiana pavement preservation program," 2010.

[9] O. E. Gungor *et al.*, "Development of an overweight vehicle permit fee structure for Illinois," *Transport Policy*, vol. 82, pp. 26–35, 2019.

[10] D. Wu, J. Zhao, H. Liu, and C. Yuan, "The assessment of damage to Texas highways due to oversize and overweight loads considering climatic factors," *International Journal of Pavement Engineering*, vol. 20, no. 7, pp. 853–865, 2019.

[11] M. R. Schlotjes, M. P. Burrow, H. T. Evdorides, and T. F. Henning, "Using support vector machines to predict the probability of pavement failure," in *Proceedings of the Institution of Civil Engineers-Transport*, Thomas Telford Ltd, 2015, pp. 212–222.

[12] H. Ziari, M. Maghrebi, J. Ayoubinejad, and S. T. Waller, "Prediction of pavement performance: Application of support vector regression with different kernels," *Transportation Research Record*, vol. 2589, no. 1, pp. 135–145, 2016.

[13] H. Gong, Y. Sun, X. Shu, and B. Huang, "Use of random forests regression for predicting IRI of asphalt pavements," *Construction and Building Materials*, vol. 189, pp. 890–897, 2018.

[14] A. Fathi, M. Mazari, M. Saghafi, A. Hosseini, and S. Kumar, "Parametric Study of Pavement Deterioration Using Machine Learning Algorithms," in *Airfield and Highway Pavements 2019*, Chicago, Illinois: American Society of Civil Engineers, Jul. 2019, pp. 31–41. doi: 10.1061/9780784482476.004. Available: https://ascelibrary.org/doi/10.1061/9780784482476.004. [Accessed: Jun. 05, 2024]

[15] P. Marcelino, M. de Lurdes Antunes, E. Fortunato, and M. C. Gomes, "Machine learning approach for pavement performance prediction," *International Journal of Pavement Engineering*, vol. 22, no. 3, pp. 341–354, 2021.

[16] S. Inkoom, J. Sobanjo, A. Barbu, and X. Niu, "Prediction of the crack condition of highway pavements using machine learning models," *Structure and Infrastructure Engineering*, vol. 15, no. 7, pp. 940–953, 2019.

[17] S. Inkoom, J. Sobanjo, A. Barbu, and X. Niu, "Pavement crack rating using machine learning frameworks: Partitioning, bootstrap forest, boosted trees, Naïve bayes, and K-Nearest neighbors," *Journal of Transportation Engineering, Part B: Pavements*, vol. 145, no. 3, p. 04019031, 2019.

[18] K. C. Dey, M. Chowdhury, W. Pang, B. J. Putman, and L. Chen, "Estimation of Pavement and Bridge Damage Costs Caused by Overweight Trucks," *Transportation Research Record*, vol. 2411, no. 1, pp. 62–71, Jan. 2014, doi: 10.3141/2411-08

[19] J. M. Sadeghi and M. Fathali, "Deterioration analysis of flexible pavements under overweight vehicles," *Journal of Transportation Engineering*, vol. 133, no. 11, pp. 625–633, 2007.
[20] H. Wang, J. Zhao, and Z. Wang, "Impact of overweight traffic on pavement life using weigh-in-motion data and mechanistic-empirical pavement analysis," in *9th International Conference on Managing Pavement Assets*, 2015.
[21] K. Chatti, H. Salama, and C. El Mohtar, "Effect of heavy trucks with large axle groups on asphalt pavement damage," in *Proc., 8th Int. Symp. on Heavy Vehicle Weights and Dimensions*, 2004. Available: https://hvttforum.org/wp-content/uploads/2019/11/EFFECT-OF-HEAVY-TRUCKS-WITH-LARGE-AXLE-GROUPS-ON-ASPHALT-PAVEMENT-DAMAGE-Chatti.pdf. [Accessed: Jun. 05, 2024]
[22] H. K. Salama, K. Chatti, and R. W. Lyles, "Effect of heavy multiple axle trucks on flexible pavement damage using in-service pavement performance data," *Journal of transportation engineering*, vol. 132, no. 10, pp. 763–770, 2006.
[23] D. Rys, J. Judycki, and P. Jaskula, "Analysis of effect of overloaded vehicles on fatigue life of flexible pavements based on weigh in motion (WIM) data," *International Journal of Pavement Engineering*, vol. 17, no. 8, pp. 716–726, 2016.
[24] H. Wang and J. Zhao, "Development of overweight permit fee using mechanistic-empirical pavement design and life-cycle cost analysis," *Transport*, vol. 31, no. 2, pp. 156–166, 2016.
[25] D. Batioja-Alvarez, S.-F. Kazemi, E. Y. Hajj, R. V. Siddharthan, and A. J. T. Hand, "Statistical Distributions of Pavement Damage Associated with Overweight Vehicles: Methodology and Case Study," *Transportation Research Record*, vol. 2672, no. 9, pp. 229–241, Dec. 2018, doi: 10.1177/0361198118793243
[26] H. H. Titi, N. J. Coley, and V. Latifi, "Evaluation of pavement performance due to overload single-trip permit truck traffic in Wisconsin," *Advances in Civil Engineering*, vol. 2018, 2018.
[27] ARA, Inc., "Guide for Mechanistic-Empirical Design of New and Rehabilitated Pavement Structures," *Washington DC*, 2004, Available: https://www.researchgate.net/profile/J-Tarafdar/post/How-to-unify-heavy-clay-soil-survey-Bulk-Density-measures-that-have-different-moisture-contents/attachment/5a3616ac4cde266d587b95e2/AS%3A572450270597120%401513494188466/download/2appendices_DD.pdf. [Accessed: Jun. 19, 2024]
[28] E. ASTM, "Standard specification for highway weigh-in-motion (WIM) systems with user requirements and test methods E 1318-09," *2007 Annual Book of ASTM Standards. Edited by ASTM Committee E17-52 on Traffic Monitoring. ASTM International, USA*, 2009.
[29] F. Navarrina *et al.*, "Comprehensive model for fatigue analysis of flexible pavements considering effects of dynamic axle loads," *Transportation Research Record*, vol. 2524, no. 1, pp. 110–118, 2015.
[30] J.-P. Bilodeau, L. Gagnon, and G. Doré, "Assessment of the relationship between the international roughness index and dynamic loading of heavy vehicles," *International Journal of Pavement Engineering*, vol. 18, no. 8, pp. 693–701, Aug. 2017, doi: 10.1080/10298436.2015.1121780
[31] T. D. Gillespie, "Everything you always wanted to know about the IRI, but were afraid to ask," *The University of Michigan Transportation Research Institute. Nebraska*, 1992, Available: https://citeseerx.ist.psu.edu/document?repid=rep1&type=pdf&doi=a1ecc343dfce49b7f77529da75cc3d0dddac12a2. [Accessed: Jun. 05, 2024]
[32] W. Hu, Q. Zhao, Y. Liu, Z. Li, and X. Kong, "Damage evaluation of the paving around manholes under vehicle dynamic load," *Advances in Materials Science and Engineering*, vol. 2020, pp. 1–11, 2020.
[33] S. M. Bonabi, *Impact of truck suspension and road roughness on loads exerted to pavements*. The University of Texas at El Paso, 2011.
[34] M. Elisher, N. Trevorrow, L. Callaway, and C. Blanksby, "Measurement and analysis of dynamic wheel loads," 2012. Available: https://trid.trb.org/View/1141775. [Accessed: Jun. 05, 2024]

[35] R. Hassan and K. McManus, “Estimating dynamic loading of pavements from surface profile properties,” *Road & Transport Research*, vol. 10, no. 3, p. 3, 2001.
[36] S. Misaghi, C. Tirado, S. Nazarian, and C. Carrasco, “Impact of pavement roughness and suspension systems on vehicle dynamic loads on flexible pavements,” *Transportation Engineering*, vol. 3, p. 100045, 2021.
[37] M. W. Sayers, T. D. Gillespie, and C. A. V. Queiroz, “The international road roughness experiment: A basis for establishing a standard scale for road roughness measurements,” *Transportation Research Record*, vol. 1084, pp. 76–85, 1986.
[38] D. Rys, “Investigation of weigh-in-motion measurement accuracy on the basis of steering axle load spectra,” *Sensors*, vol. 19, no. 15, p. 3272, 2019.
[39] P. Múčka, “Road Roughness Limit Values Based on Measured Vehicle Vibration,” *J. Infrastruct. Syst.*, vol. 23, no. 2, p. 04016029, Jun. 2017, doi: 10.1061/(ASCE)IS.1943-555X.0000325
[40] J. Zhao and H. Wang, “Mechanistic-empirical analysis of asphalt pavement fatigue cracking under vehicular dynamic loads,” *Construction and Building Materials*, vol. 284, p. 122877, 2021.
[41] D. Rys and P. Burnos, “Study on the accuracy of axle load spectra used for pavement design,” *International Journal of Pavement Engineering*, vol. 23, no. 11, pp. 3706–3715, 2022.
[42] Y. Qiao, “Flexible pavements and climate change: impact of climate change on the performance, maintenance, and life-cycle costs of flexible pavements,” University of Nottingham, 2015.
[43] B. B. Teltayev, J. Liu, and E. A. Suppes, “Distribution of temperature, moisture, stress and strain in the highway,” *Magazine of Civil Engineering*, no. 7 (83), pp. 102–113, 2018.
[44] C. Yang, D. Yun, J. Kim, and S. Shin, “Estimation road surface temperature variation using commercial vehicle ambient sensor,” in *IOP Conference Series: Materials Science and Engineering*, IOP Publishing, 2019, p. 022027.
[45] Z. Ye *et al.*, “Real-time and efficient traffic information acquisition via pavement vibration IoT monitoring system,” *Sensors*, vol. 21, no. 8, p. 2679, 2021.
[46] E. Denneman, “Application of locally developed pavement temperature prediction algorithms in performance grade (PG) binder selection,” 2007.
[47] M. A. Elshaeb, S. M. El-Badawy, and E.-S. A. Shawaly, “Development and impact of the Egyptian climatic conditions on flexible pavement performance,” *American Journal of Civil Engineering and Architecture*, vol. 2, no. 3, pp. 115–121, 2014.
[48] J. Chen, H. Wang, and P. Xie, “Pavement temperature prediction: Theoretical models and critical affecting factors,” *Applied thermal engineering*, vol. 158, p. 113755, 2019.
[49] B. J. Dempsey, *A heat-transfer model for evaluating frost action and temperature relatedeffects in multilayered pavement systems*. University of Illinois at Urbana-Champaign, 1969.
[50] D. Wang, “Simplified analytical approach to predicting asphalt pavement temperature,” *Journal of Materials in Civil Engineering*, vol. 27, no. 12, p. 04015043, 2015.
[51] R. Kršmanc, A. Š. Slak, and J. Demšar, “Statistical approach for forecasting road surface temperature,” *Meteorological applications*, vol. 20, no. 4, pp. 439–446, 2013.
[52] S. Zhong *et al.*, “Machine learning: new ideas and tools in environmental science and engineering,” *Environmental Science & Technology*, vol. 55, no. 19, pp. 12741–12754, 2021.
[53] B. Matić, D. Matić, S. Sremac, N. Radović, and P. Viđikant, “A model for the pavement temperature prediction at specified depth using neural networks,” *Metalurgija*, vol. 53, no. 4, pp. 665–667, 2014.
[54] A. Rigabadi, M. Rezaei Zadeh Herozi, and A. Rezagholilou, “An attempt for development of pavements temperature prediction models based on remote sensing data and artificial neural network,” *International Journal of Pavement Engineering*, vol. 23, no. 9, pp. 2912–2921, 2022.
[55] E. O. Lukanen, R. Stubstad, R. C. Briggs, and B. Intertec, “Temperature predictions and adjustment factors for asphalt pavement,” Turner-Fairbank Highway Research Center, 2000.
[56] C. Marshall, R. Meier, and M. Welch, “Seasonal temperature effects on flexible pavements in Tennessee,” *Transportation research record*, vol. 1764, no. 1, pp. 89–96, 2001.
[57] Federal Highway Administration, “Weigh-In-Motion Pocket Guide, Part 2,” 2018.

[58] Al-Tarawneh, Mu'ath, Y. Huang, P. Lu, and R. Bridgelall, "Weigh-In-Motion system in flexible pavements using fiber Bragg grating sensors part A: Concept," *IEEE Transactions on Intelligent Transportation Systems*, vol. 21, no. 12, pp. 5136–5147, 2019.
[59] K. S. C. Kuang, S. T. Quek, C. G. Koh, W. J. Cantwell, and P. J. Scully, "Plastic optical fibre sensors for structural health monitoring: A review of recent progress," *Journal of sensors*, vol. 2009, 2009.
[60] L. Xu, S. Shi, F. Yan, Y. Huang, and Y. Bao, "Experimental study on combined effect of mechanical loads and corrosion using tube-packaged long-gauge fiber Bragg grating sensors," *Structural Health Monitoring*, p. 14759217231164960, 2023.
[61] L. Xu, D. Zhang, Y. Huang, S. Shi, H. Pan, and Y. Bao, "Monitoring epoxy coated steel under combined mechanical loads and corrosion using fiber Bragg grating sensors," *Sensors*, vol. 22, no. 20, p. 8034, 2022.
[62] H. Zhang *et al.*, "Static and ultrasonic structural health monitoring of full-size aerospace multi-function capsule using FBG strain arrays and PSFBG acoustic emission sensors," *Optical Fiber Technology*, vol. 78, p. 103316, 2023.
[63] C.-Y. Hong, Y.-F. Zhang, M.-X. Zhang, L. M. G. Leung, and L.-Q. Liu, "Application of FBG sensors for geotechnical health monitoring, a review of sensor design, implementation methods and packaging techniques," *Sensors and Actuators A: Physical*, vol. 244, pp. 184–197, 2016.
[64] T. Jiao *et al.*, "Characterization of Engineering-Suitable Optical Fiber Sensors Packaged with Glass Fiber-Reinforced Polymers," *Symmetry*, vol. 14, no. 5, p. 973, 2022.
[65] M. Q. Feng, R. Y. Leung, and C. M. Eckersley, "Non-contact vehicle weigh-in-motion using computer vision," *Measurement*, vol. 153, p. 107415, 2020.
[66] X. Kong, J. Zhang, T. Wang, L. Deng, and C. S. Cai, "Non-contact vehicle weighing method based on tire-road contact model and computer vision techniques," *Mechanical Systems and Signal Processing*, vol. 174, p. 109093, 2022.
[67] W. L. Lawton, "Static load contact pressure patterns under airplane tires," *Highw. Res. Board Proc*, vol. 36, pp. 233–239, 1957.
[68] N. W. Lister and D. E. Nunn, *Contact areas of commercial vehicle tyres*. Road Research Laboratory, 1968.
[69] J. D. Van Vuuren, "Relationship between tire inflation pressure and mean tire contact pressure," *Transportation research record*, vol. 523, pp. 76–87, 1974.
[70] E. J. Yoder and M. W. Witczak, *Principles of pavement design*. John Wiley & Sons, 1991.
[71] J. Ejsmont, S. Taryma, G. Ronowski, and B. Swieczko-Zurek, "Influence of temperature on the tyre rolling resistance," *International Journal of Automotive Technology*, vol. 19, pp. 45–54, 2018.
[72] Federal Highway Administration, "Policy Information," 2022. Available: https://www.fhwa.dot.gov/ohim/ohimvtis.cfm. [Accessed: Jun. 05, 2024]
[73] Y. H. Huang, *Pavement analysis and design*, vol. 2. Pearson Prentice Hall Upper Saddle River, NJ, 2004.
[74] S. W. Haider, R. S. Harichandran, and M. B. Dwaikat, "Closed-Form Solutions for Bimodal Axle Load Spectra and Relative Pavement Damage Estimation," *J. Transp. Eng.*, vol. 135, no. 12, pp. 974–983, Dec. 2009, doi: 10.1061/(ASCE)TE.1943-5436.0000077
[75] S. W. Haider and R. S. Harichandran, "Effect of Axle Load Spectrum Characteristics on Flexible Pavement Performance," *Transportation Research Record*, vol. 2095, no. 1, pp. 101–114, Jan. 2009, doi: 10.3141/2095-11
[76] MATLAB, "version 7.10.0 (R2010a). Natick, Massachusetts: The MathWorks Inc.," R2010.
[77] H. Wang and Z. Wang, "Deterministic and probabilistic life-cycle cost analysis of pavement overlays with different pre-overlay conditions," *Road Materials and Pavement Design*, vol. 20, no. 1, pp. 58–73, 2019.
[78] H. Wang, Z. Wang, J. Zhao, and J. Qian, "Life-cycle cost analysis of pay adjustment for initial smoothness of asphalt pavement overlay," *Journal of Testing and Evaluation*, vol. 48, no. 2, pp. 1350–1364, 2020.

[79] H. L. Von Quintus, A. L. Simpson, and A. A. Eltahan, “Rehabilitation of asphalt concrete pavements: Initial evaluation of the SPS-5 experiment-final report,” United States. Federal Highway Administration. Office of Engineering …, 2006.
[80] G. E. Elkins and B. Ostrom, “Long-term pavement performance information management system user guide,” United States. Federal Highway Administration. Office of Infrastructure …, 2021. Available: https://rosap.ntl.bts.gov/view/dot/55790. [Accessed: Jun. 05, 2024]
[81] ASTM, “Standard Practice for Roads and Parking Lots Pavement Condition Index Surveys,” 2018. Available: https://compass.astm.org/document/?contentCode=ASTM%7CD6433-23%7Cen-US&proxycl=https%3A%2F%2Fsecure.astm.org&fromLogin=true. [Accessed: Jun. 05, 2024]
[82] K. D. Smith and P. Ram, “Measuring and Specifying Pavement Smoothness:[techbrief],” United States. Federal Highway Administration, 2016.
[83] F. H. Administration (FHWA), “Guide to LTPP traffic data collection and processing.” Federal Highway Administration, Office of Infrastructure Research …, 2001.
[84] J. Devore, *Probability and statistics for engineering and the sciences (4th ed.)*. 1995.
[85] S. W. Haider and R. S. Harichandran, “Relating Axle Load Spectra to Truck Gross Vehicle Weights and Volumes,” *J. Transp. Eng.*, vol. 133, no. 12, pp. 696–705, Dec. 2007, doi: 10.1061/(ASCE)0733-947X(2007)133:12(696)
[86] D. H. Timm, S. M. Tisdale, and R. E. Turochy, “Axle load spectra characterization by mixed distribution modeling,” *Journal of Transportation Engineering*, vol. 131, no. 2, pp. 83–88, 2005.
[87] T. Thornton, J. Calvert, and M. Vrtis, “Forensic Investigation of HMA Test Sections for Laboratory and Field Comparisons,” 2021.
[88] M. Marasteanu, M. Turos, D. Ghosh, J. L. Matias de Oliveira, and T. Yan, “Investigation of cracking resistance of asphalt mixtures and binders,” 2019.
[89] Z. Zhang, “An integrated system for road condition and weigh-in-motion measurements using in-pavement strain sensors,” North Dakota State University, 2016.
[90] Z. Zhou *et al.*, “Optical fiber Bragg grating sensor assembly for 3D strain monitoring and its case study in highway pavement,” *Mechanical Systems and Signal Processing*, vol. 28, pp. 36–49, 2012.
[91] T. Hastie, R. Tibshirani, J. H. Friedman, and J. H. Friedman, *The elements of statistical learning: data mining, inference, and prediction*, vol. 2. Springer, 2009.
[92] V. Vapnik, *The nature of statistical learning theory*. Springer science & business media, 2013. Available: https://books.google.com/books?hl=en&lr=&id=EqgACAAAQBAJ&oi=fnd&pg=PR7&dq=The+nature+of+statistical+learning+theory&ots=g5E5nu8-39&sig=qDNZhCNhUDyck9ROHakpUYIGV6Y. [Accessed: Jun. 19, 2024]
[93] R. Kohavi, “A study of cross-validation and bootstrap for accuracy estimation and model selection,” in *Ijcai*, Montreal, Canada, 1995, pp. 1137–1145.
[94] T. Hastie, R. Tibshirani, and J. Friedman, “Random Forests,” in *The Elements of Statistical Learning*, in Springer Series in Statistics. New York, NY: Springer New York, 2009, pp. 587–604. doi: 10.1007/978-0-387-84858-7_15. Available: http://link.springer.com/10.1007/978-0-387-84858-7_15. [Accessed: Jun. 05, 2024]
[95] B. Üstün, W. J. Melssen, and L. M. C. Buydens, “Facilitating the application of Support Vector Regression by using a universal Pearson VII function based kernel,” *Chemometrics and Intelligent Laboratory Systems*, vol. 81, no. 1, pp. 29–40, Mar. 2006, doi: 10.1016/j.chemolab.2005.09.003
[96] Federal Highway Administration, “Compilation of Existing State Truck Size and Weight Limit Laws - Appendix A: State Truck Size and Weight Laws - FHWA Freight Management and Operations,” 2015. Available: https://ops.fhwa.dot.gov/freight/policy/rpt_congress/truck_sw_laws/app_a.htm#nj. [Accessed: Jun. 19, 2024]
[97] J. J. Hajek, W. A. Phang, A. Prakash, and G. A. Wrong, “Performance prediction for pavement management,” in *North American Pavement Management Conference, March 18 to 21 1985*,

Citeseer, 1985. Available: https://citeseerx.ist.psu.edu/document?repid=rep1&type=pdf&doi=8632213855756c212874c1cb6d0b1e60dd632d57. [Accessed: Jun. 05, 2024]
[98] N. C. Jackson, R. Deighton, and D. L. Huft, "Development of pavement performance curves for individual distress indexes in South Dakota based on expert opinion," *Transportation Research Record*, vol. 1524, no. 1, pp. 130–136, 1996.
[99] L. Breiman, "Random forests," *Machine Learning*, vol. 45, no. 1, pp. 5–32, 2001, doi: 10.1023/A:1010933404324
[100] H. Ishwaran and U. B. Kogalur, "Random survival forests for R," *R news*, vol. 7, no. 2, pp. 25–31, 2007.
[101] T. Gneiting and A. E. Raftery, "Strictly Proper Scoring Rules, Prediction, and Estimation," *Journal of the American Statistical Association*, vol. 102, no. 477, pp. 359–378, Mar. 2007, doi: 10.1198/016214506000001437
[102] F. E. Harrell, K. L. Lee, and D. B. Mark, "MULTIVARIABLE PROGNOSTIC MODELS: ISSUES IN DEVELOPING MODELS, EVALUATING ASSUMPTIONS AND ADEQUACY, AND MEASURING AND REDUCING ERRORS," *Statist. Med.*, vol. 15, no. 4, pp. 361–387, Feb. 1996, doi: 10.1002/(SICI)1097-0258(19960229)15:4<361::AID-SIM168>3.0.CO;2-4
[103] U. B. Mogensen, H. Ishwaran, and T. A. Gerds, "Evaluating random forests for survival analysis using prediction error curves," *Journal of statistical software*, vol. 50, no. 11, p. 1, 2012.
[104] B. Goenaga, L. Fuentes, and O. Mora, "A Practical Approach to Incorporate Roughness-Induced Dynamic Loads in Pavement Design and Performance Prediction," *Arab J Sci Eng*, vol. 44, no. 5, pp. 4339–4348, May 2019, doi: 10.1007/s13369-018-3414-9
[105] L. Sun, "Developing spectrum-based models for international roughness index and present serviceability index," *Journal of transportation engineering*, vol. 127, no. 6, pp. 463–470, 2001.
[106] L. Sun, "Simulation of pavement roughness and IRI based on power spectral density," *Mathematics and computers in simulation*, vol. 61, no. 2, pp. 77–88, 2003.
[107] A. Ueckermann and M. Oeser, "Approaches for a 3D assessment of pavement evenness data based on 3D vehicle models," *journal of traffic and transportation engineering (english edition)*, vol. 2, no. 2, pp. 68–80, 2015.
[108] M. W. Sayers, "Road characterization for the simulation of automotive vehicle dynamics," *SAE International Journal of Materials and Manufacturing*, vol. 4, no. 1, pp. 251–262, 2011.
[109] A. M. Marques Almeida and L. G. D. P. Santos, "Methodological Framework for Truck-Factor Estimation Considering Vehicle–Pavement Interaction," *J. Transp. Eng.*, vol. 141, no. 2, p. 04014074, Feb. 2015, doi: 10.1061/(ASCE)TE.1943-5436.0000726
[110] W. J. Steyn, N. Viljoen, L. Popescu, and L. Du Plessis, "Freight-Truck-Pavement Interaction, Logistics, and Economics: Final Phase 1 Report (Tasks 1–6)," 2012.
[111] E. H. Law, I. Janajreh, and N. Frey, "Vehicle ride response to new widebase tires and conventional dual tires," SAE Technical Paper, 2002.
[112] H. Wang, Z. Wang, R. J. Blight, and E. C. Sheehy, "Derivation of pay adjustment for in-place air void of asphalt pavement from life-cycle cost analysis," *Road Materials and Pavement Design*, vol. 16, no. 3, pp. 505–517, 2015.
[113] T. D. Gillespie, *Effects of heavy-vehicle characteristics on pavement response and performance*, vol. 353. Transportation Research Board, 1993. Available: https://books.google.com/books?hl=en&lr=&id=yncb0ohhmygC&oi=fnd&pg=PA7&dq=Effects+of+Heavy+Vehicle+Characteristics+on+Pavement+Response+and+Performance&ots=V4KAVXIyXW&sig=-HmELbzgXIp9YdlCVHD710hVnLw. [Accessed: Jun. 05, 2024]
[114] D. Rys, "Consideration of dynamic loads in the determination of axle load spectra for pavement design," *Road Materials and Pavement Design*, vol. 22, no. 6, pp. 1309–1328, 2021.
[115] F. Zhou, S. Hu, X. Hu, and T. Scullion, "Mechanistic-empirical asphalt overlay thickness design and analysis system.," Texas Transportation Institute, 2009.

[116] Aa. AASHTO, "Mechanistic-empirical pavement design guide: A manual of practice," *AAoSHaT Officials, Editor*, 2008.
[117] T. Thornton, J. Calvert, and M. Vrtis, "Forensic Investigation of HMA Test Sections for Laboratory and Field Comparisons," 2021.
[118] A.-C. Haury, P. Gestraud, and J.-P. Vert, "The influence of feature selection methods on accuracy, stability and interpretability of molecular signatures," *PloS one*, vol. 6, no. 12, p. e28210, 2011.
[119] H. Alizadeh Noughabi, "Two powerful tests for normality," *Annals of Data Science*, vol. 3, no. 2, pp. 225–234, 2016.
[120] P. Mishra, C. M. Pandey, U. Singh, A. Gupta, C. Sahu, and A. Keshri, "Descriptive statistics and normality tests for statistical data," *Annals of cardiac anaesthesia*, vol. 22, no. 1, p. 67, 2019.
[121] S. S. Shapiro and M. B. Wilk, "An analysis of variance test for normality (complete samples)," *Biometrika*, vol. 52, no. 3/4, pp. 591–611, 1965.
[122] N. M. Razali and Y. B. Wah, "Power comparisons of shapiro-wilk, kolmogorov-smirnov, lilliefors and anderson-darling tests," *Journal of statistical modeling and analytics*, vol. 2, no. 1, pp. 21–33, 2011.
[123] S.-B. Cho and H.-H. Won, "Machine learning in DNA microarray analysis for cancer classification," presented at the Proceedings of the First Asia-Pacific Bioinformatics Conference on Bioinformatics 2003-Volume 19, 2003, pp. 189–198.
[124] C. Xiao, J. Ye, R. M. Esteves, and C. Rong, "Using Spearman's correlation coefficients for exploratory data analysis on big dataset," *Concurrency and Computation: Practice and Experience*, vol. 28, no. 14, pp. 3866–3878, 2016.
[125] H. Akoglu, "User's guide to correlation coefficients," *Turkish journal of emergency medicine*, vol. 18, no. 3, pp. 91–93, 2018.
[126] E. Ostertagová, "Modelling using polynomial regression," *Procedia Engineering*, vol. 48, pp. 500–506, 2012.
[127] A. Pant, "Introduction to linear regression and polynomial regression," *URL https://towardsdatascience. com/introduction-to-linear-regressionand-polynomial-regression-f8adc96f31cb*, 2019.
[128] S. Kim, S. Kim, C. H. Green, and J. Jeong, "Multivariate polynomial regression modeling of total dissolved-solids in rangeland stormwater runoff in the Colorado River Basin," *Environmental Modelling & Software*, vol. 157, p. 105523, 2022.
[129] S. Qiu, L. M. Dooley, and L. Xie, "How servant leadership and self-efficacy interact to affect service quality in the hospitality industry: A polynomial regression with response surface analysis," *Tourism Management*, vol. 78, p. 104051, 2020.
[130] C. Y. Tang, K. Fung, E. W. Lee, G. T. Ho, K. W. Siu, and W. Mou, "Product form design using customer perception evaluation by a combined superellipse fitting and ANN approach," *Advanced Engineering Informatics*, vol. 27, no. 3, pp. 386–394, 2013.
[131] A. Shan, I. Hafeez, S. Hussan, and M. B. Jamil, "Predicting the laboratory rutting response of asphalt mixtures using different neural network algorithms," *International Journal of Pavement Engineering*, vol. 23, no. 6, pp. 1948–1956, May 2022, doi: 10.1080/10298436.2020.1830282
[132] F. Rosenblatt, "Principles of neurodynamics. perceptrons and the theory of brain mechanisms," Cornell Aeronautical Lab Inc Buffalo NY, 1961.
[133] M. W. Gardner and S. Dorling, "Artificial neural networks (the multilayer perceptron)—a review of applications in the atmospheric sciences," *Atmospheric environment*, vol. 32, no. 14–15, pp. 2627–2636, 1998.
[134] Y.-D. Zhang *et al.*, "Voxelwise detection of cerebral microbleed in CADASIL patients by leaky rectified linear unit and early stopping," *Multimedia Tools and Applications*, vol. 77, pp. 21825–21845, 2018.

[135] K. Hara, D. Saito, and H. Shouno, "Analysis of function of rectified linear unit used in deep learning," presented at the 2015 international joint conference on neural networks (IJCNN), IEEE, 2015, pp. 1–8.
[136] S.-H. Wang, P. Phillips, Y. Sui, B. Liu, M. Yang, and H. Cheng, "Classification of Alzheimer's disease based on eight-layer convolutional neural network with leaky rectified linear unit and max pooling," *Journal of medical systems*, vol. 42, pp. 1–11, 2018.
[137] D. Chicco, M. J. Warrens, and G. Jurman, "The coefficient of determination R-squared is more informative than SMAPE, MAE, MAPE, MSE and RMSE in regression analysis evaluation," *PeerJ Computer Science*, vol. 7, p. e623, 2021.
[138] H. Michael, J. Christopher, N. John, and L. William, "Applied linear statistical models," *5th ed. Boston: McGraw-Hil*, 2005.
[139] Federal Highway Administration, "WEIGH-IN-MOTION POCKET GUIDE," 2019.
[140] Y. Hai-qing, Y. Jun, and D. Jing, "The sensing principle of FBG and its experimental application in structure strengthening detection," *Journal of Wuhan University of Technology-Mater. Sci. Ed.*, vol. 18, pp. 94–96, 2003.
[141] L. Fan, K. Le, C. Guo, C. Sun, and G. Chen, "Magnet-assisted hybrid EFPI/FBG sensor for internal corrosion monitoring of steel pipelines," *Optical Fiber Technology*, vol. 73, p. 103064, 2022.
[142] M. Liao, S. Liang, R. Luo, and Y. Xiao, "The cooperative deformation test of an embedded FBG sensor and strain correction curve verification," *Construction and Building Materials*, vol. 342, p. 128029, 2022.
[143] Z. Zhou, J. Li, and J. Ou, "Interface transferring mechanism and error modification of embedded FBG strain sensors," *Frontiers of Electrical and Electronic Engineering in China*, vol. 2, pp. 92–98, 2007.
[144] R. Michalczyk, "Implementation of generalized viscoelastic material model in Abaqus code," *Logistyka*, no. 6, 2011.
[145] Y. H. Huang, *Pavement analysis and design*, vol. 2. Pearson Prentice Hall Upper Saddle River, NJ, 2004.
[146] W. Alkasawneh, E. Pan, and R. Green, "The effect of loading configuration and footprint geometry on flexible pavement response based on linear elastic theory," *Road materials and pavement design*, vol. 9, no. 2, pp. 159–179, 2008.
[147] H.-L. Kou, W. Li, W.-C. Zhang, Y. Zhou, and X.-L. Zhou, "Stress monitoring on GFRP anchors based on fiber Bragg grating sensors," *Sensors*, vol. 19, no. 7, p. 1507, 2019.
[148] R. Bonaquist and D. W. Christensen, "Practical procedure for developing dynamic modulus master curves for pavement structural design," *Transportation Research Record*, vol. 1929, no. 1, pp. 208–217, 2005.
[149] C. Olidis and D. Hein, "Guide for the mechanistic-empirical design of new and rehabilitated pavement structures materials characterization: Is your agency ready," in *2004 annual conference of the transportation association of Canada*, 2004.
[150] M. R. Islam, S. A. Kalevela, and G. Mendel, "How the mix factors affect the dynamic modulus of hot-mix asphalt," *Journal of Composites Science*, vol. 3, no. 3, p. 72, 2019.
[151] T. Bennert, "Dynamic modulus of hot mix asphalt: final report, June 2009.," New Jersey. Dept. of Transportation, 2009.
[152] X. Kong *et al.*, "Tire contact force equations for vision-based vehicle weight identification," *Applied Sciences*, vol. 12, no. 9, p. 4487, 2022.
[153] "U.S. vehicle fleet 1990-2022," *Statista*. Available: https://www.statista.com/statistics/183505/number-of-vehicles-in-the-united-states-since-1990/. [Accessed: Jan. 12, 2024]
[154] A. Lansdell, W. Song, and B. Dixon, "Development and testing of a bridge weigh-in-motion method considering nonconstant vehicle speed," *Engineering Structures*, vol. 152, pp. 709–726, 2017.

[155] R. Bajwa, R. Rajagopal, E. Coleri, P. Varaiya, and C. Flores, “In-pavement wireless weigh-in-motion,” in *Proceedings of the 12th international conference on Information processing in sensor networks*, 2013, pp. 103–114.
[156] X. Liu and I. L. Al-Qadi, “Development of a simulated three-dimensional truck model to predict excess fuel consumption resulting from pavement roughness,” *Transportation Research Record*, vol. 2675, no. 9, pp. 1444–1456, 2021.
[157] X. Yang, X. Wang, J. Podolsky, Y. Huang, and P. Lu, “Development of asphalt pavement temperature prediction models utilising multiple regression and artificial neural network approaches: a field study in North America,” *International Journal of Pavement Engineering*, vol. 24, no. 2, p. 2279250, 2023.
[158] X. Yang, X. Wang, J. Podolsky, Y. Huang, and P. Lu, “Assessing Vehicle Wandering Effects on the Accuracy of Weigh-in-Motion Measurement Based on In-Pavement Fiber Bragg Sensors through a Hybrid Sensor-Camera System,” *Sensors*, vol. 23, no. 21, p. 8707, 2023.
[159] H. Wang, P. Xiang, and L. Jiang, “Optical fiber sensor based in-field structural performance monitoring of multilayered asphalt pavement,” *Journal of Lightwave Technology*, vol. 36, no. 17, pp. 3624–3632, 2018.
[160] Y. Huang, L. Palek, R. Strommen, B. Worel, and G. Chen, “Real-time weigh-in-motion measurement using fiber Bragg grating sensors,” in *Sensors and Smart Structures Technologies for Civil, Mechanical, and Aerospace Systems 2014*, SPIE, 2014, pp. 47–55.
[161] Y. Liu, J. Xie, S. Liu, Y. Zhao, Y. Zhu, and G. Qi, “Research on the methodology of development and calibration of flexible encapsulated fiber Bragg grating sensors,” *Measurement*, vol. 201, p. 111730, 2022.
[162] M. Majumder, T. K. Gangopadhyay, A. K. Chakraborty, K. Dasgupta, and D. K. Bhattacharya, “Fibre Bragg gratings in structural health monitoring—Present status and applications,” *Sensors and Actuators A: Physical*, vol. 147, no. 1, pp. 150–164, 2008.
[163] Y.-Q. Liu, X. Du, H.-L. Shen, and S.-J. Chen, “Estimating generalized gaussian blur kernels for out-of-focus image deblurring,” *IEEE Transactions on circuits and systems for video technology*, vol. 31, no. 3, pp. 829–843, 2020.
[164] T. Popkin, A. Cavallaro, and D. Hands, “Accurate and efficient method for smoothly space-variant Gaussian blurring,” *IEEE Transactions on image processing*, vol. 19, no. 5, pp. 1362–1370, 2010.
[165] A. Ajmal, C. Hollitt, M. Frean, and H. Al-Sahaf, “A comparison of RGB and HSV colour spaces for visual attention models,” presented at the 2018 International conference on image and vision computing New Zealand (IVCNZ), IEEE, 2018, pp. 1–6.
[166] V. Chernov, J. Alander, and V. Bochko, “Integer-based accurate conversion between RGB and HSV color spaces,” *Computers & Electrical Engineering*, vol. 46, pp. 328–337, 2015.
[167] J. Braunfelds *et al.*, “Development of the Strain Measurement Calibration Technique for Road Pavement Structural Health Monitoring Applications Using Optical FBG Sensors,” in *2023 Photonics & Electromagnetics Research Symposium (PIERS)*, IEEE, 2023, pp. 1060–1065. Available: https://ieeexplore.ieee.org/abstract/document/10221310/. [Accessed: Apr. 04, 2024]